Università
degli Studi di
Pavia

Dipartimento di
Fisica
"A. Volta"

DOTTORATO DI RICERCA IN FISICA – XXIII CICLO

Time-resolved optical spectroscopy on $Bi_2Sr_2Ca_{0.92}Y_{0.08}Cu_2O_{8+\delta}$

dissertation submitted by

Stefano Dal Conte

to obtain the degree of

DOTTORE DI RICERCA IN FISICA

Supervisors: Dott. P. Galinetto

Department of Physics "A. Volta", University of Pavia

Prof. F. Parmigiani

Department of Physics, University of Trieste

Dott. C. Giannetti

Department of Physics, University of Brescia

Referee: Prof. A. Damascelli

Department of Physics and Astronomy, University of British Columbia

Cover: Supercontinuum pulse spectrogram measured through two-photon absorption in a ZnSe crystal.

Time-resolved optical spectroscopy on $Bi_2Sr_2Ca_{0.92}Y_{0.08}Cu_2O_{8+\delta}$
Stefano Dal Conte
PhD thesis – University of Pavia
Printed in Pavia, Italy, December 2010
ISBN 978-88-95767-39-0

to Annamaria, Carlo, Matteo
and
Martina

Contents

Chapter 1

Introduction

1.1 Overview

Superconductivity represents one of the most amazing discovery of the last century. It was discovered by Kamerlingh Onnes and his collaborators in 1911 when, immerging a thin mercury wire into liquid helium, it was observed that under 4.2 K, the sample undergoes a transition to a phase in which the resistivity surprisingly drops to zero. This new state of the matter was called superconductive state.
This discovery opened the way, in the following years, to a large amount of experimental works that led to identify many other superconductive materials, like tin and lead. Despite the growing interest surrounding the discovery of Onnes, it took almost fifty years to reach a full theoretical explanation of the superconductivity.
In 1957 Bardeen Cooper and Schrieffer developed a microscopic theory of the superconductivity which was called later BCS theory in their honour. A significative step towards the formulation of this theory is due to Cooper which demonstrate that the normal Fermi sea becomes instable if a whatever small attractive interaction is effective among the electrons [26]. In BCS superconductors this attractive force is mediated by the phonons and bring the electrons, lying near the Fermi surface, to form the so-called Cooper pairs. Each pair is formed by two electrons with opposite momentum and spin. In simple terms the picture is the following: one electron interacts with ions and polarizes the lattice while another electron, coming afterwords, interacts with the polarized lattice. This variation of the lattice polarization is felt by the second electron as an effective attractive interaction that, below the critical temperature T_c, overcomes the Coulomb repulsive force and allow the electrons to couple in pairs. In other words, the glue which binds the electrons together, is given by the phonons. The so-formed pairs strongly overlap due to the long-range coherence and form a condensate in order to minimize the total energy of the system. All the Cooper pairs are described by the same wavefunction, characterized by a phase, which remains coherent over a macroscopic length scale (i.e. of the order of 10^{-6} m). The collective behaviour of the condensate is responsible of many macroscopic effects observed in these systems, like the opening of an isotropic (s-wave) superconductive gap in the continuum spectrum of the allowed energy states [118].
The BCS theory was believed to give an exhaustive explanation of superconduc-

tivity until 1986, when J. G. Bednorz and K. A. Müller discovered the superconductive properties of La-based cuprate compound with a critical temperature above 30 K [14]. For this discovery they were awarded the 1987 Nobel prize of Physics. Soon after, compounds with T_c as high as the temperature of liquid nitrogen were discovered and a superconductive transition temperature of 90 K was found in the compound YBaCuO by Wu [134]. Just to give an idea of the importance of this discovery, the record of the highest critical temperature before 1986 was 23.3 K in the alloy Nb_3Ge.
The cuprates superconductors are compounds which are characterized by a crystal structures with one or more sheets of CuO_2, separated by insulating block layers. Since the advent of first cuprate and the present days more than 200 superconductors were synthetized with different chemical compositions and crystal structures. The maximum T_c found until now is in the mercury-based compounds which has a T_c=133 K at ambient pressure (about 160 K under pressure).
The discovery of high-T_c superconductivity (HTCS) induced an unprecedented worlwide effort to discover the physical mechanism at the base of many physical properties that the BCS model is not able to capture.
In these years, a huge amount of experimental and theoretical works have been proposed in order to find the mechanism that causes the pairing of electronic carriers but a definitive answer to this question does not exist. The scientific community is divided on this issue. Part of that is convinced that electron-phonon coupling is still the responsible of the pairing mechanism like in conventional superconductors while an other part is persuaded of the electronic origin of the superconductivity's glue [1, 7, 68, 88, 109]. A possible hypothesis which has spread out recently, is that the high-temperature superconductivity in cuprates is the result of the interplay between the electron-phonon interaction and an interaction mediated by other bosons of electronic origin, like spin fluctuations [60, 61]. Moreover the electron-boson coupling function $\alpha^2F(\Omega)$ of HTCS, extracted from optical and inelastic neutron scattering measurements, is characterized by a broad continuum spectrum extending beyond the Debye frequency, in contrast to BCS superconductors where $\alpha^2F(\Omega)$ is limited to the energy range of the characteristic frequencies of the lattice modes [58, 127]. The specific nature and the identification of the role played by these high-energy bosons constitutes an outstanding issue.
Another interesting but not solved problem, together with the determination of the superconductive glue, is given by the possible interdependence between the high and low energy electronic properties in the cuprates below T_c. In BCS superconductors the occurence of the superconductivity is accompanied by the opening of the gap 2Δ which affects only the electronic states in an energy shell of the same order of $\pm\Delta$ (where Δ is of the order of few meV) near the Fermi level. On the contrary, in the HTSC, the formation of the superconductive condensate seems to modify also the physical properties in the visible region. Recent equilibrium optical measurements evidenced a superconductivity induced spectral weight shift from the intraband to interband optical region [20, 90, 107]. This result seems to be in agreement with the hole-superconductivity model proposed by Hirsch *et al.* [53, 51], according to which, in cuprates, the superconductivity is driven by a kinetic energy gain in contrast with the BCS-like increasing of the kinetic energy. However the difficulty to choose the cutoff frequency separating the two energy regions and the broadening of the Drude

peak have prevented finally to clarify whether the spectral weigth transfer over a broad frequency range is due to a thermal effect or it is a real modification of the electronic properties in visible range [96].
The intriguing puzzle of HTSC is further complicated by another problem, i.e. the appearence below a certain temperature $T^*>T_c$ of a new phase which is called pseudogap phase. This phase has peculiar properties which differs from that found in both the superconductive and normal state. Recently, scientists have focused on trying to understand the origin of the pseudogap state and in particular the possible relation with the superconductive state [55, 117]. Two main scenarios have been proposed [95]. In the first one, the pseudogap is described as a state dominated by an hidden order which is in competition with the superconductive state [23, 129]. In the second scenario the electrons are supposed to form Cooper pairs below T^* while the formation of the condensate due to the long range phase coherence, occurs below T_c. In this sense the pseudogap phase represents a precursor of the superconductive phase [42].
In order to validate one of these two different interpretations, it's necessary to get more insight to the nature of the pseudogap. In particular it has to be clarified whether the occurrence of this phase is accompanied by an opening of the gap in the quasiparticles density of states or it is an effect caused by the suppression of the spectral weight in the single-particle spectral function [55]. Since the discovery of HTSC, a wide variety of experimental techniques, i.e. equilibrium optical spectroscopy, angle-resolved photoemission spectroscopy, tunnelling spectroscopy and inelastic neutron scattering have been employed to study the physical properties of this systems. All these experimental techniques probe the equilibrium state of the materials.
Ultrafast time-resolved spectroscopy has been used more and more frequently in the last 20 years due to the rapid development of ultrafast laser sources. This technique investigates the out-of-equilibrium physical properties and has been applied to HTSC and other strongly correlated system like charge and spin density wave systems and heavy fermion systems [35, 47, 50, 110, 34].
In a time-resolved experiment a femtosecond laser pulse prepares the system in a non-equilibrium state and a second delayed pulse probes the recovery of the equilibrium state.
In the case of HTSC, the success of this experimental technique relies on the possibility to study in the time-domain the interaction between the electronic carriers and the phonons directly determining the strength of the coupling λ without the need to perform a complicate integration of the electron-boson coupling function. Moreover, in contrast with all the time-integrated spectroscopies which are blind to the nature of the bosonic glue, a time-resolved technique have the capability to disentangle the different bosonic excitations described by $\alpha^2F(\Omega)$ because of a different specific heat and, consequentely, a different relaxation time.
Another important characteristic of this experimental technique is given by the strong sensitivity of the temporal response to the electronic phase of the system which could allow to study the possible interplay between the pseudogap and the superconductive phase.
A long standing problem concerns the origin of the transient reflectivity variation measured in the superconductive state. Below T_c the transient signal exhibits a

strong doping dependence variation and an increase of one order of magnitude with respect the case of a noble metals. A possible explanation has been ascribed to a modification of the optical properties of the system due to a superconductivity induced rearrangement of the electronic bands, instead of a simple thermal effect. Up to now, all the time-resolved reflectivity experiments in the visible region on the HTSC have been performed at the probe energy of 1.5 eV and the study of the temporal behaviour of the system is limited to the output frequency of the Ti:sapphire lasers. The lack of spectral resolution of the probe pulse prevented to relate the measured reflectivity variation to a pump-induced modification of the dielectric function of the system avoiding to explain the origin of the signal measured in the superconducting phase.

1.2 Outline

In this thesis work we study for the first time the non-equilibrium optical response of a high-temperature superconductor, more precisely, of a $Bi_2Sr_2Ca_{0.92}Y_{0.08}Cu_2O_{8+\delta}$ crystal, at different doping levels and temperatures, over a wide spectral range which covers all the visible and part of the infrared region. The optical spectroscopy technique we use, is characterized by both spectral and temporal resolution and exploits the large spectral content of the supercontinuum light produced by a non-linear photonic crystal fiber. The probe frequency window is further extended towards the infrared region by an optical parametric amplifier system. The use of this non-equilibrium approach allows to face various open problems related to the HTSC and sometimes presents some advantages with respect to the standard equilibrium spectroscopies. To be more precise the main issues that we want to tackle in this work are the following:

1. What is the glue responsible for binding the electrons into superconducting pairs? Is the pairing mediated by phonons or by other bosonic modes of electronic origin or by both these elements?

2. Are the pseudogap and superconductivity competitive effects or can they coexist? Is the pseudogap a real gap in the density of states?

3. What is the origin of the superconductivity-induced spectral weight transfer from the interband to intraband optical region? Is it a real modification of the electronic properties in the visible range or is it a simple thermal effects due to the broadening of the Drude peak?. Which are the optical transitions involved? Does this modification involve a superconductive-induced rearrangement of Cu-O bonds, partecipating to the condensate formation?

The work has been organized in these chapters:

- In the second chapter a general description of the electronic properties of the HTSC is given together with a brief description of different models describing the coupling mechanisms. The chapter outlines the physical properties of the pseudogap phase and it describes the non-Fermi liquid behavior of the normal state of HTSC.

- In the third chapter we introduce the Extended Drude model, commonly used to describe the equilibrium optical properties of the HTSC. The problem of the possible sum rule violation related to the spectral weight shift, is presented. The second part of this chapter presents the non-equilibrium optical properties of the HTSC and introduces the theoretical models that describe the temporal dependence of the electron and phonon temperatures in a high-temperature superconductors excited by an ultrashort laser pulse.

- The description of the experimental set up is sketched in the four chapter. In particular great importance is given to the detection and characterization of the supercontinuum light pulse and to the physical mechanism responsible for its production.

- The equilibrium optical measurements are shown in chapter five. The Extended Drude model is used to fit the data. Finally, the electron-boson coupling function is extracted from the optical spectra using a strong-coupling analysis.

- In chapter six we show one-color pump-probe reflectivity measurements. The electronic temperature dependence and the electron-phonon coupling constant is extracted from the dynamics.

- Time and frequency resolved reflectivity measurements in normal state are reported in chapter seven. Starting from the strong coupling formalism used to describe the equilibrium dielectric function, we develop a differential model to fit the pump-induced modification of the reflectivity over the whole probe energy range at different delay times. This approach allows us to disentangle the contribution of the electronic and the bosonic temperature due to the different temporal scale and to gain important information about the coupling mechanism in HTSC demonstrating that both phonons and other bosonic excitation of electronic origin contribute to the high T_c of these systems.

- In chapter eight, pump-supercontinuum probe reflectivity measurements in pseudogap phase are shown. The results of the fit of the differential model to the data can be explained in term of a transient increasing of the Drude plasma frequency and a weakening of the low-energy bosonic mode. In particular the positive variation of the plasma frequency has an opposite trend with respect the normal state behaviour and seems to support the hypothesis that a gap in the density of state starts to open in the pseudogap phase.

- The superconductivity induced variation of reflectivity ($T<T_c$), reported in chapter nine, can be accounted for by assuming a transient modification of the optical properties in the visible region. In particular a significative modification of the optical oscillators centered at 1.5 eV and 2 eV is observed. This result puts an end to the long-lived and hotly dabated issue about the increase of the transient signal observed in HTSC below T_c. Thanks to the wide spectral content of the probe pulse, we can assert that the measured signal is not given by a simple excited state absorption but it is caused by a modification of the electronic bands.

Chapter 2

High temperature superconductivity: models and open questions

2.1 Introduction

In this chapter we describe the physical properties of an HTSC from a theoretical point of view. At the begining we give a short introduction of the theoretical models proposed to describe the low-energy electronic states of cuprates. Then a sketch of the different versions of the phase diagram that have been proposed in the last years, is given. In particular we focus on the pseudogap phase which represents one of the most intriguing aspect of the HTSC. The two following sections are devoted to the description of the various mechanisms proposed to explain the formation of Cooper pairs in HTSC. Particular importance is given to the model of the hole superconductivity proposed by J.E. Hirsch and F. Marsiglio [52]. Finally we discuss different aspects related to the non-Fermi liquid behaviour of the cuprates.

2.2 Electronic properties of HTSC

High-temperature superconductivity (HTSC) represents one of the most interesting and intriguing problem of the modern condensed matter physics [14]. Despite a lot of efforts of the scientific community to develop new experimental and theoretical tools to get more insight to this problem, HTSC still remains an open issue and its origin is object of a strong debate. The superconductivity with the higher critical temperature was found in compounds belonging to the family of copper oxides (cuprates). The feature common to all cuprates is given by two dimensional CuO_2 planes weakly interacting with the neighboring planes containing other atoms, like Ba, La, Bi, acting like charge reservoir to dope with hole or electron the CuO plane [22, 119]. Hole doping can also be achieved, like in the case of $Bi_2Sr_2CaCu_2O_{8+\delta}$ (Bi2212), by addiction of oxygen ions to the charge reservoir layers. The copper oxygen planes play a fundamental role because the Cu-O orbitals within these planes form the

electronic bands close to the Fermi level. Below a critical temperature T_c electrons in these planes overcome the Coulomb repulsion, forming a condensate of Cooper pairs characterized by a macroscopic coherence length. Before describing the different mechanisms proposed to explain the phenomenom of HTSC, we summarize the peculiar electronic properties of the undoped parent compound. Considering the undoped compound of $La_{2-x}Sr_xCuO_4$, i.e. La_2CuO_4, the valence of Cu is 2^+, leading to a $3d^9$ electronic configuration of copper atoms. The crystal field that derives from the interaction with the four planar oxygens surrounding the copper atom and the out of plane oxygens (apical oxygens) breaks the degeneracy of the d-levels leading to the splitting into four occupied low energy orbitals (with symmetry xy, xz, yz, $3z^2$-r^2) and one half-filled high energy orbital x^2-y^2 [59, 103]. According to the band theory this compound should be a metal but experimental findings indicate that it is an insulator with a large gap (2 eV) where the spins of the Cu holes are coupled antiferromagnetically [136]. The failure of the band theory comes from its inability to include the dramatic effects of the strong electronic correlations.
The Hubbard model is believed to capture the main part of the physics of the strongly correlated materials [6]. The single band Hubbard Hamiltonian can be divided into two terms:

$$H = -t \sum_{<ij>,\sigma} \left(c^+_{i,\sigma} c_{j\sigma} + H.c. \right) + U \sum_i n_{i,\downarrow} n_{i,\uparrow} \tag{2.1}$$

The first term describes the quantum hopping of electrons between nearest neighbor sites, while the second term is the Hubbard U term that accounts for the strong Coulomb interaction between electrons that occupy the same site. In the more specific case of the cuprates, the low energy electronic structure can be described by the so called three band Hubbard Hamiltonians that is given by [41, 131]:

$$H = \sum_{i\sigma} \epsilon_d d^+_{i\sigma} d_{i\sigma} + \sum_{i\sigma} \epsilon_p p^+_{i\sigma} p_{i\sigma} + \sum_{<ij>\sigma} t_{p,d} p^+_{j\sigma} d_{i\sigma} + H.c. + \\ + \sum_i U_d n_{i,\downarrow} n_{i,\uparrow} + \sum_{<jj'>\sigma} t_{O-O} p^+_{j\sigma} p_{j'\sigma} \tag{2.2}$$

Having adopted the hole picture, the operator $d^+_{i\sigma}$ creates a Cu hole at the site i with energy ϵ_d, $p^+_{j\sigma}$ creates an O $2p$ hole at the site j, the third term takes into account the hopping between oxygen and copper electronic orbitals, while the fourth and the fifth term describe the Coulomb repulsion term between two holes on the same Cu site and the hopping between nearest-neighbour oxygens. If the energy difference $\epsilon_p - \epsilon_d$ (charge transfer energy) is large enough compared with the hopping amplitude t_{pd}, the holes remain localized on the Cu site. In other words the hopping is responsible for antiferromagnetic superexchange near-neighbour spin correlations between Cu holes, where the exchange integral is given by:

$$J = \frac{t^4_{pd}}{(\epsilon_p - \epsilon_d)^3} \tag{2.3}$$

As the parent compound is doped, for example replacing in La_2CuO_4 a trivalent La atom with a divalent Sr atom, an extra number of holes is injected in the CuO_4 plaquettes. Due to the strong Coulomb repulsion term U_d, the holes occupy the oxygen p orbitals. This hole-doped system may gain energy because of the hole hopping between Cu and O orbital which leads to an antiferromagnetic superexchange

interaction of the Cu-O holes. In particular, a lower energy state is obtained by a fully symmetric linear combination of oxygen hole states around the Cu site with the Cu hole spin that couples antiferromagnetically to the O hole spins. This singlet state, known as Zhang-Rice singlet, can hop from site to site like a single hole does in a simple Hubbard model [137]. It is important to notice that it is possible to recover the single band Hubbard model only in the case of a single hole added to the undoped compound: when additional holes move in the 2D lattice, as in the case of doped cuprates, the single-band approximation is not still valid and the interactions between neighboring Zhang-Rice singlets has to be considered. The question whether the single band Hubbard model can satisfactorily describe the physics of HTSC is still an open problem, although spin-resolved photoemission measurements [**?**] and theoretical calculation using Dynamical Mean Field Theory (DMFT) recently confirmed that the lowest energy excitations have a singlet nature providing a direct support to the stability of the Zhang-Rice singlet in hole-doped cuprates. Despite its apparent simplicity the Hubbard model is very hard to solve: one of the most studied simplified Hamiltonians in the field of HTSC is called $t-J$ model and is obtained from the Hubbard model by projecting out the doubly occupied states at large U [30]:

$$H = -t \sum_{<ij>,\sigma} \left(c^{+}_{i,\sigma} c_{j\sigma} + \ H.c. \right) \ + \ J \sum_{<ij>} \left(\mathbf{S}_i \cdot \mathbf{S}_j - \frac{1}{4} n_i n_j \right) \tag{2.4}$$

The $t-J$ Hamiltonian is widely used as a starting point to describe the electronic properties of HTSC, however the possibility that the electronic excitations alone are not sufficient to explain the pairing of the electrons has been recently discussed. For this reason, many efforts have been devoted to study the electron-phonon interaction effects in the $t-J$ model [60, 61, 68, 88].

2.3 Phase diagram and pseudogap phase

The physical properties of HTSC crucially depend on the nature of the dopant carriers (electrons or holes) and on their concentration. In fig. 2.1 we sketch the phase diagram of an HTSC, showing the different phases as a function of the temperature and of the dopant concentration. We focus on the hole-doped side of the diagram. As the density of the holes in the CuO_2 planes is increased, the antiferromagnetic correlations break down and, below a critical temperature T_c, the system is driven to the superconductive state and a d-wave symmetry gap starts to open at the Fermi level [111, 121]. The T_c curve has a dome shape with a maximum that corresponds to an optimal doping condition which, in the case of $Bi_2Sr_2CaCu_2O_{8+\delta}$ (Bi2212), is 0.16 holes per Cu atom [79]. The superconductive state persists until about the 30% of hole doping. Above this concentration the electronic properties of the system change and it is strongly discussed if the Fermi liquid behaviour is recovered at high-doping concentration, in the overdoped region. Above T_c and in the underdoped region of the phase diagram the antiferromagnetic-insulating phase continuously evolves into another exotic phase not found in the standard BCS superconductors, known as pseudogap phase. This phase was observed for the first time by measuring the decrease of the spin-lattice relaxation in an NMR experiment

on underdoped HTSC and it was interpreted as the opening of a pseudogap below a temperature $T^* > T_c$ [13]. A similar suppression has been confirmed by tunneling experiment [89, 116], c-axis optical conductivity [105], specific heat experiment [78] and angle-resolved photoemission (ARPES) [122]. Since its discovery, a great effort has been devoted to understand the connection of the pseudogap with the superconductive state but no consensus has been achieved concerning the origin of the pseudogap phase [55, 117].

All the models reported in the licterature can be grouped in two main scenarios [95]. The first one involves preformed Cooper pairs under the temperature T^*, which become phase coherent under T_c. As an example we mention the pionering work by Emery and Kivelson [42]. Here the loss of coherence of the condensate is explained in term of phase fluctuations that, due to the low density of superconducting carriers (as compared to the standard 3D BCS superconductors), may wash out the long range order without breaking the Cooper pairs.

Another interesting theory is based on the notion of spin-charge separation [72, 92]: an hole can be theoretically treated as a bound state of a fermionic particle called spinon carrying only the spin and another bosonic particle called holon carrying only the charge. In strongly correlated system like HTSC the double nature of the charge carriers becomes more evident and spinons and holons behave like independent particles. In a mean-field description spinons pair together forming a gap in the spin excitation spectrum that is interpreted as the pseudogap, while holons undergo Bose-Einstein condensation at the critical temperature leading the system into the superconductive state.

In the second scenario, instead, the pseudogap is considered as a particular phase that is in competition with the superconductivity and it's characterized by an hidden order [23, 129]. Various candidates of this order were proposed in the course of these years in particular stripe and antiferromagnetic order or d-density wave order (DDW), which break a particular symmetry of the system. Among these models we cite the one proposed by Emery [43] in which, below a certain temperature T_0, an exotic phase characterized by an alternation of charged and insulating antiferromagnetic stripes is spontaneously formed. At a lower crossover temperature, antiferromagnetic correlations start to grow up and to pair quasiparticles while below T_c the Josephson coupling between charged stripes induces the coherence of the condensate.

The fact that T^* decreases moving towards the overdoped region is experimentally established, but the structure of the whole phase diagram and in particular the T^* dependence on the doping is nowadays an object of discussion. Two different behaviors of the pseudogap line were put forward depending on the above-mentioned different scenarios [55]. In the first scenario the T^*-line is supposed to be tangent the strongly overdoped side of the superconducting dome while in the case of a pseudogap competing with superconductivity, the T^*-line is expected to cross the T_c line at about optimal doping and to extend under the overdoped side of the superconducting dome, in a region where the superconductivity coexists with pseudogap.

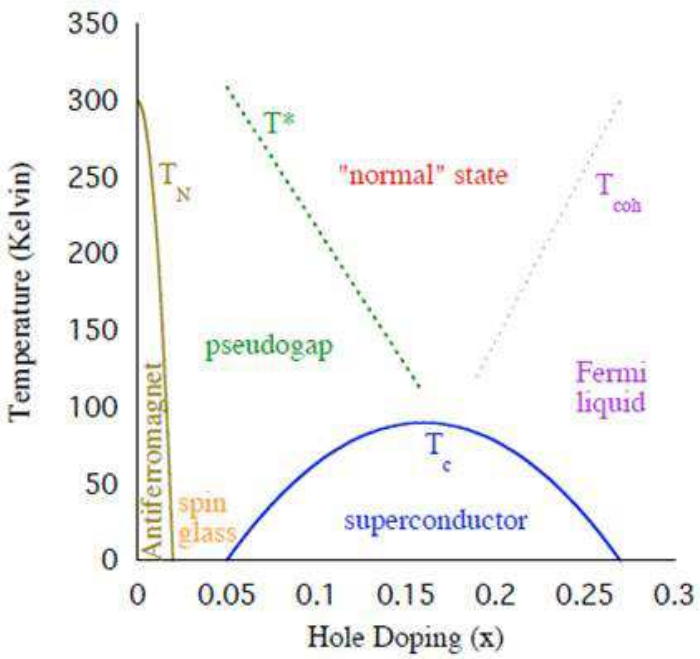

Figure 2.1: Phase diagram of an hole-doped cuprate. The solid lines represent the true thermodynamic phase transitions. The dotted lines indicate a crossover behaviour. Figure taken from [95].

2.4 Pairing mechanisms in HTSC

The possible models of the pairing mechanism in HTSC can be divided in two categories. The first one claims that the high critical temperature accompanied with a d-wave symmetry gap has an electronic origin and can be explained in terms of the strong Coulomb interaction [7, 102] (for example the RVB model by P.W. Anderson [6]). The second group argues that the binding of the electrons in Cooper pairs is mediated by a bosonic glue. Concerning the last hypothesis there is no consensus about the nature of this glue and a very hot debate is aimed at identifying whether a lattice vibration (phonons) [29, 36, 71, 80, 112] or a fluctuations of the spin polarization [1, 24, 109] is involved in the pairing process.
In conventional superconductors, the glue responsible for the formation of the Cooper pairs is given by the phonons. The BCS theory is only valid in the weak electron-phonon coupling approximation [9, 10]. The generalization of the BCS theory in the case of strong electron-phonon coupling has been carried on by Eliashberg [40, 93] and it takes into account the retardation effects of the phonons response. This work sets out from the Migdal theory of metals [85] based on the Green's-function methods of the many body theory and the finite temperature Matsubara formalism: all the effect of interaction with the lattice modes are summarized in the electron self-energy $\Sigma(\omega)$ that is written in terms of the one-electron Green function and phonon propagator, neglecting the vertex corrections. The main physical quantity of this theory is the glue function $\alpha^2 F(\Omega)$. $F(\Omega)$ is the phonon density of states, Ω being the phonon frequency and $\alpha^2(\Omega)$ the strength of the frequency dependent

electron-phonon interaction. The electron-phonon coupling constant λ provides the strength of the coupling integrated over the phonon frequencies:

$$\lambda = 2 \int \frac{\alpha^2 F(\Omega)}{\Omega} \, d\Omega \tag{2.5}$$

The critical temperature depends on λ and in the strong coupling regime this dependence can be explicated in the following expression obtained by McMillan [86]:

$$T_c = \frac{\tilde{\Omega}}{1.2} \exp\left[-\frac{1.04\,(1+\lambda)}{\lambda - \mu^*\,(1+0.62\lambda)}\right] \tag{2.6}$$

where $\tilde{\Omega}$ is the characteristic phonon frequency and is defined as an average over $\alpha^2 F(\Omega)$:

$$\tilde{\Omega} = \left\langle \Omega^2 \right\rangle^{\frac{1}{2}} \tag{2.7}$$

and

$$\left\langle \Omega^2 \right\rangle = \frac{2}{\lambda} \int_0^\infty \Omega \alpha^2 F(\Omega) \; d\Omega. \tag{2.8}$$

This formalism is not restricted to the case of phononic interactions but it can also be applied to a more general bosonic interactions.
Although there are many experimental results, like the high critical transition temperature, the d-wave symmetry of the gap and the small isotope effect on T_c, that seems to exclude a phonon-mediated glue in HTSC, there are as many other experimental evidences that electron-phonon coupling plays an important role in HTSC. For example Raman scattering and infrared optical spectroscopy [114] evidenced a strong electron-phonon coupling with certain phononic modes. Moreover the kinks in the energy dispersion, observed in ARPES spectra along the nodal direction of the Brillouin zone, are explained by interaction with phonons [28, 36] or with magnetic resonance modes [44, 97].
The Nearly Antiferromagnetic Fermi-liquid (NAFL) model was proposed by Pines and Scalapino and explains the pairing mechanism in term of spin fluctuations [87, 91, 109, 132]. It is based on the experimental observation that in the antiferromagnetic insulating phase the dynamical spin susceptibility is strongly peaked in the points $q = (\pm\pi, \pm\pi)$ of the Brillouin zone: this is equivalent to say that the spin fluctuations tend to zero at these points. The NAFL model claims that electrons on the Fermi surface in the vicinity of the $(\pm\pi, \pm\pi)$ points scatter more strongly with the other electrons at the Fermi level, connected by a vector q. In that way, the resulting coupling is more effective in the antinodal region and it has a d-wave symmetry as confirmed experimentally.

2.5 Hole superconductivity and kinetic energy lowering

The theory of hole superconductivity has been proposed by J.E. Hirsch and F. Marsiglio to explain the phenomenology of the HTSC [52, 53, 51, 83]. It is based on the asymmetric dynamical behavior of electrons and holes near the Fermi level. The motion of an hole in a full band costs an amount of energy due to the disruption

it causes in its environment, contrary to what happen to electrons. In the Hirsch model the occurrence of the superconductivity is explained in term of pairing between oxygen holes. The effective Hamiltonian that describes the propagation of holes through the oxygen anion network contains on-site repulsive interactions and a modulated hopping term that yields to a larger hopping amplitude between sites when other holes simoultaneously present.
This model provides an attractive interaction between nearest-neighbor holes with antiparallel spin with a critical temperature that depends on the hole density. When two holes couple together, they reduce their effective mass and can delocalize more efficiently: in other words they reduce the kinetic energy. The mechanism described here is totally different from the BCS theory. When a system is cooled down to the critical temperature, the value of the internal energy decreases. The internal energy is given by a sum of the interaction energy between carriers and the kinetic energy. For a BCS superconductor the superconductive transition is accompanied by an increase of the kinetic energy overcompensated by a decrease of the interaction energy. On the contrary, in the Hirsch's model the carriers directly lower their kinetic energy upon pairing. This result seems to find a confirmation in the optical spectral weight transfer from the visible region to the intraband transition region, observed in the optical spectra of HTSC (see chapter 3).

2.6 Non-Fermi liquid behavior

Another interesting aspect of HTSC is related to the non-Fermi liquid behavior found in the optimal and underdoped side of the phase diagram. In this region, a linear temperature dependence of the resistivity has been observed, in contrast to the T^2 dependence predicted by the Landau Fermi-liquid theory, revealing the failure of the concept of quasiparticles to describe the low lying energy excitations. Another difference between Fermi and non-Fermi liquid resides in the different shape of the momentum distribution function n_k at $T = 0$: in the first case n_k has a discontinuity Z_k for $k = k_F$, while in the second case the quasiparticle spectral weigth Z_k is zero [31, 98].
Moving in the phase diagram towards the overdoped region, the superconductive phase is observed to fade and the physics of HTSC is believed to be metallic-like. The crossover between these two regimes supports the theories that explain the superconductity at high temperature in term of a quantum critical point [21]. The possible quantum phase transition occurs at zero temperature and at optimal doping but strongly affects the physical properties of HTSC at finite temperature: both the T^* line and Fermi-non Fermi liquid crossover line converge to this point. The experimental determination of this crossover line can be obtained by ARPES technique because of the possibility to discriminate the coherent and incoherent part of the spectral function and the close relation between these quantities and Z_k: $\int A_{coh}\, d\omega = Z_k$ and $\int A_{incoh}\, d\omega = 1 - Z_k$.
Recently, employing these relations and studying the evolution of the bilayer band splitting in the nodal direction, Fournier*et al.* [46] found that, below a critical hole doping, Z_k suddenly drops to zero, directly demonstrating the non-Fermi liquid behavior of HTSC at an hole doping concentration below 10-15%.

Chapter 3

Optical properties of HTSC

3.1 Introduction

This chapter is divided in two main parts. In the first part we introduce the extended Drude model which is used to describe the far-infrared optical properties of the HTSC and allows us to determine the electron-boson coupling function directly from the equilibrium optical measurements. Afterwards the problem of the sum rule violation in cuprates is presented. The second part of the chapter deals with the non-equilibrium optical properties of HTSC. After a brief overview of the state of the art of the experimental results obtained by the time-resolved reflectivity measurements, we describe the Rothwarf-Taylor model which gives a phenomenological explanation of the non-equilibrium dynamics in the superconductive phase. The chapter ends with a brief description of a simple model proposed to simulate the temporal dependence of the electronic and phononic temperatures of a system excited by an ultrafast laser pulse.

3.2 Equilibrium optical properties of HTSC

Optical spectroscopy constitutes a powerful tool to investigate the electronic properties of solids, since it provides direct information about the underlying electronic structure [37, 125, 133]. The Drude-Lorentz model describes very well the optical properties of a good metal: it is based on the hypothesis that electrons in the conduction band constitute a classical gas of non-interacting particles. Within this model, the optical conductivity $\sigma(\omega)$ is given by:

$$\sigma(\omega) = \frac{1}{4\pi} \frac{\omega_{pD}^2}{1/\tau_D - i\omega\tau_D} + \frac{1}{4\pi} \sum_i \frac{\omega_{p,i}\omega}{i\left(\omega_i^2 - \omega^2\right) + \omega/\tau_i} \tag{3.1}$$

The first term (Drude term) is related to the intraband optical transition and describes the motion of the free carriers, $\omega_{p,D}$ being the Drude plasma frequency and $1/\tau_D$ the free carriers scattering rate. The second term describes the interband optical transition in terms of a sum of optical oscillators with characteristic plasma frequencies $\omega_{p,i}$, resonance frequencies ω_i and relaxation times τ_i.

3.2.1 Extended Drude model

The Drude model has been applied successfully to describe the optical properties of a large number of metals but in the case of a strong interaction between electronic carriers and bosonic excitations, it fails to be a good approximation. The generalization of the Drude model to the case of boson-assisted optical transitions is called Extended Drude model (EDM) [4, 3]. This model has been used for the first time by Allen to analyze the far infrared optical response of the metals at T=0 and later on it was generalized to the case of finite temperature [112]. In the following years the EDM has been extensively applied to strongly correlated materials like HTSC. In the EDM all the effects of the strong interactions are accounted for by an optical self-energy $\Sigma_{opt}(\omega)$, which is sometimes called also memory function:

$$\Sigma_{opt}(\omega) = \Sigma'_{opt}(\omega) + i\Sigma''_{opt}(\omega) = \frac{1}{\tau(\omega)} - i\omega\lambda(\omega). \tag{3.2}$$

The resulting expression of the complex conductivity turns out to be:

$$\sigma(\omega) = \frac{1}{4\pi}\frac{\omega_p^2}{\Sigma_{opt}(\omega) - i\omega} = \frac{1}{4\pi}\frac{\omega_p^2}{\frac{1}{\tau(\omega)} - i\omega(1+\lambda(\omega))} \tag{3.3}$$

where:

$$\lambda(\omega) = \frac{m^*}{m} - 1 \tag{3.4}$$

The real part of the optical self-energy (3.2) is a frequency dependent scattering rate due to the electron-phonon scattering (in the Drude model the inelastic impurity scattering makes the scattering rate a constant), while the imaginary part $\lambda(\omega)$ is related to the renormalization of the electronic effective mass due to the strong correlations [11]. The optical self-energy $\Sigma_{opt}(\omega)$ has the same analytical properties of the one-particle self energy $\Sigma(\omega)$ (averaged over the Fermi surface) used in the Green function theory, but conceptually it is a different quantity. $\Sigma(\omega)$ is directly measured by a photoemission experiment, since this technique probes the single particle excitations of the (N-1) particle system, which can be described in terms of the spectral function and the single particle self energy. An optical experiment, instead, looks at the particle-hole excitations of an N-particle system and gives information about the joint particle-hole density of states. In the so-called Allen approximation [4], $\Sigma_{opt}(\omega)$ can be write as a convolution integral between a transport spectral function $\alpha_{tr}^2 F(\Omega)$ and a kernel function $K\left(\frac{\omega}{2\pi T}, \frac{\Omega}{2\pi T}\right)$ which describes the thermal dependence of the phononic excitations coupled with electrons.

$$\Sigma_{opt}(\omega) = -2\int_0^\infty \alpha_{tr}^2 F(\Omega) K\left(\frac{\omega}{2\pi T}, \frac{\Omega}{2\pi T}\right) \tag{3.5}$$

where

$$K(x,y) = \frac{i}{y} + \left\{\frac{y-x}{x}\left[\Psi(1-ix+iy) - \Psi(1+iy)\right]\right\} - \{y \to -y\} \tag{3.6}$$

and $\Psi(x)$ is the Digamma function. The quantity $\alpha_{tr}^2 F(\Omega)$ is different from that defined in 2.5 and refers to a transport property of the sample. An interesting method

to determine $\alpha^2_{tr}F(\Omega)$ directly from the raw data was found by Marsiglio [81] and it is based on the second derivative of the conductivity with respect the frequency:

$$\alpha^2_{tr}F(\Omega) = \frac{1}{2\pi}\frac{\omega_p^2}{4\pi}\frac{d^2}{d\omega^2}Re\left(\frac{1}{\sigma(\omega)}\right) \tag{3.7}$$

The Maximum Entropy Method has been recently used to extract $\alpha^2_{tr}F(\Omega)$ from the optical scattering rate $1/\tau(\omega)$ but it produces unphysical negative values of this quantity [58].
The microscopic derivation of the complex conductivity $\sigma(\omega)$ in the presence of strong electron-phonon correlations is achieved starting from the Kubo formula and using complex diagrammatic techniques to evaluate the electron and phonon Green functions. Omitting the vertex corrections (Migdal approximation) it is possible to simplify the calculations and to obtain an expression of $\sigma(\omega)$ in terms of the one-particle self-energy function:

$$\sigma(\omega,T) = \frac{i\omega_p^2}{4\pi\omega}\int_{-\infty}^{+\infty}\frac{f_{FD}(\omega+\epsilon,T) - f_{FD}(\epsilon,T)}{\omega - \Sigma(\omega+\epsilon,T) + \Sigma^*(\epsilon,T) + i\Gamma_{imp}}\,d\epsilon \tag{3.8}$$

where ω_p is the plasma frequency, $f_{FD}(\omega)$ is the Fermi-Dirac distribution function and Γ_{imp} is the impurity scattering contribution. $\Sigma(\omega)$ and $\Sigma^*(\omega)$ are the electron and hole self-energies, respectively, and are obtained averaging $\Sigma(\omega,\mathbf{k})$ over the Fermi surface and assuming a constant density of states. In this case $\Sigma(\omega,T)$ is given by a convolution integral between the glue function $\alpha^2F(\Omega)$ and a new kernel function $L(\omega,\Omega,T)$ [67]:

$$\Sigma(\omega,T) = \int_0^\infty \alpha^2F(\Omega)\,L(\omega,\Omega,T) \tag{3.9}$$

The kernel function is the result of the integration of Bose-Einstein ($n_{BE}(\omega)$) and Fermi-Dirac functions:

$$L(\omega,\Omega,T) = \int\left[\frac{n_{BE}(\Omega') + f_{FD}(\Omega)}{\Omega - \epsilon + \Omega' + i\delta} + \frac{n_{BE}(\Omega') + 1 - f_{FD}(\Omega)}{\Omega - \epsilon - \Omega' - i\delta}\right]d\Omega' \tag{3.10}$$

The last integral can be analytically solved obtaining:

$$L(\omega,\Omega,T) = -2\pi i\left[n_{BE}(\Omega) + \frac{1}{2}\right] + \Psi\left(\frac{1}{2} + i\frac{\Omega-\Omega'}{2\pi T}\right) - \Psi\left(\frac{1}{2} - i\frac{\Omega+\Omega'}{2\pi T}\right) \tag{3.11}$$

The first term contains the distribution of the bosons while the second term (sum of digamma functions) is the result of the Fermi-Dirac function integration. This formalism is valid not only for phonons but it can be extended to a general electron-boson interaction. In the case that the charged carriers lose energy coupling magnetically with their spins, the boson glue has the following notation $I^2\chi(\Omega)$, because in the spin-fluctuation interaction model, the coupling function is proportional to the imaginary part of spin susceptibility. In the case of an unknown coupling mechanism it's possible to define a glue function given by the sum of the contribution of all the scattering bosons:

$$\Lambda(\Omega) = \alpha^2F(\Omega) + I^2\chi(\Omega) + \text{other bosons} \tag{3.12}$$

The strong electron-boson coupling formalism is based on the hypothesys that electrons behave like Fermi-liquid particles and it is supposed to properly describe the optical response of an HTSC in the overdoped region. Following the work of van Heumen *et al.* [127, 124, 126] it is possible to generalize the eq. (3.12) and define a new glue function Π that, convoluted with the kernel function (3.11) and put in eq. (3.8) reproduces the measured conductivity. Π is assumed to be a multi-step function and it is obtained by the best fit to the experimental data. It has been recently demonstrated that the Π extracted at room temperature reproduces the data down to 100 K, confirming that the strong coupling formalism is applicable in a large range of temperature. A common feature of $\widetilde{\Pi}$, found at all doping regimes and at all temperatures, is a broad spectrum that extends up to 400 meV and an intense peak at 50-60 meV, that corresponds to the kink observed in the nodal direction in ARPES spectra [65, 138] and with the peak-dip-hump structure of the tunneling spectra.

3.2.2 Sum rules

The optical constants in solids satisfy simple integral relations, called sum rules. The global sum rule states that the integral, over all the energy bands, of the imaginary part of the dielectric function $\epsilon(\omega)$ is a constant independent of the temperature and it is proportional to the ratio between the density and the mass of the carriers:

$$\frac{1}{4\pi}\int_0^\infty \omega\, Im\epsilon(\omega)\; d\omega = \frac{\omega_p^2}{8} \tag{3.13}$$

The integral that appears in (3.13) is called spectral weight SW. Choosing an appropriate cutoff frequency ω_c, the integral (3.13) can be split into the sum of an intraband (SW_D) and an interband spectral weight (SW_{inter}). In a BCS superconductor below T_c, the spectral weight removed in the far infrared region of the dielectric function, related to the opening of a gap Δ, is recovered by the formation of a peak at $\omega = 0$ associated to the dissipationless response of the condensate. The transition to the superconductive state does not affect the interband optical region and no experimental variation of SW_{inter} has been detected (i.e., $SW^N_{inter} = SW^{SC}_{inter}$). These results are summarized by the Ferrer-Glover-Tinkham (FGT) sum rule [118]: $D = SW^N_D - SW^{Sc}_D$ where D is the condensate spectral weight.
The work by Hirsch *et al.* about the superconductivity driven by a kinetic energy lowering (see chapter 2.5) [53, 51], triggered the interest of various experimentalists looking for a possible violation of the FGT sum rule. This violation is explained in terms of a spectral weight transfer from the interband to intraband optical regions or viceversa, i.e., the FGT sum rule has an additional term and can be written as:

$$D = (SW^N_D - SW^{Sc}_D) + (SW^N_{inter} - SW^{Sc}_{inter}) \tag{3.14}$$

In the specific case of an optical process described by an Hamiltonian with near-neighbour hopping, the total intraband spectral weight can be related to the average kinetic energy $\langle T_\delta \rangle$ of the charged carriers (holes) associated to the hopping process in the δ direction through the relation:

$$\frac{1}{4\pi}\int_0^\infty \omega\epsilon_D(\omega)\; d\omega = \frac{\pi^2 a_\delta^2 e^2}{2\hbar^2 V_{Cu}}\langle -T_\delta \rangle \tag{3.15}$$

where a_δ is the lattice spacing in the $Cu-O$ plane, along the direction determined by the in-plane polarization δ of the incidence light and V_{Cu} is the volume per Cu atom.
Recently, a superconductivity-induced decrease of SW_{inter} has been reported in optimally and underdoped HTSC [15, 20, 70, 82, 90, 107, 108, 125] (see fig. 3.1). These results have been interpreted as an increase of SW_D corresponding to a gain in the kinetic energy. On the contrary, in the over-doped region an opposite change of SW_{inter} is detected, accordingly to a BCS-like behavior at high dopings. Although the estimated kinetic energy gain is of the same order than the one predicted by the hole-superconductivity models, the equilibrium spectroscopic techniques didn't definitely clarify whether the spectral weight shift observed is related to a real modification of the electronic properties in the visible region or simply to a temperature-related narrowing of the Drude peak [66, 96]. In addition, the inability of resolving small reflectivity variations and the finite cut-off necessary to evaluate the optical integral prevented these techniques from addressing the major question whether the measured spectral weight variation is equally spread over all the interband transitions or related to particular electronic states participating in the condensate formation.

3.3 Non-equilibrium optical properties of HTSC

The recent development of ultrafast laser sources enabled the study of non-equilibrium properties of several materials included the HTSC. In time-resolved optical experiments an ultrafast laser pulse (pump pulse, ∼100 fs) excites the electronic carriers above the Fermi level E_F while a second delayed pulse monitors the evolution of the system back to the initial equilibrium state. If the probe pulse is monochromatic, the experimental technique is named one-color pump-probe reflectivity, while probing the photoinduced variation of the reflectivity (or transmissivity) with a broad spectrum or with a tunable wavelength pulse permits to perform a time-resolved optical spectroscopy and to measure the temporal dynamics of the dielectric function on the femtosecond time scale.
Time-resolved optical properties of metals and semiconductors have been extensively studied and many works, both experimental and theoretical, have been published during the last 30 years [54]. The physics that describes the interaction of the electronic and lattice degrees of freedom with an ultrafast light pulse is quite well understood in these materials.
In the specific case of the metals, electrons are excited from occupied to non-occupied states above the Fermi level E_F and then thermalize, through inelastic scattering processes, on a characteristic timescale of few femtoseconds. The electron-electron thermalization occurs in a time $\tau_{e-e} \sim \frac{\hbar E_F}{2\pi E^2}$ where E is the carrier energy measured with respect to E_F. Considering that in metals $E_F \sim 10$ eV and $\hbar$=0.658 eV·fs, $\tau_{e-e} \sim 4$ fs for electrons excited at 0.5 eV above E_F that is significantly faster compared to the pulse temporal width. Since τ_{e-e} is much shorter than the period of the typical phonon modes, the electronic system, in this time interval, is not coupled to the lattice and reaches a temperature T_e higher than the phonon bath temperature T_{ph}. The final value of the temperature T_e depends on the pulse energy and is larger than T_{ph} because the heat capacity of the electrons is much smaller than the lattice heat capacity. After the thermalization, the excited electrons start to loose

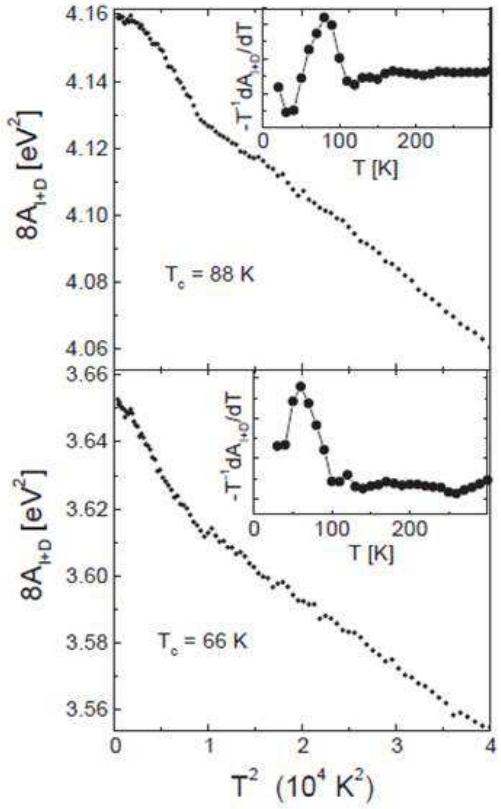

Figure 3.1: Temperature dependence of the intraband spectral weight SW_{inter} for optimally (top) and underdoped (bottom) $Bi_2Sr_2CaCu_2O_{8+\delta}$ obtained by integrating the optical conductivity up to 1.25 eV. At T_c SW_{inter} breaks away from the approximately T^2 behaviour and shows an anomalous rise, meaning that the kinetic energy of the carriers lowers in the superconducting state [90].

energy through electron-phonon scattering processes and relax towards the states near the chemical potential. Allen developed a theoretical two-temperature model (2TM) [5] which describes the electron-phonon relaxation in metals and obtained a simple expression of the electron-phonon relaxation time τ_{e-ph} in terms of T_e, the mean square phonon frequency $\langle\omega^2\rangle$ and λ:

$$\tau_{e-ph} = \frac{\pi k_b T_e}{3\hbar\lambda\langle\omega^2\rangle} \tag{3.16}$$

Allen's model represents an interesting method that allows to derive λ more directly than other experimental techniques. In fact τ_{e-ph} can be obtained fitting $\Delta R/R$ to an exponential decay while $\langle\omega^2\rangle$ is taken from the literature or can be approximated by $\omega_D^2/2$. The 2TM model has been successfully applied to different metals obtaining a λ that ranges between 0.05 and 0.15 in agreement with the data obtained by other experimental techniques. This formalism has been employed also in HTSC in normal state, where there's no gap in the excitation spectrum and the system seems to have a pseudo-metallic behaviour: the λ extracted from transient reflectiv-

ity measurements was found to increase to 0.82 in the case of Bi2212 [18, 17].
Before reviewing the state of art of the time-resolved techniques on HTSC, we focus on the physical origin of the change of the optical properties in these experiments. In metals, the relative change of the reflectivity ($\Delta R/R$) can be accounted for by simple thermal effects. The heating of the electrons induced by the pump pulse modifies the carrier population, smearing the electronic distribution function $f_{FD}(\omega, T)$. In other words the thermal broadening of $f_{FD}(\omega, T)$ induces an increase of the occupation of states above E_F and a depletion of states below E_F which is revealed as a change in reflectivity. This mechanism is responsible for a small relative reflectivity variation on the order of $\Delta R/R \sim 10^{-4}$-10^{-5}.
Time-resolved reflectivity measurements performed on HTSC under T_c reveals some important differences as compared to metals.
First, the opening of a gap in the excitation spectrum at $T<T_c$ causes the slowering of the relaxation dynamics with a decay time τ that increases of about one order of magnitude (from ~ 100 fs to ~ 1 ps).
In this case when the pump pulse breaks a Cooper pair, a quasiparticle pair is created with energy larger than the superconductive gap. In this non-equilibrium condition, the recombination process of quasiparticles is accompanied by the emission of an high energy ($\hbar\omega > \Delta$) boson that is responsible of the pairing. Since the boson has enough energy to break another pair, an avalanche process of creation of quasiparticles grows up. The recovery time of this process is determined by the decay time of the bosons. A slowing of the recombination dynamics of the bosons (boson bottleneck) brings to the increasing of the decay time of $\Delta R/R$. This mechanism is well described by a set of coupled differential equations that constitute the Rothwarf-Taylor model [106]. This phenomenological model is able to explain the bottleneck of the dynamics in superconductive state and will be described more deeply in section (3.3.3).
Second, another anomalous behaviour distinctive of the cuprates below T_c, is given by a substantial increase of the signal $\Delta R/R$ as compared to the relative variation measured in metals. In particular, a $\Delta R/R$ of the order of 10^{-3}, about 1-2 order of magnitude larger than normal metals, is measured in HTSC. The origin of the $\Delta R/R$ variation has been extensively discussed in these last years and has been subject of different interpretations [33, 49, 62].
i) A possible explanation of this result is given in terms of the spectral weight shift from the interband to intraband optical regions observed in equilibrium optical measurements. In a pump-probe experiment on a superconductor, the effect of the pump is to drive the system towards the normal state. When an high density of quasiparticles is photoinjected in the system, the superconductive gap can be totally or partially quenched and part of the condensate spectral weight shifts to higher energy, i.e., in the same energy region investigated by the probe pulse [48]. The $\Delta R/R$ change of sign recently observed under the T_c is compatible with the change of spectral weight shift that occurs in overdoped region [48].
ii) The photoinduced signal is interpreted also as a simple result of an excited state absorbtion from photoexcited quasiparticles states, similar to what occurs in metals [33]. This interpretation does not account for the dramatic large $\Delta R/R$ values measured in the superconducting phase and will be extensively discussed and ruled out in the next chapters.

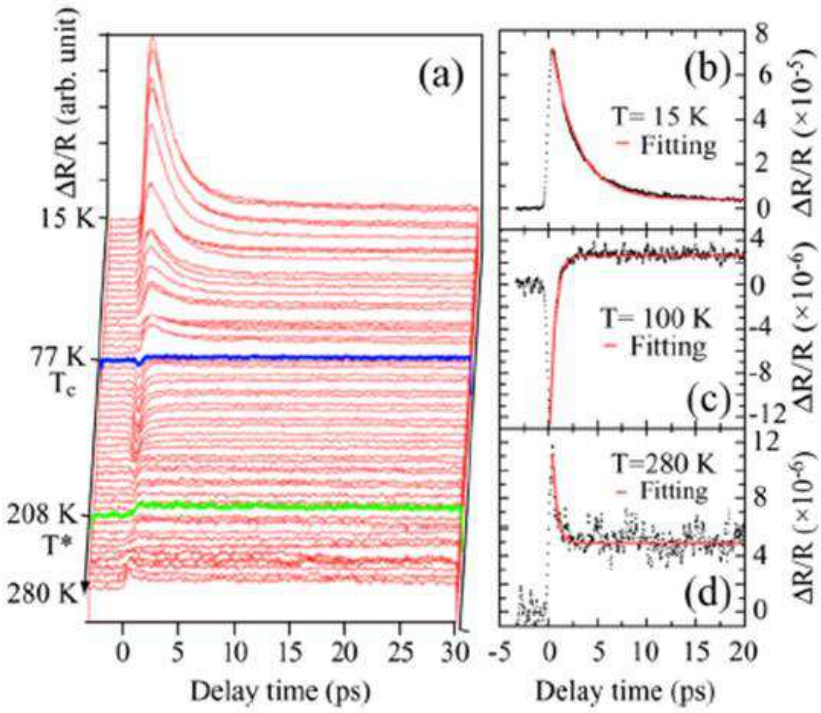

Figure 3.2: (a) Temperature dependence of $\Delta R/R$ on Bi2212. The blue line marks the transition from pseudogap to superconductive phase. While the green line is interpreted as the transition from pseudogap to normal state. (b-c-d) Transient reflectivity measured respectively in superconductive, pseudogap and normal state [76].

3.3.1 State of the art

The main purpose of the time-resolved optical measurements is not only to study the optical properties of the HTSC far from the equilibrium condition but also to clarify several unsolved aspects of the equilibrium properties of these materials.
In this paragraph we summarize the most significant experimental results obtained by optical pump-probe measurements. A characteristic common to most of cuprates is the sensitivity of time-resolved measurements to the phase of the system. The optical response changes drastically with the temperature as we can appreciate in the fig. 3.2 [76]: in the normal state the transient variation of reflectivity is fast (about a hundred of fs) and positive while as the sample enters in the psedogap phase a negative and fast component appears and dominates over the previous one as the temperature is further lowered. When the system is cooled below T_c, ΔR increases rapidly and the relaxation time τ drops to 2.5 ps.
The peculiar capacity of the time-domain spectroscopy to disentangle different excitations on the base of their decay-time has been employed in the past to address the complicate problem of the interplay between the superconducting and pseudogap phases. As reported in the previous section, the presence of the gap strongly affects the transient behaviour of $\Delta R/R$. In the strong boson bottleneck regime,

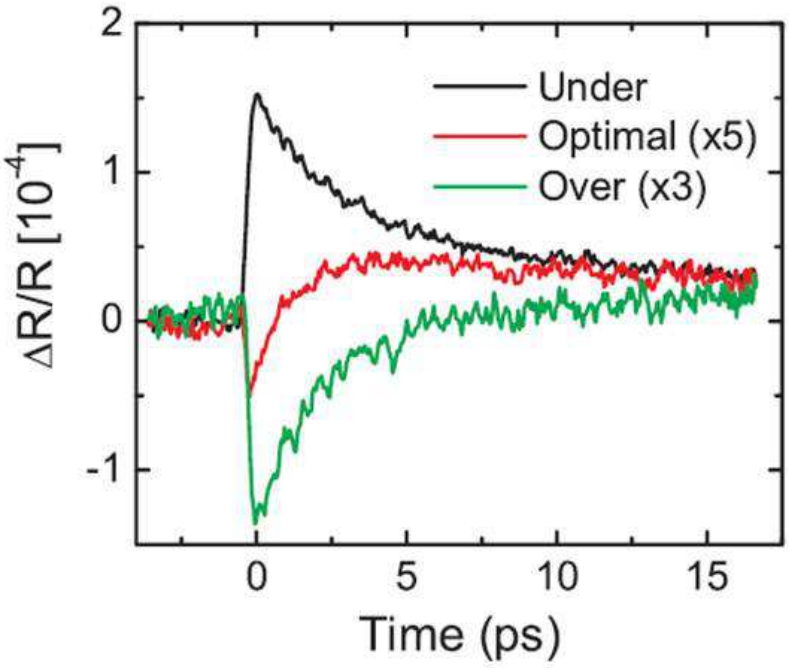

Figure 3.3: Transient variation of the reflectivity measured on Bi2212 at different doping range. Adapted from [48]

the photoinjected quasiparticles accumulate above the gap because their recombination rate depends on the anharmonic decay of the bosons. When the temperature increases and approaches T_c the superconducting gap closes. Since only the boson with energy $\hbar\omega > 2\Delta$ can break a Cooper pair, when Δ decreases, a large number of bosons has enough energy to create pair of quasiparticles. It is for this reason that the decay time diverges like $1/\Delta$ as T_c is approached from below. The temperature dependence of τ has been measured and analyzed in many works. In fig. 3.4 the value of the decay obtained by a multicomponent fit of the transient signal is shown. Above T_c the signal is well reproduced by a single exponential decay, while in the superconductivity phase two distinct components with different relaxation times are resolved: the first τ shows the expected divergence at $T=T_c$, the second is found to be temperature independent. The measurement of two different relaxation dynamics under T_c has been interpreted as a possible coexistence of the two gaps under the superconductive dome.
Another important result comes from the experimental observation that the temporal dynamics of $\Delta R/R$ in optical pump-probe experiment is equivalent to that measured in optical pump-terahertz probe experiments. Since in the last technique the imaginary part of the transient conductivity is directly proportional to the condensate density, this is considered as the proof that the $\Delta R/R$ variation in the near-IR/visible spectral range is proportional to the density of photoinjected quasiparticles. All the mentioned results are obtained in a regime of low perturbation i.e. when the intensity of the pump is not large enough to completely destroy the superconducting phase [47, 50, 110].

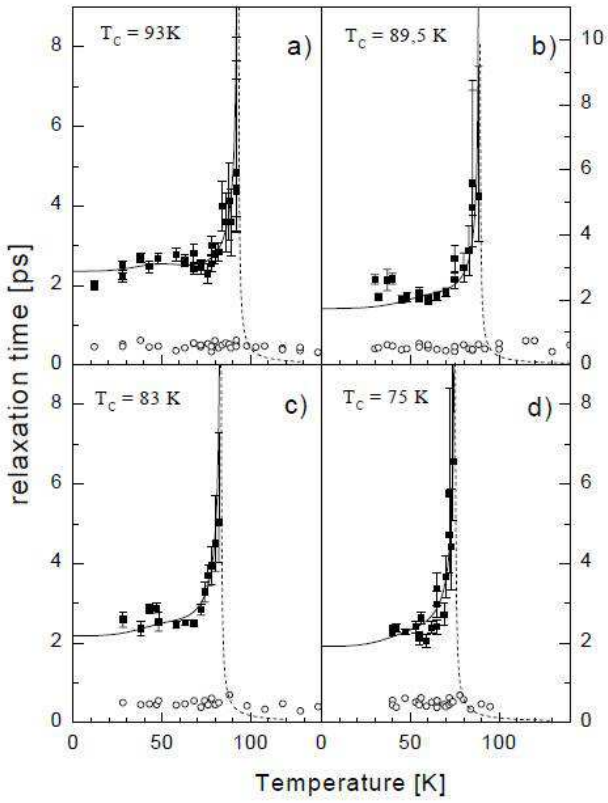

Figure 3.4: Relaxation times resulting from a two component fit of $\Delta R/R$ on $Y_{1-x}Ca_xBa_2Cu_3O_{7-\delta}$ at different doping. The relaxation time τ_a diverges at T=T_c while τ_b is found to be completely T-independent. The presence of this dynamics below T_c suggests the coexistence of two distinct gap below T=T_c [34].

3.3.2 Rothwarf-Taylor equations

In this subsection we give an overview of the Rothwarf-Taylor model (RT model) which provides a phenomenological description of the photoinduced non-equilibrium dynamics of superconductors. The RT model consists in two coupled differential equations describing the temporal evolution of a quasiparticles system, created by the laser-induced breaking of Cooper pairs, followed by the process of recombination into the condensate. The process of recombination is mediated by the emission of a boson at the same energy of the superconductive gap. The coupled differential equations describing the dynamics of the quasiparticle excitation density $n(t)$ are:

$$\begin{aligned} \dot{n} &= I_{QP}(t) + 2\gamma p - \beta n^2 \\ \dot{p} &= I_{Bos}(t) - \gamma p + \frac{\beta n^2}{2} - \gamma_{esc}(p - p_T) \end{aligned} \tag{3.17}$$

where p is the boson density with energy $\hbar\omega \geq 2\Delta$. $I_{QP}(t)$ and $I_{Bos}(t)$ are respectively the number of quasiparticles and boson photoinjected per cm^3 per second: for both these quantities we assume the same gaussian temporal profile of the incident

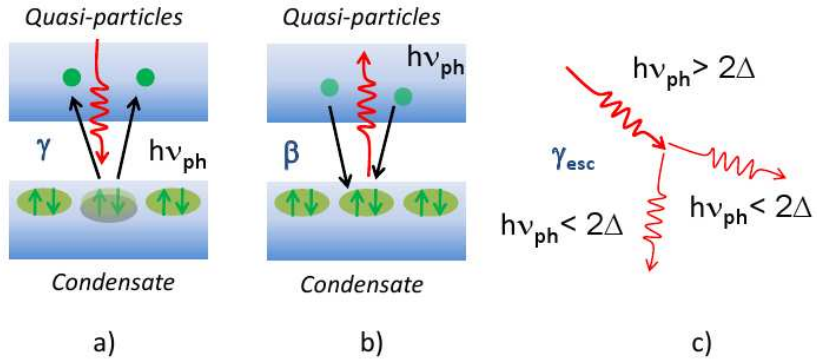

Figure 3.5: Three physical process described by the RT model: (a) Creation of a pair of quasiparticles above the superconductive gap by absorption of a boson. (b) Annihilation of two quasiparticles via emission of a boson. (c) Anharmonic decay of high frequency bosons [35].

pulse. $2\gamma p$ is the rate of electron-hole pair creation by annihilation of a gap energy boson, while βn^2 is the inverse process i.e. the rate of annihilation of two quasiparticles via emission of a boson. The parameter γ_{esc} is the boson decay rate due to anaharmonic processes or to the diffusion out of the excited volume.
In the case $\gamma_{esc} < \gamma$, the probability that bosons are scattered and create a couple of quasiparticles is higher than the one to lose energy via the interaction with low-frequency bosons. In this regime the boson density increases until an equilibrium with the excited quasiparticles is reached. This is possible when the rate of creation γ compensate the rate of annihilation β. At this point quasiparticles and boson are strongly coupled and both decay at the rate γ_{esc}. Usually $1/\gamma_{esc}$ is of the order of a few picoseconds.
Although it is well-known that BCS superconductors are in the regime of strong phonon bottleneck, it is far from the agreement which regime properly describes the non-equilibrium dynamics of HTSC.

3.3.3 Electron-boson coupling

One of the outstanding problems connected to the origin of HTSC is to determine which are the bosons mediating the formation of Cooper pairs. In particular, the determination of the electron-boson coupling strenght λ allows to shine light on the mechanism of pairing. So far, the parameter λ has been determined by different experimental tecniques i.e. inelastic neutron scattering, optical conductivity, ARPES and tunneling spectroscopy but with contrasting results ranging from a weak coupling regime ($\lambda \sim 0.1$) to a strong coupling regime ($\lambda \geq 1$). All these tecniques allow to extract the electron-boson coupling function through a complex procedure of inversion of the experimental data. The constant λ is finally obtained by integration of the coupling function over the boson frequencies up to a given cutoff frequency.
The peculiarity of time-resolved measurements is in the possibility to directly extract the coupling constant λ from the experimental data in the time domain.

Table 3.1: Fitting parameters obtained by numerically integrating the differtial equation7.15. The smallest and highest values of f and $\lambda\Omega_0^2$ correspond to the choice Ω_0=40 meV and Ω_0=70 meV. Data taken from [101]

T_l	f	$\lambda\Omega_0^2$ (meV^2)	τ_β (ps)
30±10	0.13-0.25	300-380	2±0.1
300±10	0.18-0.25	340-380	0.9±0.1

Contrary to the standard equilibrium techniques it is possible to disentangle the contribution of different bosons on the base of the different relaxation dynamics. Time resolved techniques have been extensively used in the last years to determine λ in metals and in superconductors above T_c within the two temperature model (2TM). In the superconductive state the bottleneck in the recovery dynamics has prevented the determination of the effective strength of the electron-boson coupling. Very recently time-resolved photoemission spectroscopy on cuprates has been performed by L. Perfetti *et al.* [101]. In this experiment the sample is excited by an ultrashort infrared pulse (1.5 eV) while a second delayed pulse (6 eV) probes the transient electron distribution $f(\omega,\tau)$ by photoemitting electrons along the nodal direction. The temperature evolution $T_e(\tau)$ of the excited electron population is directly extracted fitting $f(\omega,\tau)$ at different delay time. The author observed two different dynamics of the extracted electronic temperature and developed a three-temperature model (3TM). They supposed that the excited electron are more strongly coupled with a subset of phonons and quickly reach the equilibrium at a temperature T_p in a few hundred of femtoseconds. The second dynamics is given by the thermalization with the cold lattice at the temperature T_l and it occurs with a slower decay time ($\tau_\beta \sim 2\ ps$). Accordingly to the 2TM the rate of energy transfer between electrons and phonons is given by the integral $\int \Omega^2\alpha^2F(\Omega)(n_e-n_p)\,d\Omega$, where n_e and n_p are the Bose-Einstein distributions at the temperature of electrons T_e and phonons T_p, respectively. The spetral density of phonons is simplified considering only one phonon mode at Ω_0 between 40 meV and 70 meV, i.e., $F(\Omega)=\delta(\Omega-\Omega_0)$. The rate equations of the 3TM are:

$$\frac{dT_e}{dt} = -\frac{3\lambda\Omega_0^3}{\hbar\pi k_b^2}\frac{n_e-n_p}{T_e} + \frac{P}{C_e} \tag{3.18}$$

$$\frac{dT_p}{dt} = \frac{C_e}{C_p}\frac{3\lambda\Omega_0^3}{\hbar\pi k_b^2}\frac{n_e-n_p}{T_e} - \frac{T_p-T_l}{\tau_\beta} \tag{3.19}$$

$$\frac{dT_l}{dt} = \frac{C_p}{C_l}\frac{T_p-T_l}{\tau_\beta} \tag{3.20}$$

where P is the gaussian temporal profile of the incident pulse. The specific heat of the electrons, the strongly coupled phonons and the lattice are: $C_e=\gamma T_e$, $C_p = 3f\Omega_0\frac{dn_p}{dT_p}$, $C_l = 3(1-f)\Omega_0\frac{dn_p}{dT_p}$, and f is the fraction of the strongly-coupled phonons. Fitting the temporal profile of T_e with the numerical solution of the equation (7.15), one obtains the results displayed in the table (3.1).

Chapter 4

Time-resolved optical spectroscopy

4.1 Introduction

The experimental set up is described in detail in this chapter. Particular importance is given to the detection system and to the characterization of the supercontinuum light pulses used to probe the non-equilibrium dynamics of the sample in the visible optical region. At the end of the chapter we give a brief description of the setup used to extend the probe energy range in the infrared region down to 0.5 eV.

4.2 Optical oscillator

The first stage of the laser system is a diode pumped Nd:Yag laser (Coherent Verdi V10) which provides a beam with wavelenght λ=532 nm and maximum output power of 10 W. This laser pumps a Ti:sapphire oscillator (Coherent Mira 900) converting the input continuous wave beam into a train of ultrafast pulses characterized by a wavelenght λ=800 nm and a temporal width of 120 fs. The cavity of the oscillator is equipped by a cavity dumper which is an acousto-optical switch that allows to vary continuously the repetition rate of the laser from 1 MHz to 200 Hz and to increase the energy per pulse. The output energy per pulse is about 50 nJ at 100 KHz of repetition rate. This experimental configuration is particularly suitable to study the strong non-equilibrium regime in cuprates avoiding the avarage heating effects. Nevertheless it's necessary to underline that all the measurements presented in this thesis are done in a low perturbation regime without causing any superconductive to normal photoinduced phase transition.
At the output of the laser source, a telescope formed by two plano-convex lenses (L) placed at the distance 2f from each other (f is the focus length of the lens) collimates the beam and helps in obtaining a better focalization on the sample at the end of the line. The beam is divided in two part by a beam splitter (BS): the 70 % of the incident beam is trasmitted (pump) while the remaining 30 % is used as probe. The temporal delay between the two beam is varied by a motorized

high-precision translational stage, placed on the pump line, which is controlled via software and allows to change the optical path in step of 1 μm. Because of the double passage into the translational stage 1 μm corresponds to a temporal delay between pump and probe of 6.6 fs. The intensity of both the beams is tuned by an intensity attenuator given by an half-wave plate and a polarizer (P). Pump and probe are both focused on the sample with a plano-convex lens of 20 cm and 10 cm and have perpendicular polarizations to avoid any possible interference effect. A mirror placed on a piezoelectric motor allows to obtain a fine control of the spatial coincidence. Since the relative variations of the probe are very low (tipically of the order of 10^{-5} is necessary to minimize all the effects due to scattering of the pump. The size of the two beams are measured by imaging the spots in the focal plane on a CCD camera. The samples measured are placed in an open-cycle cryostat that can cool down to the minimum temperature of 10K.

4.2.1 One color pump-probe reflectivity measurements

In this type of measurement both pump and probe beams have the same wavelenght (λ=800nm). The signal acquisition is based on the lock-in detection. The intensity of the pump beam is modulated at a frequency of 3 KHz using a mechanical chopper. The probe signal reflected by the sample is parallelized using another lens of the same focal lenght f and is refocused on a photodiode (PD). The signal detected is acquired by a lock-in amplifier referenced to the modulation of the pump beam. Using a Fourier-transform based algorithm, this device extracts from the input signal the component modulated at the reference frequency. The frequency of the modulation is chosen in order to be high enough to minimize the $1/f$ noise and sufficiently lower than the repetition rate of the laser source. The signal to noise ratio provided by the lock-in acquisition scheme is further reduced by the fast scanning of the translator stage. The oscillatory movement of the scan delay is synchronized with the lock-in acquisition in a way that the first step of the translator coincides with the starting of the acquisition. Because of the fast scan, the integration time of the lock-in amplifier has to be reduced to 5 ms. If the total scan length is 1 mm (corresponding to a time window of 6.6 ps), the time required to perform a single scan is about 2 s. A good signal to noise ratio is obtained averaging 200-300 scan for a total duration of 6 min. The fast scanning acquisition scheme is particularly suitable to reduce the noise present on a time scale longer than the measured temporal dynamics, for example the intensity drift of the laser and the oscillations of the cryostat.

4.2.2 Femtosecond pump-supercontinuum probe spectroscopy

To develop this novel experimental technique we start from the experimental setup described in the last section introducing some modifications which are reported in the following.
Supercontiuum light is produced on the probe line, focusing the probe pulses with an aspherical lens into a photonic crystal fiber (the properties of the photonic crystal fiber will be extensively described in the next section). The fiber is positioned on a home-made launch system equipped by three traslational degrees of freedom and a

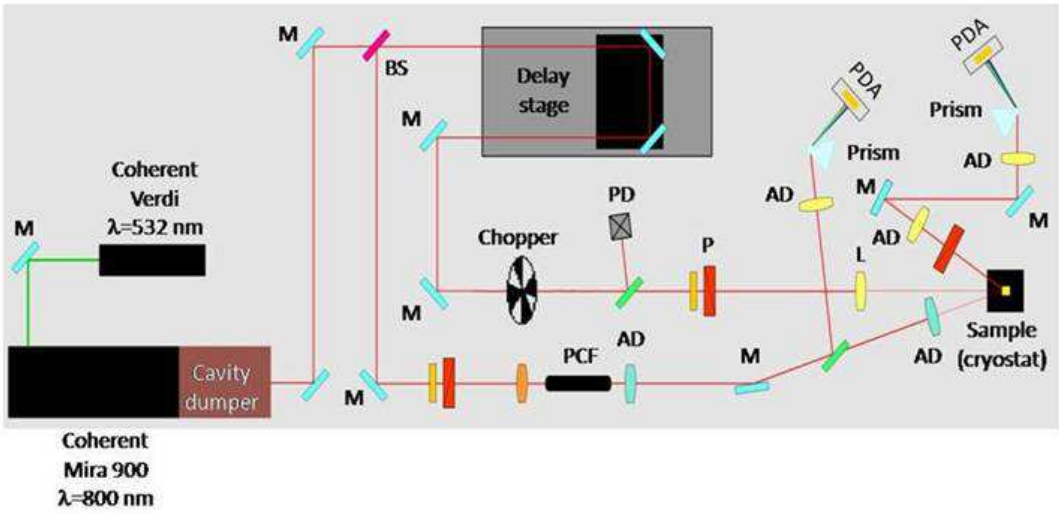

Figure 4.1: A schematic drawing of the experimental set-up.

tilting mechanism, in order to optimize the coupling of the laser into the fiber itself. Strongly non linear processes inside the fiber broaden the 800 nm pulse generating a broadband pulse characterized by a spectral content ranging from 450 nm to 1500 nm and a complex spectral chirp. More details on the temporal and spectral characterization of the supercontinuum light will be given in the next chapter. After the fiber the white light pulse is parallelized by an achromatic doublet (AD) and then refocused by another doublet with focal lenght f=100 mm. An optical window, placed before the last doublet, samples the probe. This reference is used to monitor and compensate the probe intensity during the measurements. Both the reference and the signal reflected by the sample are dispersed by a prism and collected by two Si-arrays of 128 pixels. A spectral slice, whose width ranges from 2 nm at 700 nm to 6 nm at 1100 nm, is acquired by each pixel of the array, corresponding to a constant temporal resolution of $\sim$120 fs [25]. A fast digitizer performs the scan of the arrays. Because of the large difference between the scan frequency of the array and the repetition rate of the laser, a single-shot detection is not feasible and it is necessary to integrate many pulses. The pump beam is chopped at a low frequency (typically 30 Hz), and, at the same time, the pump modulation is acquired by a photodiode and digitalized by a data acquisition device (NI-DAQmx M-series) which is synchronized with the fast digitizer. In this way it is possible to discriminate between pumped and the unpumped pulses. At the end of a single acquisition the pump-induced variation of signal is obtained by mediating and subtracting the two signals. To prevent the probe intensity fluctuations from affecting the measurement, the reflectivity variation is divided by the reference signal. The sensitivity of the array of photodiodes ranges from 500 nm to about 1000 nm, outside this range the response of the photodiodes drops. Only this portion of the supercontinuum light will be used in the measurements reported in this work.
In fig. 4.1 we sketch the pump-supercontinuum probe reflectivity experimental setup.

4.2.3 Supercontinuum light: physical features and characterization

Supercontinuum generation consists in a spectral broadening of a narrow-band light pulse generated by nonlinear process during the propagation in a medium [38]. Supercontinuum or white light was first generated and observed by Alfano and Shapiro in a bulk glass [2]. In the following years, supercontinuum light was generated in a wide range of non-linear materials, like solids, organic and inorganic liquids, waveguides and photonic crystal fiber. The physical mechanism behind the broadening of the spectrum is the combination of different non-linear phenomena like the self-phase modulation, the Raman scattering, the four-wave mixing and the soliton fission. Nowadays, supercontinuum generation constitutes an emerging tool in the field of ultrafast optical spectroscopies but the complexity of the spectral and temporal structure of the supercontinuum pulses requires a detailed characterization.
We developed a specific characterization technique based on a frequency-resolved optical gating through two-photon absorption in thick ZnSe plate (gap 2.1 eV). The gating pulse is the pump that is noncollinearly focused on the plate, in coincidence with the supercontinuum pulse. After the plate, the supercontinuum pulse is dispersed by a prism and collected on the linear photodiode array as reported in section (4.2.3). This method is based on the fact that carriers can be excited across the gap of ZnSe, through a two-photon absorption process only if temporal coincidence between part of its spectrum and the gate pulse, is realized. In this way the spectrogram of the pulse is obtained by measuring the transient absorbtion as a function of the time delay between the two pulses as we can see in fig. 4.2. The main advantage is that the two photon absorption process is not subjected to phase-matching condition as in the standard XFROG techniques.

4.2.4 Photonic crystal fiber

The supercontinuum light is generated in a photonic crystal fiber (PCF). This type of fiber exploits the light confinement properties typical of the photonic crystals: the core of the fyber has a diameter of 1.8 μm and the cladding is constituted by an ordered array of holes that run over the entire length of the fiber. An advantage to use photonic crystal fibers is the possibility to reduce the core size to few microns making the non-linear processes more efficient. Another peculiar characteristic is the possibility to modify the size and the order of the holes controlling the physical properties of the fiber. In particular our fiber is engineered to obtain a zero wavelength dispersion close to the seed pulse wavelength: this guarantees the maximum broadening of the spectrum and reduces the pump power requirements making possible the supercontinuum generation using unamplified input pulses.

4.3 Optical parametric amplifier

This set-up has been used to extend the spectral content of the probe also in the infrared region down to 0.5 eV. The main component of the setup is a solid-state diode-pumped Nd:vanadate (Nd:YVO^4) laser generating a continuous light with $\lambda = 532$ nm and power of 18 W. This laser is the pump of both an optical oscillator

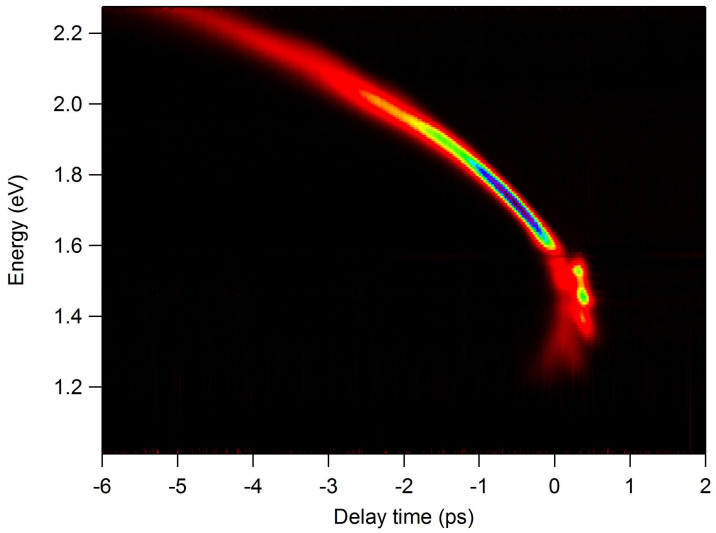

Figure 4.2: Supercontinuum pulse spectrogram measured through two-photon absorption in a ZnSe crystal.

(described in section (4.2.1) and a Regenerative amplifier (Coherent RegA Model 9050). The laser pulse provided by the oscillator is temporally stretched by a couple of diffraction gratings and it is switched into the cavity of the amplifier with a fast Pockels cell (electro-optic modulator). The pulse amplification is achieved by multiple passes through a gain medium, i.e, a Ti:sapphire crystal which is previously pumped and accumulates energy. After several trips in the cavity, the amplified pulse is switched out and it is compressed until reaching a minimum temporal delay of 50 fs. The repetition rate of the RegA is 250 KHz and the maximum energy per pulse increases up to a few μJ.
After the amplification the laser beam is split into two part: the first parts is focused on the sample while the other is used as the seed of an optical parametric amplifier (Coherent OPA 9850). The working principle of this optical device is based on the non-linear process of optical parametric generation. In this process the pump photon (ω_p), strongly interacting with a non-linear crystal, is converted into two photons called signal and idler with frequencies respectively ω_s and ω_i respectively. The sum of their frequency is fixed by the value of the pump frequency, and by the energy conservation principle: $\omega_p = \omega_s + \omega_i$. Their values are determined by the phase matching conditions which change varying the angle between the pump and the optical axys of the crystal. Changing these conditions it's possible to tune ω_s and ω_i in a frequency window that ranges from 1200 nm to 1600 nm for the signal and from 1600 nm to 2400 nm for the idler.

Chapter 5

Physical properties of $Bi_2Sr_2Ca_{0.92}Y_{0.08}Cu_2O_{8+\delta}$

5.1 Introduction

In this chapter, the equilibrium optical measurements carried on a sample of Y-doped Bi2212, are reported in a large frequency region ranging from the far-infrared to the ultraviolet. Before showing the experimental measurements, we spend few words on the physical optical properties of the sample. The equilibrium dielectric function is well reproduced by a sum of Lorentz oscillators and an extended Drude term. The origin of the interband oscillators is discussed. The electron-boson coupling function is determined directly from the fit assuming a model-independent histogram rappresentation.

5.2 Crystal structure of $Bi_2Sr_2Ca_{0.92}Y_{0.08}Cu_2O_{8+\delta}$

The bismuth strontium calcium copper oxyde superconductors are the most studied high-temperature superconductors together with yttrium barium copper oxydes (abbreviated YBCO). The general chemical composition of these compounds is $Bi_2Sr_2Ca_nCu_{n+1}O_{2n+6+\delta}$. The n=1 sample is called for the sake of simplicity Bi2212, referring to the ordered sequence of the metallic ions in the stoichiometric formula, and has attracted more attention than the other compounds of the same family. The main building blocks of the crystal structure are the CuO_2 planes that are separated between each others by additional BiO, SrO and Ca planes as we can see looking at the unit cell of the Bi2212 shown in fig.5.1. The superconductive currents are localized in the two-dimensional CuO_2 planes and they start to occur at low temperature upon doping the system with holes. This effect is obtained by adding interstitial oxygen atoms which take position in the BiO planes: the critical temperature strongly depends on the amount of extra-holes and in the specific case of $Bi_2Sr_2CaCu_2O_{8+\delta}$, it reaches the maximum value of 95 K in correspondence with an excess density of about 0.16 holes per Cu atom.
The stability of Bi2212 superconductors and the relative ease to cleavage, due to the

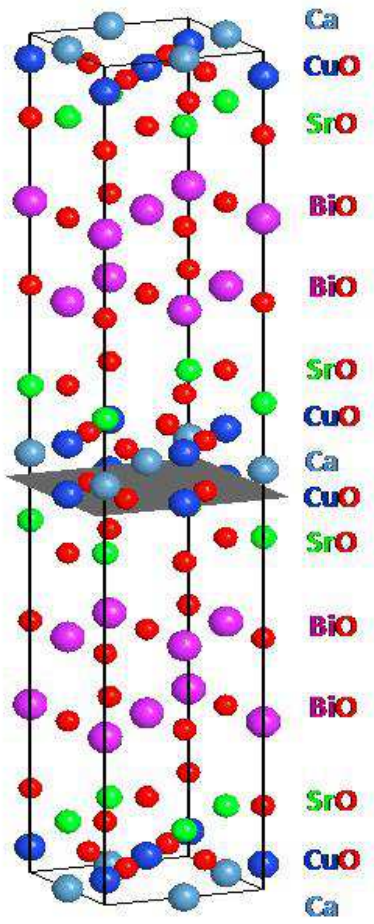

Figure 5.1: The unit cell of Bi2212.

weakness of the chemical bonds between BiO layers, make these samples particularly suited for electron spectroscopy studies. Although a large amount of experimental work on the Bi2212 have been published since now, several chemical properties are not well understood when compared to other HTSC. In particular the connection between the nanoscale inhomogeneity of the doped holes in the CuO_2 planes and the chemical inhomogeneity of the sample given by the excess of oxygen atoms in BiO layers, and consequently the connection between the former and the occurence of the superconductivity is still an object of study.
All the measurements we will show in the next chapters are performed on Yttrium doped Bi2212. The substitution of Yttrium for Calcium atoms has the effect to stabilize the 1:1 ratio between Bi and Sr sites and, for 8% of Y doping, to increase the maximum critical temperature to the value of 96 K. The resulting chemical formula of this compounds is: $Bi_2Sr_2Ca_{0.92}Y_{0.08}Cu_2O_{8+\delta}$. In the next section we will give more details on the preparation techniques of the samples.

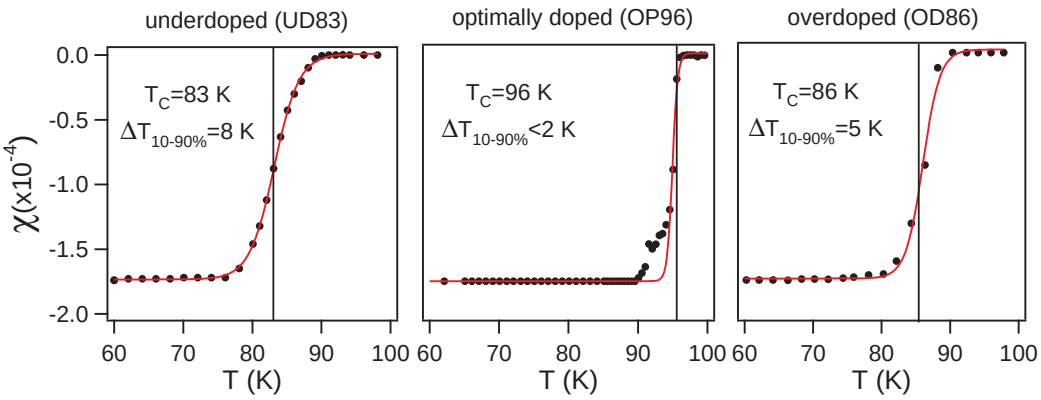

Figure 5.2: Magnetic susceptibility curves as a function of the temperature.

5.3 Sample preparation

Large single crystals of Y-substituted Bi2212 have been provided by the group of Prof. A. Damascelli in the University of British Columbia
These crystals were grown in an image furnace by the traveling-solvent floating-zone technique with a non-zero Y content in order to maximize T_c and with different annealing condition in order to obtain three different doped sampes [39]. The underdoped samples have been annealed at 550 °C for 12 days in a vacuum sealed glass ampoule with copper oxide inside. The overdoped samples were annealed under pure oxygen flow at 500 °C for 7 days. To avoid damage of the surfaces, the crystals have been embedded in BISCO powder during the annealing procedure. The samples have been homogenized by annealing in a sealed quartz ampoule, together with ceramic at the same oxygen content. The critical temperature of the sample are determined from the susceptibility curve obtained using a SQUID magnetometer. In fig.5.2 we report the magnetic susceptibility as a function of the temperature for three samples characterized by different doping regimes. For the optimally-doped sample (OP96) the critical temperature reported (T_c=96 K) is the onset-temperature of the superconducting phase transition, the transition being very narrow (ΔT_c <2 K). As a meaningful parameter for the under- (T_c=83 K, UD83) and over-doped (T_c=86 K, OD86) samples, which have transition widths of $\Delta T_{10-90\%}$ 8 K and $\Delta T_{10-90\%}$ 5 K, we reported the transition midpoint temperatures. The hole concentration p is obtained through the phenomenological formula [104]:

$$\frac{T_c}{T_{c,max}} = 1 - 82.6 \cdot (p - 0.16)^2 \tag{5.1}$$

where $T_{c,max}$ is the critical temperature of the optimally-doped sample.

5.4 Static optical measurements

In this section we report the equilibrium optical measurements performed the optimally-doped sample (OP96). All these measurements have been taken in the laboratories of the Quantum material group of the University of Geneve (head of the group,

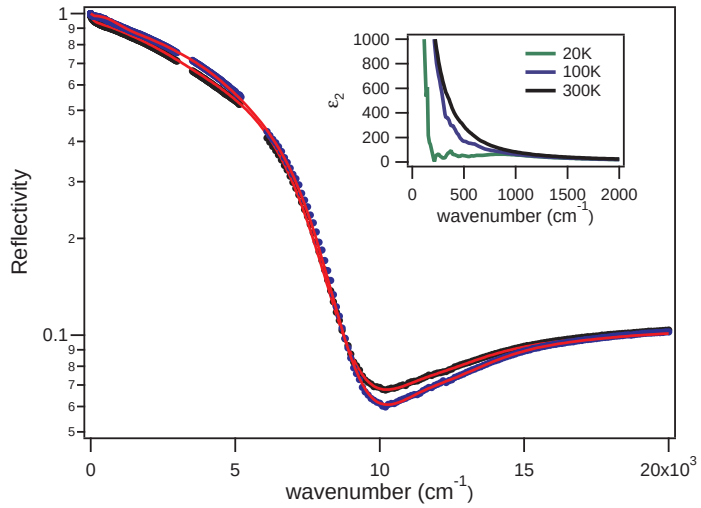

Figure 5.3: Reflectivity, measured on a broad energy range, is reported for OP96 at T=300 K (black line) and T=100 K (blu line). The red solid curve is the fit to the data. In the inset the imaginary part of the dielectric function ϵ_2, at low energies, is reported. In particular the opening of the superconductive gap is revealed as a suppression of spectral weight in ϵ_2.

Prof. D. Van der Marel). The optical response of the sample is measured using two different experimental techniques. In the low frequency region between 50 cm^{-1} and 6000 cm^{-1} (6-740 meV) in-plane normal incidence reflectivity measurement are performed by a Fourier transform spectrometer. In the frequency window that ranges from 1500 cm^{-1} and 36000 cm^{-1} (0.18-4.4 eV) ellipsometric measurements have been performed allowing to directly determine the dielectric function of the sample. In the far-infrared region the ab-plane dielectric function is extracted using the KK relations. This combination allows to determine with precision the dielectric function in the entire range of the reflectivity and ellipsometric measurements. The c-axis dielectric function previously determined from c-axis reflectivity measurements, is used to extract the true ab-plane dielectric function washing out all the out of plane cotributions due to the off-normal angle of incidence used in the ellipsometric measurements. All these measurements are carried out in ultra high vacuum condition.

5.4.1 Interband transitions and mid-infrared peaks

In the fig.5.3 we report the reflectivity measured on the sample OP96 in the normal and pseudogap phases respectively at 300 K and 100 K. The reflectivity measured in superconductive state at 20 K is not reported bacause it completely overlaps the 100 K measurement on the scale of the graph. In the fig.5.3 we report the real ϵ_1 and imaginary part ϵ_2 of the dielectric function at different temperatures. The intraband optical region under 1.25 eV (10000 cm^{-1}) is dominated by a broad Drude peak that will be discussed extensively in the next section.

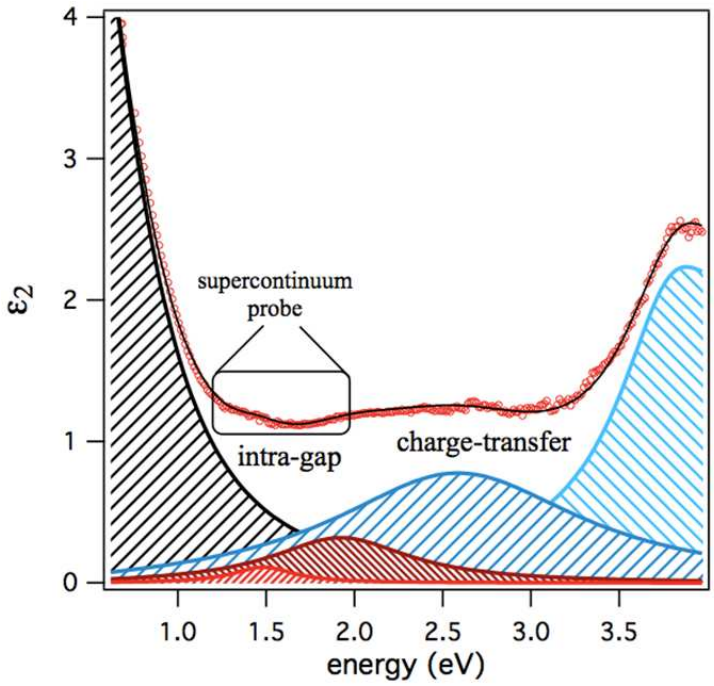

Figure 5.4: The high-energy region of the imaginary part of the in-plane dielectric function, measured at T=20 K for the OP96 sample is shown. The thin black line is the fit to the data described in the text. The values of the parameters resulting from the fit are reported in the table5.2. The contributions of the individual interband oscillators at $\omega_{0,i}$=1.46, 2, 2.72 and 3.85 eV are indicated as colour-patterned areas. The black inset indicates the spectral window covered by the supercontinuum light probe.

In the high energy region ($\hbar\omega > 1.25$ eV) the optical response is dominated by the interband optical transitions. The best fit to the data (solid line) is obtained modelling the equilibrium optical conductivity $\epsilon_{eq}(T,\omega)$ as:

$$\epsilon_{eq}(T,\omega) = \epsilon_D(T,\omega) + \sum_i \epsilon_{L,i}(T,\omega) \tag{5.2}$$

where the first term is the Drude peak of the conductivity and the second term is a sum of Lorentz oscillators.
We stress that the $\epsilon_{eq}(T,\omega)$ obtained by the fitting procedure reproduces both ϵ_1 and ϵ_2 in the whole experimental range. In the table (5.2) we report all the parameters obtained from the fit procedure on the OP96 sample at 300 K, 100 K, 20 K.
The optical properties are satisfactorily reproduced over the whole spectrum, considering, in addition to the extended Drude model, two mid-infrared (MIR) peaks in the intraband region (∼0.5, 0.8 eV), whose origin is still subject of debate. Many experimental groups suggest that these peaks are a remnant of some spectroscopic feature intrinsic to the undoped compounds [11]. A possible interpretation of this well-established structures is a transition from the occupied low-Hubbard band (LHB) of Cu to the Fermi energy in the O-2p band [74, 120].

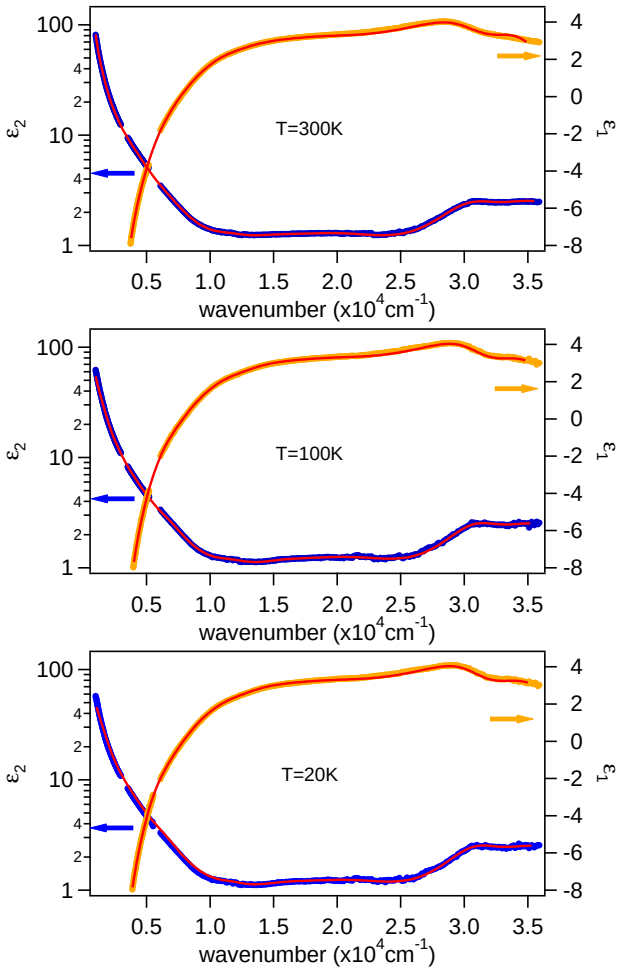

Figure 5.5: Real and imaginary part of the dielectric function are reported at T=300 K, T=100 K, T=20 K

The interband transitions in the near-IR/visible/UV spectral range are reproduced using six Lorentz oscillators at ∼1.45, 2, 2.7, 3.85, 4.36 and 5 eV. The identification of the interband transitions with specific electronic excitations is an open issue as well. Many efforts have been devoted to give a possible interpretation studying the temperature and doping behaviour of the optical conductivity. A common feature observed in all undoped compounds is a suppression of spectral weight below 2 eV due to the presence of a charge-transfer (CT) gap. Adopting the hole-picture, the charge-transfer process is explained in terms of a hole transfer from the upper Hubbard band with $d_{x^2-y^2}$ symmetry to the O $2p_{x,y}$ orbitals. Increasing the doping level of the sample, the energy region below the gap is partially filled by states at the expense of the spectral weight related to the CT excitations of the undoped compound. However the feature associated to the CT gap clearly persists in the finite doping region and it's found to be blue-shifted.
Dynamical mean field calculations of the electron density of states and optical conductivity in an hole-doped three-band Hubbard model [32], recently found that the

Fermi level moves into a broad (∼2 eV) and structured band of mixed Cu-O character, corresponding to the Zhang-Rice singlet states, in agreement with previous experimental results [16]. The empty upper Hubbard band (UHB), constituted by Cu-3d^{10} states, is shifted to higher energies with respect to the undoped compound, accounting for the blue-shift of the optical CT edge to 2.5-3 eV. The structures appearing in the optical conductivity at 1-2 eV, i.e. below the reminiscence of the CT gap, are related to transitions between mixed Cu-O singlet states with different symmetries.
Little *et al.* [75] give a different interpretation of the 1.5 eV oscillator in terms of a d-d transition, i.e., an electronic transition between Cu 3d states. However the rather small dependence with the temperature of the oscillator strength compared to the strong variation of the phonon-assisted d-d transition observed in other parent compounds [12] makes this hypothesis inconsistent.
The dielectric functions of the UD83 and OD86 samples have been extrapolated from the $\epsilon_{eq}(T,\omega)$ of the OP96, following the trend of the optical properties at different dopings, reported in Ref. [20]. In particular, for the UD83 sample, the main modifications to the dielectric function are: i) ϵ_∞=2.55; ii) the plasma frequencies of the Drude ω_p and MIR peaks (ω_0 and ω_1) are decreased by ∼3.7%; iii) the plasma frequencies ω_2 and ω_3 are decreased by ∼3.7%; iv) the plasma frequency ω_4 is decreased of ∼13%; v) the plasma frequency ω_5 is increased of ∼30%; vi) the plasma frequencies ω_6 and ω_7 are decreased by ∼4.8%. For the OD86 sample, the main modification to the dielectric function are: i)ϵ_∞=2.79; ii) the plasma frequencies of the Drude (ω_p) and MIR peaks (ω_0 and ω_1) are increased by ∼2.9%; iii) the plasma frequencies ω_2 and ω_3 are increased by ∼2.9%; iv) the plasma frequency ω_4 is increased by ∼14%; v) the plasma frequency ω_5 is decreased by ∼17%; vi) the plasma frequencies ω_6 and ω_7 are increased by ∼3.7%.

5.4.2 Strong-coupling analysis and far-infrared region

As pointed out in the previous section, the Drude peak in the intraband optical region has a width broader than in the case of a normal metal. The reason of this broadening is the coupling of the free carriers to a broad spectrum of bosons whose origin is still being discussed. We adopt the generalized Drude formalism, described in the section (3.2.1), to study the optical response of the medium in the far infrared region. The Drude component ϵ_D of the dielectric function in (5.4) is written in term of a complex optical self-energy Σ_{opt}. Employing the Allen approximation [4], Σ_{opt} is given by the sum of a contribution due the impurity scattering rate Γ_{imp} and a convolution integral between a kernel function $K(\omega,\Omega,T)$ and a general boson spectrum $\Pi(\Omega)$.
We follow the work by van Heumen *et al.* [127] and we use an histogram representation of $\Pi(\Omega)$ which does not depends on a microscopic model, since we are interested only in the relevant spectral features of the bosonic glue. This fit procedure has been previously applied to other HTSC such as $HgBa_2CuO_{4+\delta}$ and bismuth-based compounds with very good results. The authors also test the accuracy of the fitting procedure finding that an histogram formed by only 6 blocks are sufficient to reproduce the experimental data.
The bosonic function we used in our fitting procedure is a simplified one,constituted

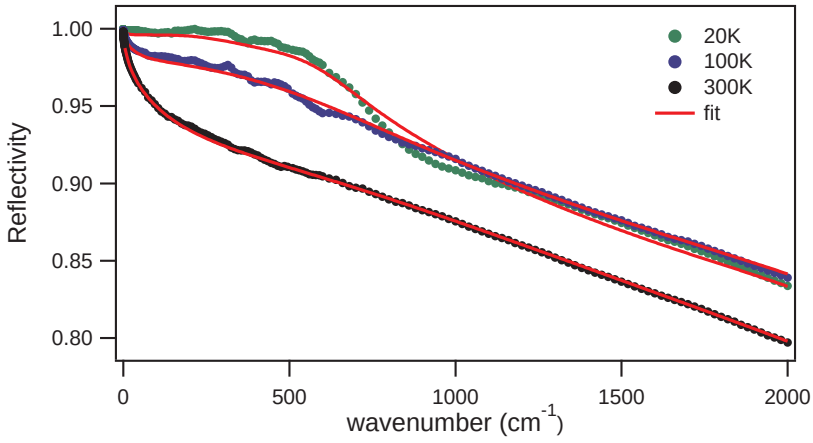

Figure 5.6: Reflectivity of OP96 at different temperature. The fit to the curve (red line) reproduces in a very satisfactory way the experimental data also at low energies.

by 4 blocks. On the other hand we added contribution to the dielectric function of two mid-infrared peaks at higher frequencies than the spectral broadening of $\Pi(\Omega)$. Another difference is that the blocks are mathematically written in term of sigmoid functions which are analytical approximation of the step function. As a consequence the total number of fit parameters necessary to describe the boson function are 14: a background term, a term connected to the steepness and other 3(x4) terms that describe the frequency, the width and the intensity of the blocks.
As we can see in the fig. 5.6 the resulting fit procedure reproduces in details the reflectivity of the OP96 sample, down to low photon frequencies, at different temperatures.

In the fig. 5.7 the boson spectra extracted from the fit at 300 K and 100 K and 20 K are reported. The distinctive feautures of the bosonic glue is the narrow peak at 50-70 meV which is present both in the normal and superconductive states and a broad spectrum extending up to 350 meV which will be discussed in the following. The intensity of the peak strongly varies with the temperature while its position does not significantly change: a slight blue-shift of few meV is observed with the increase of the temperature. The formalism used to fit the data is in principle valid in the normal state of an HTSC, assuming that the behaviour of the system is Fermi-liquid like. The opening of the pseudogap under T^* and the occurence of the superconductivity strongly change the density of states in the low-energy region and introduce additional effects that are not captured by this formalism. Moreover below T_c the far-infrared reflectivity is dominated by the opening of the superconducting gap and by the emergence of the condensate $\delta(0)$ function. For this reason, the extraction of the boson spectral function below T_c is a difficult task and, in particular, the results obtained for the underdoped sample, where the antiferromagnetic correlations play an increasing role, have to be handled with care.
The boson spectrum has been recently obtained [58] also from the equilibrium conductivity numerically inverting the optical scattering rate with the maximum entropy method. The resulting bosonic coupling function has the same wide spectral content

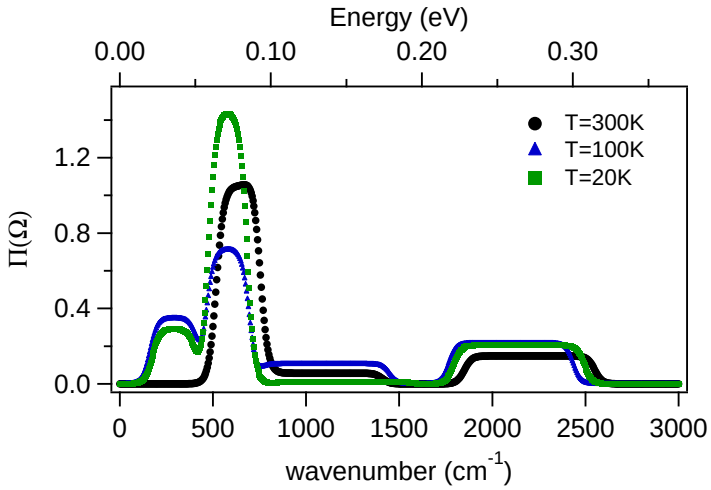

Figure 5.7: Electron-boson coupling functions extracted from the reflectivity fit. A physical feature found at all the temperatures, is a low-energy peak and a broad continuum extending up to $\sim$2500 cm^{-1}.

of $\Pi(\Omega)$ but the narrow peak, well evident below T_c is broadened and is frequency-shifted, merging into the high energy spectrum when the temperature increases.

The low energy peak is intimately related to the kink observed in ARPES spectra along the nodal direction and also to the sharp resonance observed at low temperature in magnetic neutron scattering measurements. Until now, detailed study do not to converge to a unique interpretation of this physical feautures and the interaction with optical phonons or magnetic resonance modes constitute possible explanations. Moreover it is very difficult to clearly disentangle these two different excitations because of the similar energy scales: the optical phonons have energies 40 meV and 70 meV while the energy of the magnetic resonance mode in the hole doped compounds is 40 meV. Another unsolved problem is to determine if this kink represents a real signature of superconductivity. Regarding this point a recent work of Hwang *et al.* [57] seems to exclude this possibility: studying the infrared optical properties of Bi-2212, they found that the narrow peak under 100 meV weakens at higher doping rate and completely disappears in the strongly overdoped side of the phase diagram (p=0.23) where the system is still a superconductor with a high critical temperature. The persistence of the peak well above T_c found in the resulting $\Pi(\Omega)$ seems to confirm that this spectral feature is not intrinsic to the superconductivity.

Together with the sharp feature, the boson coupling function displays a continuum background extending up to frequencies much higher than the maximum frequency of the lattice (Debye frequency ω_D) which is of the order of 100 meV. This part of the spectrum is sometimes called the Millis-Monien-Pines spectrum and it is common to all the HTSC independently of the techniques employed to extract $\Pi(\Omega)$. The electron-phonon coupling function $\alpha^2F(\Omega)$ of a BCS superconductor extracted from the tunneling experiments, has a width of the same size of the phononic density of states $F(\omega)$ and the peaks observed in $F(\omega)$ and $\alpha^2F(\Omega)$ coincide. In the specific case of an HTSC, the background can not be due to phonons, because of its large spectral content, and it has necessary an electronic origin: a coupling mediated by

Table 5.1: We report here the values of the electron-boson coupling constant λ obtained by integrating the glue function $\Pi(\Omega)$ at different temperatures. The corresponding T_c, calculated in the frame of the strong-coupling formalism, are also reported.

Temp (K)	λ	$\widetilde{\Omega}$ (cm^{-1})	T_c (K)
290	0.96	730	113.9
100	1.54	463	105.9
20	1.69	497	120.3

spin fluctuations or orbital currents has been proposed.

By a careful examination of the extracted $\Pi(\Omega)$ it is possible to get important informations on which are the parts of the spectrum that are responsible of the high T_c. Van Heumen *et al.* [127] have evaluated separatly the strength of the coupling above (λ_{bcg}) and below (λ_{peak}) 100 meV, employing the relation (2.5). The Mc Millan formula (2.6) relates the value of T_c with the strength of the coupling λ and for the Coulomb repulsion term μ=0 takes this simplified form:

$$T_c = 0.83\widetilde{\Omega} \exp\left(-\frac{1+\lambda}{\lambda}\right). \tag{5.3}$$

The values of λ_{peak} and λ_{bcg} are shown to change with the doping in particular for the overdoped sample the low frequency part of the boson function turns out to be too weak to explain the high T_c. These results suggest that also the high energy bosons has to be taken into account in the calculation of T_c and play a role in the mechanism of the superconductivity.

We repeated the same analysis for the OP96 sample and we obtained the values reported in table (5.1). The values of T_c obtained are higher but very close to the experimental values. The overestimation of the critical temperature is expected and it comes from the fact that the pairing between electrons in HTSC has a d-wave symmetry and it is active only in the antinodal direction while the electron-boson coupling constant λ is extracted from a momentum mediated $\Pi(\Omega)$.

We note that the λ is temperature dependent and increases about twice at 20K as compared to the normal state. This behaviour is connected to an increasing of the 50 meV-peak intensity and a raise of a spectral feauture in $\Pi(\Omega)$ below the peak as we can see in fig. 5.7. The high energy part of the spectrum seems to change less significantly than the peak. A possible explanation of the increasing of the electrons interaction with the bosons could be given in terms of a pseudogap opening.

The observed temperature variation of the spectrum doesn't imply the failure of the strong coupling formalism where the thermal excitations of the bosons and electrons are described by the kernel function $K\left(\frac{\omega}{2\pi T}, \frac{\Omega}{2\pi T}\right)$(see eq. 3.5). It is concerning this problem, it was shown that the $\Pi(\Omega)$ function extracted from the T=290 K data reproduces satisfactorily the experimental spectra in the pseudogap state and under T_c. For this reason we conclude that the temperature dependence of the optical spectra mainly originates from the Bose-Eistein and Fermi-Dirac factors contained

in $K\left(\frac{\omega}{2\pi T}, \frac{\Omega}{2\pi T}\right)$ and only small differencies between theoretical and experimetal curves have to be ascribed to an effective temperature dependence of $\Pi(\Omega)$.

5.4.3 The optical self-energy

The optical self-energy Σ_{opt} is a complex function which it is introduced in the formalism of the generalized Drude model to describe the strong interaction between the free electron gas and a general spectrum of bosons. The real and imaginary part of Σ_{opt} describe respectively the frequency dependent scattering rate $1/\tau(\omega)$ and the mass enhancement of the charged carriers $m^*(\omega)/m$ which is related to the coupling constant λ. Since the optical response is causal the these two quantity are related by the Kramers-Kronig relations.
We used the $\Pi(\Omega)$ obtained by the fit to compute $1/\tau(\omega)$ and $m^*(\omega)/m$ at different temperatures as shown in fig. 5.8. The inverse of the scattering time decreases with the temperature at all the range of frequencies and has the form $a + b\omega$ above 1000 cm^{-1}: the slope b is proportional to the the temperature as expected for the marginal liquid behavior of the carriers in HTSC while the intercept could be interpreted as the signature of the non-Fermi liquid behavior of the normal state. When the temperature is below T_c, $1/\tau(\omega)$ is strongly suppressed as a consequence of the opening of the superconductive gap Δ. The behavior of $1/\tau(\omega)$ is very similar to that extracted from ARPES measurement along the nodal direction; along the antinodal direction instead the scattering rate of the electrons seems to feel the effects of the superconductivity.
From the frequency dependence of $1/\tau(\omega)$ it is possible to roughly estimate the superconductive gap. In the case of a BCS superconductor under T_c the absorption drops at the frequency $2\Delta + \Omega_{ph}$ where Ω_{ph} is the phonon resonance energy since the coupling is phonon-mediated. Analogously, in HTSC the inverse of the scattering rate onset is given by $2\Delta + \Omega_{bos}$ where Ω_{bos} is the energy of bosonic mode observed in the bosonic coupling function below 100 meV. We choose as the onset the frequency at which $\frac{1}{\tau(\omega)}$ ceases to be linear: 1200±50 cm^{-1}. Since the frequency position Ω_{bos} of the low-energy peak in $\widetilde{\Pi}(\Omega)$ is 585±50 cm^{-1} we find that Δ=307±100 cm^{-1} (i.e. 38±12 meV). This value is in agreement with the experimental value of Δ (40±5 meV) obtained with ARPES meausurements on the same Y-doped sample [115].
The narrowing of the optical conductivity at low frequencies causes both the drop of $1/\tau(\omega)$ and the increasing of m^* as we can see in fig. 5.8. This is in agreement with the definition of m^* as the probability of the charged carriers to be scattered. At higher frequencies the ratio between the effective mass and the bare mass approaches the unity. Decreasing the temperature, m^* reaches higher values and below T_c displays a hump at $\omega \sim 600\ cm^{-1}$ and saturates to a finite value.
Another important physical quantity that can be extracted in the frame of the extended Drude model is the strength of the electron-boson coupling λ from the relation:

$$\lim_{\omega \to 0} \frac{m^*(\omega)}{m} = 1 + \lambda \tag{5.4}$$

For T=20 K we obtain the value λ=1.7 which is in agreement with the value 1.69 obtained from the integration of $\Pi_{T=20K}(\Omega)$ reported in table (5.1).
It's necessary to specify that sometimes the interpretation of the Σ_{opt} in term of

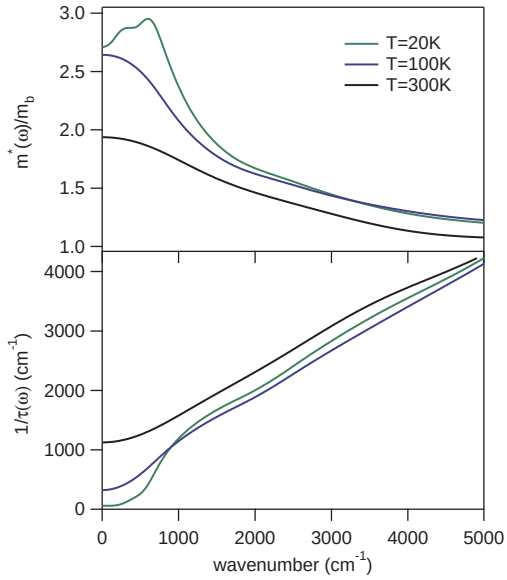

Figure 5.8: The frequency dependent effective mass (top) and the scattering time (bottom) are calculated at different temperature in the frame of the extended Drude model using the parameter obtained by the reflectivity fit.

scattering rate and effective mass enhancement has to be tackled with care. For example the result that $1/\tau(\omega)$ goes to zero for $\omega \to 0$ in the superconductive state cannot be interpreted as an infinite quasiparticles lifetime but it is an effect due to the redistribution of the density of states under T_c [11].

5.4.4 Marginal Fermi liquid

In the section (5.4.2) we describe the optical properties of an HTSC using a strong coupling formalism and we chose a model-independent histogram rappresentation of the electron-boson coupling function. In particular we represent the glue function adopting the Marginal Fermi Liquid (MFL) phenomenology and we compare the result to the ones obtained in the last section.
The Marginal Fermi liquid model is a phenomenological model that was introduced by Varma and co-workers [130] to explain some anomalous physical properties in the normal state of the cuprate superconductors, i.e. the linear temperature dependence of the in-plane resistivity and the unexpected behavior of the nuclear relaxation rate in NMR measurements. The main hypothesis behind this theory consists in the assumption that the glue function is made of charge or spin excitations which, in the low frequency region, scale as ω/T.
The simplified version of the bosonic spectrum is given by $\Pi(\Omega) = \min\left(\frac{\omega}{T}, cost\right)$ ($\Pi(\Omega)$ goes like ω/T at low energies and it is constant above this region). A cutoff Ω_c in the glue function is introduced to make convergent the electron self-energy.
Starting from the original work by Varma [130] we write $\Pi(\Omega)$ in an analitical

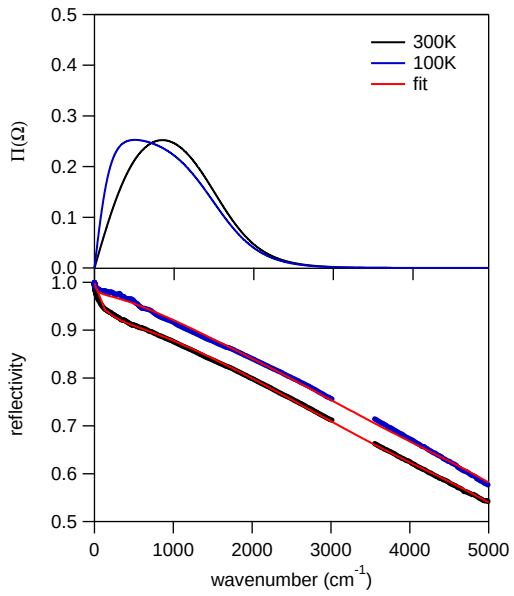

Figure 5.9: (Top) Electron-boson coupling function extracted from the fit of the reflectivity using the MFL model. (Bottom) Static reflectivity (OP96) at low energy and fit for MFL model

form:

$$\widetilde{\Pi}_{MFL}(\Omega) = \Lambda \tanh\left(\frac{\Omega}{2T}\right) f(\Omega, \Omega_c, \Delta) \tag{5.5}$$

where $f(\Omega, \Omega_c, \Delta)$ is the high energy cutoff function which has the following form:

$$f(\Omega, \Omega_c, \Delta) = \frac{1}{1 + \exp\left(\frac{\Omega - \Omega_c}{\Delta}\right)}. \tag{5.6}$$

Λ is the coupling constant of the entire boson spectrum while Δ is a parameter connected to its spectral width [124].
We replace $\Pi_{MFL}(\Omega)$ into eq. (3.9) and we fit the reflectivity. The results of the fit are displayed in fig. 5.9 together with the $\Pi_{MFL}(\Omega)$ coupling functions in normal and pseudogap state. The λ obtained from the integration of $\Pi_{MFL}(\Omega)$ increases at low temperatures changing from λ=1.06 at T=290 K to λ=1.46 at T=100 K . This effect can be understood in terms of a general redshift of the glue function and an increase of the spectral weight in the low energy region observed also in $\Pi(\Omega)$. It's very interesting to note that, in order to obtain good fit, it is necessary to change only the temperature and the parameter Λ, while the ω_c and Δ remain fixed. This result seems to confirm the ω/T behavior of the bosonic coupling function distinctive of the MFL model. For the sake of completeness, an analogous ω/T scaling behavior was recently observed in the optical conductivity: $\sigma(\omega, T) = T^{\mu} h\left(\frac{\omega}{T}\right)$ where the exponent μ assumes different values depending on the ratio $\frac{\omega}{T}$.
The MFL model can be extendend in the superconductive state, modifying $\Pi_{MFL}(\Omega)$ and taking into account of the opening of the gap. In this case we talk of gapped MFL [96].

5.5 Conclusion

In this chapter we report the optical measurements carried on the Y-doped Bi2212 in equilibrium condition. The dielectric function is reproduced by a set of interband optical oscillators in the visible region. The oscillators placed at 1.5 and 2 eV are related to transitions between mixed Cu-O singlet states with different symmetries while, the interband oscillators in the ultraviolet region are a reminiscence of the charge transfer gap. Two mid-infrared peaks, whose origin is still subject of debate, are added to fit the dielectric function in the intraband region ($\sim$0.5 and $\sim$0.8 eV). The extended Drude model is employed to describe the low-energy optical properties of the system and allow to extract the electron-boson coupling function which is characterized by a narrow peak at $\sim$70 meV and a broad continuum extending up to $\sim$300 meV. The high-energy part of the glue function is considered to be related to the bosonic modes of electronic origin, like spin fluctuations, because it extends well above the upper limit of the lattice excitation in HTSC i.e.100 meV. The low-energy peak was already observed by different experimental measurements but the nature of the bosons which give rise to this spectral feauture is still debated.

Table 5.2: Parameters used in the fit to $\sigma_{eq}(T,\omega)$ of the OP96 sample. All the values are expressed in inverse centimeter units (cm^{-1}).

	parameters	T=20K	T=100K	T=300K
Extendend Drude	ϵ_{inf}	2.67	2.67	2.62
	ω_p	17418	17392	16901
	Γ_{imp}	53	155	625
	T	20	100	290
Mid-infrared peak	ω_0	4234	4929	4264
	ω_{p0}^2	10454991	13871222	22041800
	γ_0	3535	4706	4069
	ω_1	6490	6959	6789
	ω_{p1}^2	11001998	6489852	8142014
	γ_1	3519	2949	3925
Interband transitions	ω_2	11800	11800	11650
	ω_{p2}^2	5560610	7460610	5307060
	γ_2	3644	3944	3500
	ω_3	16163	16163	15409
	ω_{p3}^2	40768500	41268500	45542000
	γ_3	8304	8304	8905
	ω_4	21947	21947	21300
	ω_{p4}^2	225776000	230776025	223159025
	γ_4	13998	13898	13898
	ω_5	31057	31057	30756
	ω_{p5}^2	288626121	288626121	320536896
	γ_5	6191	6191	6908
	ω_6	35146	35146	34946
	ω_{p6}^2	217474009	217474009	214474009
	γ_6	6396	6396	6396
	ω_7	40421	40421	40421
	ω_{p7}^2	750212100	750212100	756371984
	γ_7	7518	7518	7518

Chapter 6

One-color time-resolved optical measurements

6.1 Introduction

In this chapter we report time-resolved reflectivity measurements performed on the samples $Bi_2Sr_2Ca_{0.92}Y_{0.08}Cu_2O_{8+\delta}$ at three different doping level (UD83, OP96, OD86) in a temperature range between 20 K and 300 K. Both the probe and pump wavelengths are set at 800 nm (one-color configuration) and they are provided by the optical oscillator described in chapter (4.2). The transient response of each sample is fitted by a sum of exponential decay functions. A detailed study of the temperature dependence of the decay times is done. The peculiar sensitivity of this technique to the phase of the system enables to obtain important informations about the phase diagram of an HTSC and in particular on how the psedogap crossover temperature T^* evolves with the doping level.

6.2 Experimental data

Ultrafast time-resolved reflectivity is an experimental technique largely employed in the field of high temperature superconductivity because, in contrast to the standard equilibrium spectroscopies, allows to study directly in time domain the quasiparticles recombination dynamics. Besides the high temporal resolution, another advantage of this techniques is the sensitivity to the phase of the system. The transient optical response of an HTSC depends on the temperature and also on the doping rate as we will see in this chapter. In particular the different time scales of the quasiparticles response enable to get more information on the interplay between different phases of the system. With regard to this point, the relationship between the superconductive and the pseudogap state is not well understood and is subject of a debate to clarify whether the pseudogap is a precursor or it is in competition with the superconductive phase. Strictly connected to this problem there is the issue of the determination of the phase diagram of an HTSC and in particular of how the pseudogap line merges into the superconductive dome.

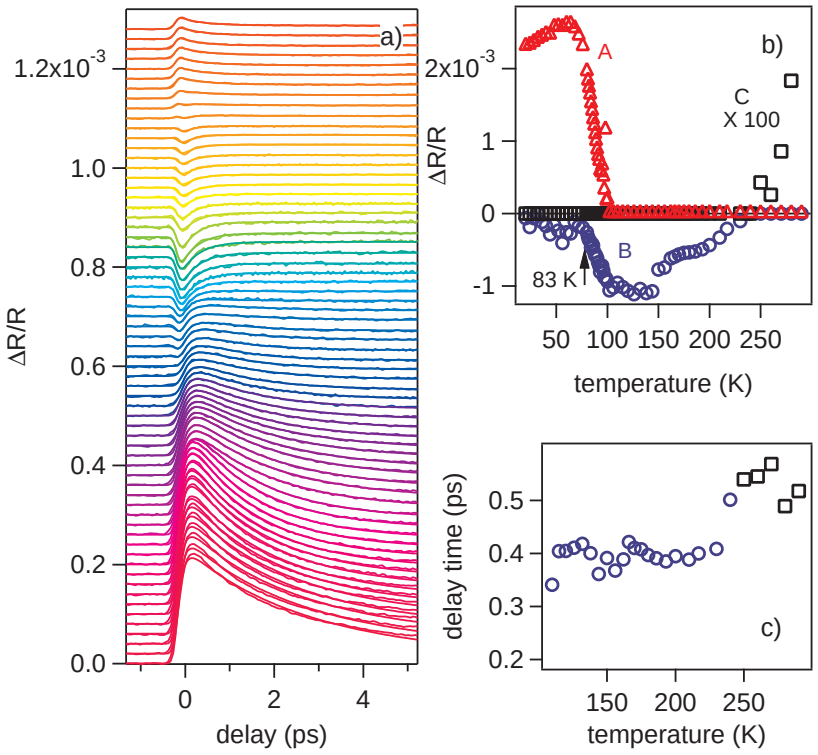

Figure 6.1: (a) Time-resolved reflectivity traces on underdoped Y-doped Bi2212 at different temperatures, are reported. Both the pump and probe wavelenght are set to 800 nm. An offset proportional to the sample temperature has been added to the traces. The solid lines superimposed to the data are the fit with the function 6.1. (b) The amplitude of the exponential decays is reported as a function of the temperature. The values of the coefficient C, related to the normal state component have been multiplied by 100, for display purposes. (c) The fast decay times τ_B and τ_C, obtained by the fitting procedure, are reported as a function of the temperature.

In the last decade this problem has been approached by many authors [34, 76] employing one-color pump-probe reflectivity techniques.
A typical time-resolved reflectivity signal in a HTSC is characterized by a fast transient component with a finite rise time of the order of few hundreds of femtoseconds and a temperature dependent decay time which changes abruptly under T_c and is related to the energy exchange between electrons and phonons. The signal related to the thermalization of electrons among themselves via intraband scattering processes has a relaxation time τ_{e-e} too fast ($\tau_{e-e} = \hbar E_F / 2\pi E^2$ where E is the energy measured with respect the Fermi level E_F) and it's covered by the temporal width of the pulse. Beside these components, there's another slow dynamics related to the phonon thermalization which is well reproduced by an exponential decay with a slower relaxation time of about 100 ps. At the moment, we do not consider, in the fitting procedure, the slow component and we focus on the fast one trying to study

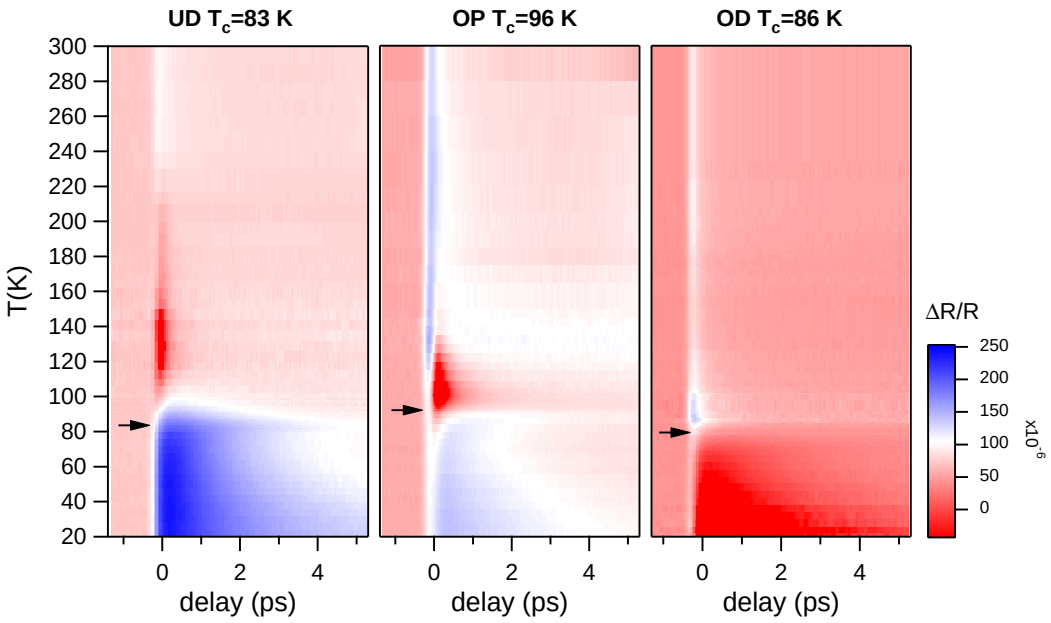

Figure 6.2: Temperature dependence of the time-resolved reflectivity measurements at λ_{probe}=800nm. The black arrows indicate the critical temperature.

its change with the temperature.

In fig. 6.1a we report time-resolved reflectivity scans ($\Delta R/R(t)$) on the underdoped (UD83), where the pseudogap region is more extended. The positive and negative fast components of the measured signal have been extracted by fitting to the data a triple exponential decay, convoluted with a Gaussian curve, taking into the temporal profile of the pump and probe pulses (full-width-halfmaximum= 120 fs). The exponential decay function is given by:

$$f(t) = A\exp(-t/\tau_A) + B\exp(-t/\tau_B) + C\exp(-t/\tau_C) \tag{6.1}$$

where τ_A is a slow decay time (τ_A >1 ps) and τ_B and τ_C are fast decay times (τ_B,τ_C <1 ps). The fitting procedure evidences a large and positive A component, that disappears approaching T_c from below and, for this reason, is attributed to the superconducting (SC) phase. Around T_c a negative component starts to appear overlappig with the slow and positive one. This component increases with the temperature reaching the maximum at about 130K and then starts to decreses disappearing at a temperature T^* of about 220K. Also the relaxation time changes above T_c and drops to about 400 fs according to the fact that the system is no longer a superconductor and a bottleneck in the quasiparticles recombination process is absent. The value of the crossover temperature T^* and the sharp change sign of $\Delta R/R$ leads us to interpret this feauture as the fingerprint of the pseudogap phase. A similar value of T^* was obtained by Liu *et al.* [76] in the same measurements carried on a sample of underdoped Bi2212 and it's consistent with the results obtained by other experimental techniques reported in [55].

Above T^* the B component drops and a small positive component, related to the normal phase, appears.

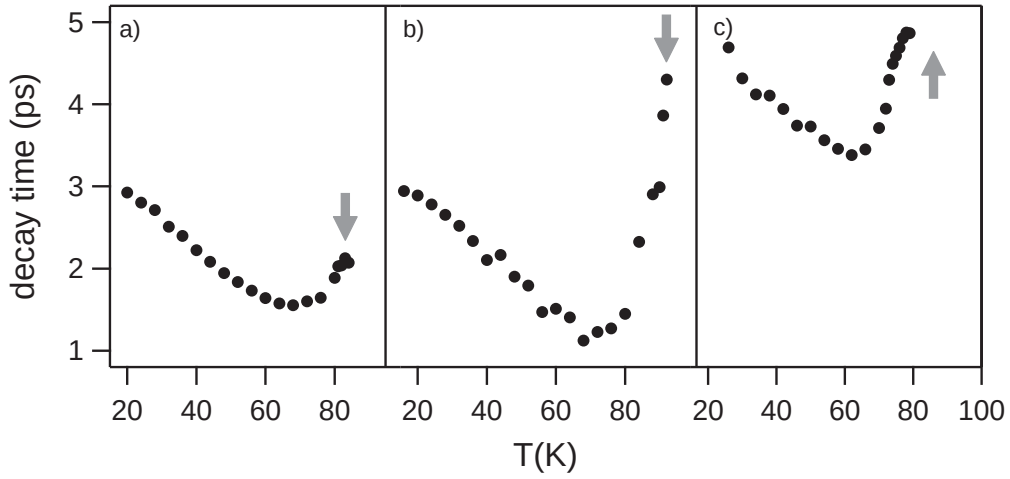

Figure 6.3: The decay times, obtained by fitting the exponential decay of the reflectivity, are reported as a function of the temperature. The black arrow indicate the critical temperature.

In fig. 6.1b the temperature dependence of the three components amplitude is shown: to help the reader the values of the C coefficients have been multiplied by a factor 100. In fig. 6.1c we report the values, obtained from the fitting procedure, of the decay times τ_B and τ_C of the non-equilibrium populations photoinjected in the N and PG phases. The decay time is fast in both the N and PG phases ranging from $\sim$500 fs at T=300 K to $\sim$ 400 fs at T=100 K. The decay time values extracted from the fitting procedure as T_c is approached (90K$\leq$T$\leq$100K) are not reported, since the coexistence of the A and B components did not allow to obtain reliable values of τ_B.
The values of τ_A obtained from the fit are reported in fig. 6.3 at different doping regime and will be discussed later on.
Fig. 6.2 shows the 2D plot of the transient reflectivity at different temperature carried on the three samples. As we can see, the sign of $\Delta R/R$ doesn't change qualitatively from under to optimally doped but the value of T^* extrapolated linearly decreases with the doping to the value T^* $\sim$140K. The decay dynamics becomes slightly faster in OP96 below T^* as compared to what observed in the UD sample. In the overdoped sample the pseudogap component is not detected because the T^* line has merged into the superconducting dome at lower doping level. Another difference encountered in the OD region, is the change of sign (from positive to negative) of the relative change of reflectivity in the superconductive state. The sign flip of the transient component was already reported by Gedik *et al.* [48] in Bi2212 and triggered an animated debate.

6.3 Conclusion

The measurements that we report in this chapter show that the signal variation strongly depends on the phase of the system, making this technique a very useful and promising tool to study the phase diagram of an HTSC. The $\Delta R/R(t)$ is positive and fast in the normal state with a decay time of the order of $\sim$ 400 fs, while it changes sign in the pseudogap phase. The temperature at which the negative component starts to appear, is ascribed to the onset of the pseudogap phase and it turns out to be $\sim$220 K for the UD83 and $\sim$130 K for the OP96 sample. In the OD86 sample the pseudogap component is not detected meaning that the T^* line merges with the superconducting critical temperature. The amplitude of $\Delta R/R(t)$ increase of one order of magnitude in the superconductive state while the corresponding decay time slows down because of the opening of a gap and it turns to be of the order of few ps.

Chapter 7

Normal state

7.1 Introduction

In this chapter we report time and frequency resolved reflectivity measurements on $Bi_2Sr_2Ca_{0.92}Y_{0.08}Cu_2O_{8+\delta}$ at different doping levels in normal state. All the measurements shown here are performed at T=290 K. We exploy the strong coupling formalism used to fit the equilibrium optical spectra in chapter 5 and we develop a differential model to interpolate the pump-induced modification of the reflectivity over the entire energy range set by the spectral content of the probe. We will show later how the possibility to disentangle the electronic and bosonic contribution to the transient signal, gives us the chance to determinate which is the part of the glue function $\Pi(\Omega)$ that is ascribed to the phonons and to the electronic boson modes. The coupling constant λ and the contribution to the superconductive critical temperature are obtained in both the cases by integrating $\Pi(\Omega)$ and using the McMillan formula [86]. Our conclusion is that neither the electronic modes nor the lattice alone are not able to account for the high T_c observed. This suggests that the superconductivity in cuprates can be explained by an interplay between these two pairing mechanisms [60, 61, 88].

7.2 Preamble

One color time-resolved reflectivity measurements have the great advantage to temporally resolve the dynamics of the electronic excitations out of equilibrium and to provide important informations on the mechanisms of the energy exchange with the other degrees of freedom of the system. In this configuration, a pump pulse of energy $\hbar\omega$, excites above E_F, all the electrons that occupy the electronic bands in a spectral region that extends $\hbar\omega$ below E_F. The monochromatic probe pulse follows the carriers relaxation dynamics through the Fermi level but the resulting transient signal $\Delta R/R$ is limited only to the probe photon energy. The lack of spectral resolution makes difficult to assess which is the physical origin of the reflectivity variation particularly in strongly correlated systems like cuprates where the strong electronic correlations plays a fundamental role.

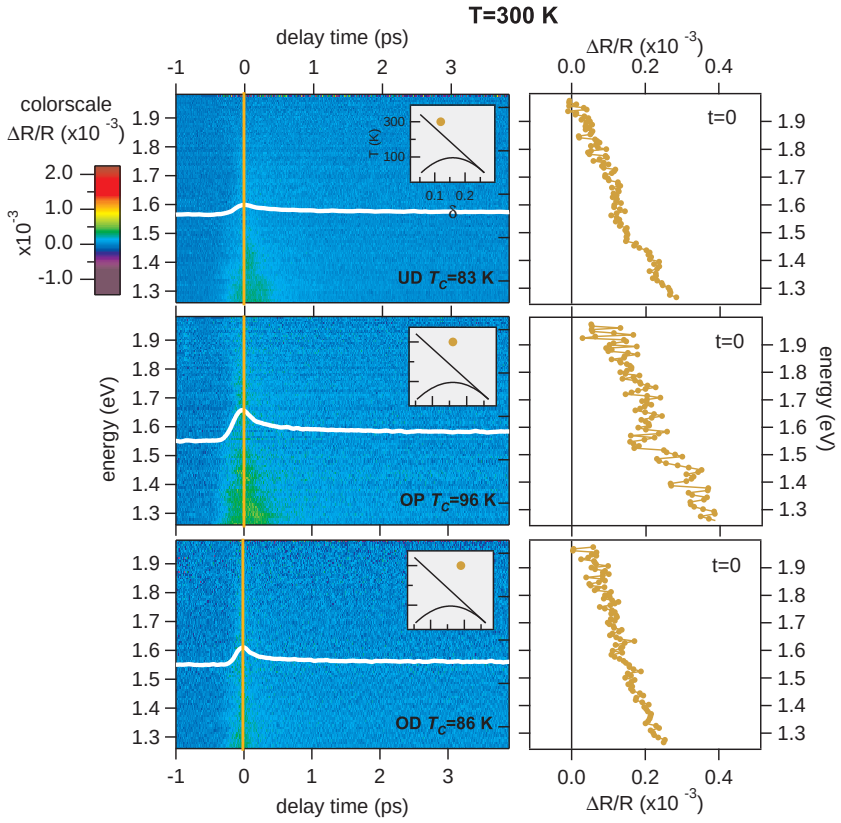

Figure 7.1: Energy and time-resolved reflectivity on $Bi_2Sr_2Ca_{0.92}Y_{0.08}Cu_2O_{8+\delta}$. The 2D scan are reported for different doping range at T=290K. The colour scale of the reflectivity variation amplitude is reported on the top left of the figure. The insets display the position of each scan in the T-δ phase diagram. The white lines are the $\Delta R/R(t)$ traces obtained at λ_{probe}=800nm. The yellow line represents the cut at the delay time τ=0 ps. The energy resolved spectra $\Delta R/R(\omega, \tau = 0)$ are reported next to the respective 2D plot.

In simple systems, like metals, it's well established that the measured $\Delta R/R$ can be explained as a thermal effect which modifies the electronic distribution function [54]. In cuprates the situation is more complicated and many other effects could overlap and contribute to $\Delta R/R$, like a rearrangement of the electronic bands due to the optical spectral weight shift [48].
In this case the temporal resolution is not sufficient to disentangle the several contributions and it is necessary to study the transient dynamic behaviour of the dielectric function of the system over a broad spectral range of energies. A possible way to satisfy this condition, conserving the high temporal resolution, is to use the supercontinuum light or a frequency tunable femtosecond light pulses as a probe.
In the previous chapter we have seen how the supercontinuum light is chirped due to the self-phase modulation and group velocity dispersion occurring in the photonic crystal fiber. The determination of the spectral and temporal structure of the broadband pulse allows us to determine the real response of the system.

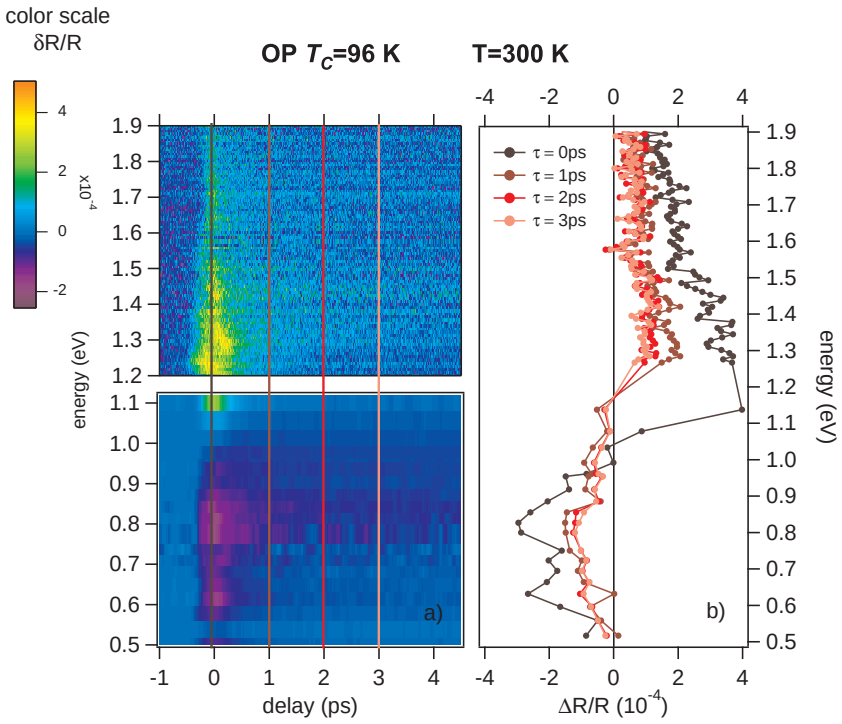

Figure 7.2: (a) Pump-supercontinuum probe reflectivity measurements (top) jointed with pump-OPA probe reflectivity measurements (bottom) carried on OP96 at T=300K. The total probe energy range is 0.5-2 eV. The pump fluence I_{fl}=10 $\mu J/cm^2$ per pulse. The straight line represents the temporal cut of the 2D spectra. (b) Energy resolved spectra at different delay times.

Since the study of the temporal behaviour of the dielectric function of an HTSC is a difficult task and many effects connected to the occurence of the superconductivity could further complicate the analysis, we tackle the problem starting from the normal state of HTSC, where the system has a metallic-like behaviour.

7.3 Experimental data

In fig. 7.1 we report the time and frequency resolved reflectivity ($\Delta R/R(\omega, t)$) carried on the underdoped (UD83), the optimally doped (OP96) and the overdoped (OD86) samples in normal state at room temperature (T=290K). The frequency window used to explore the dynamics is limited by the sensitivity of the photodiode array (PDA) and ranges from 1.25 eV to 2 eV. The maximum temporal delay between pump and probe is 4.5 ps. As we can notice from the color scale, the fractional change of reflectivity is positive and fast, and it is similar at different doping levels as already observed in the one color time-resolved measurements (Fig. 6.2). For each 2D plot, the time traces are reported: the temporal behaviour at each frequency displays a fast transient component and a slow decay which could be interpreted respectively as the electron-phonon relaxation and the phonon thermalization.

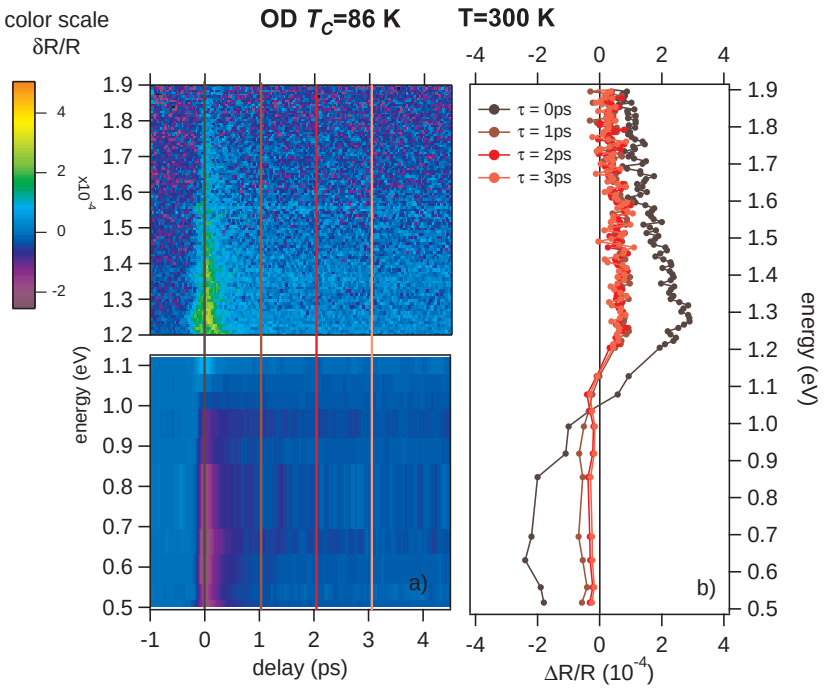

Figure 7.3: (a) Pump-supercontinuum probe reflectivity measurements (top) jointed with pump-OPA probe reflectivity measurements (bottom) carried on OD86 at T=300K. I_{fl}=10 $\mu J/cm^2$ per pulse. (b) Energy resolved spectra at different delay times.

The energy-resolved spectra, obtained at different delay times monotonically increase with the probe energy and seems to vanish in the ultraviolet region without showing any particular structure.
In fig. 7.2 and 7.3 we report the data obtained from the supercontinuum probe technique extended in the infrared region down to 0.5 eV employing the signal and idler pulses provided by an OPA system. We report here the spectra for OP96 and OD86 samples. The total energy extension of the probe now ranges from 0.5 eV to 2 eV. The pump fluence and in general the experimental conditions are the same used in supercontinuum probe measurements (laser fluence=10 $\mu J/cm^2$). Looking closely at the OPA time traces of OD86 sample (fig. 7.4a-b), we can appreciate how the transient response of the system is complex in the infrared region. Near the visible region, above ω_{probe}=1.1 eV, $\Delta R/R(t)$ is characterized by a sum of a positive fast and slow components with a decay time of τ_1=400 fs and τ_2=3 ps respectively. Shifting the probe energy towards the infrared, both the dynamics change sign. The reversing of $\Delta R/R(t)$ makes the transient signal more difficult to analyze near the crossing point. In the spectral region far from the crossing point we find out a similar two component temporal dynamics reversed in sign.
The energy resolved spectra extended in the infrared region are shown in fig. 7.2b and 7.3b. Both the OP and OD traces display a positive maximum at about 1.3 eV and monotonically decrease as the photon energy increase. In the OPA probe region, $\Delta R/R(t)$ decreases, changing sign at about 1.1 eV, and it keeps constant

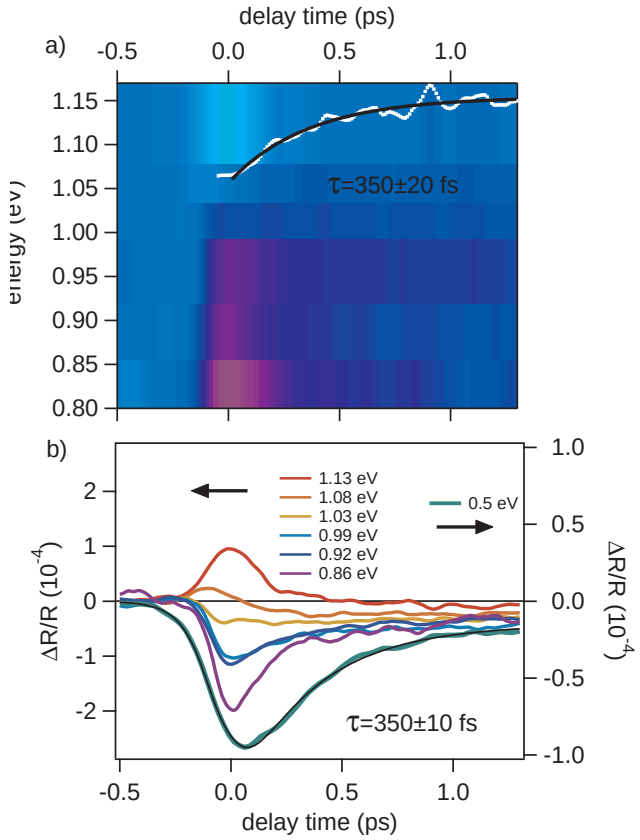

Figure 7.4: (a) Energy and time-resolved reflectivity on OD86 near the crossing point. The white line represents the temporal dynamics of the crossing point. The time evolution of this trace is fitted (black solid line) using a model with two component decays. The fast dynamics as a decay time τ of 350±20 fs. (b) $\Delta R/R(t)$ traces at different at different probe wavelength. The fast component of the trace at 0.5 eV has the same decay time that the crossing point

at about 2×10^{-4}. It is interesting to note that an additional dynamics is clearly visible by examining the 2D plots in the frequency domain at different delay times i.e. a blue shift dynamics of the crossing point, reported in fig.7.4b. The decay time of the fast component of this dynamics, reported in the inset of the figure, turns to be ∼350±20 fs.

7.4 Three-temperature model

Since the model we adopt to study the temporal behavior of the dielectric function depends on both the electronic and bosonic temperature, it is necessary to know the temporal profile of T_e and T_b after the absorption of the pump pulse. The three temperature model (TTM), described in section (3.3.3), it is a generalization of Allen model [5] to the case of the cuprates, where the electron population is strongly coupled with a subset of phonons with a short decay time and then thermalizes on

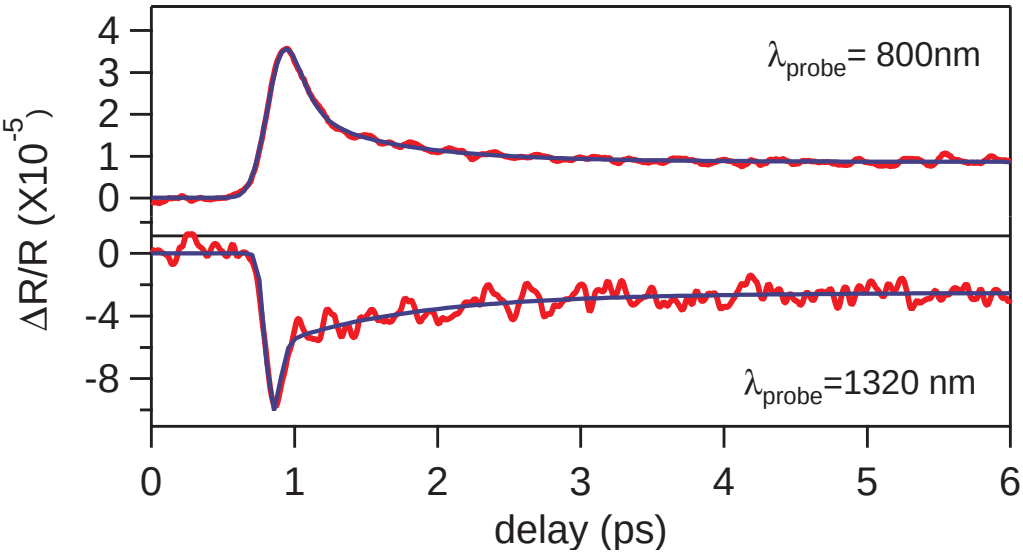

Figure 7.5: $\frac{\Delta R}{R}(t)$ traces at λ_{probe}=800nm and λ_{probe}=1320nm (OP96). I_{fl}=10 $\mu J/cm^2$. The fitting result is obtained by integrating numerically the solutions of the three temperature model. The result of the fit are reported in table 7.1

a longer time scale with the rest of the phonons.

This model [101] was introduced to fit the temporal behaviour of T_e directly obtained from the electron distribution function extracted from time-resolved photoemission spectra at different delays.

In fig. 7.5 we report the fit of the TTM to $\Delta R/R(t)$ at different probe energies. The coupling constant between electrons and strongly coupled phonons λ resulting from the fit of T_e, depends on the frequency of the phononic modes Ω_0 and varies from a maximum of ∼0.21 to a minimum of ∼0.08, in correspondence to the choice Ω_0=40 meV and Ω_0=70 meV. Since the electron-boson coupling function $\Pi(\Omega)$ extracted from the static optical reflectivity displays a low-energy narrow peak near 70 meV (69±4 meV), we assume λ as a fixed parameter and we set its value to λ=0.08 in the fitting procedure.

We chose to fit time-traces at a probe energy far from the crossing point where there

Table 7.1: Parameters obtained from the 3TM fit.

Ω_0 (meV)	λ	f	τ_β (ps)	T (K)	Fluence ($\frac{\mu J}{cm^2}$)
69±4	0.08±0.02	0.06±0.03	0.55±0.2	290	10

is no influence of the crossing point dynamics. In fig. 7.5 we report the $\Delta R/R(\omega_0, t)$ taken at ω_0=800 nm and ω_0=1320 nm. The fit (blue line) is obtained by integrating numerically the rate equations 7.15 and it satisfactorily reproduces the data assuming that the fractional variation of reflectivity is proportional to the electronic and

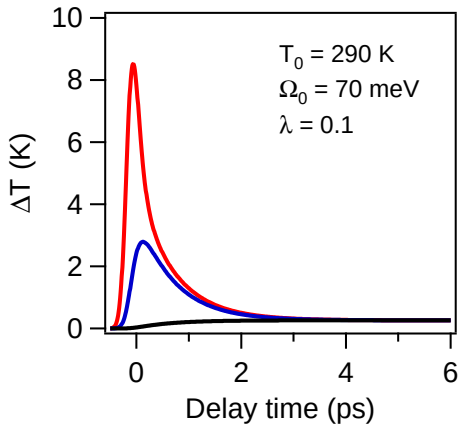

Figure 7.6: Simulation of the temporal behaviour of T_e,T_b and T_l. The parameter of the simulation are obtained by the fit of $\Delta R/R(t)$.

the cold phonon modes temperature, as in metals: $\Delta R = a\Delta T_e + b\Delta T_l$.
In order to make the model more realistic, we use in the rate equations the experimentally measured values of the electronic specific heat coefficient ($\gamma_{el} = C_{el}/T$) and of the lattice contribution to the specific heat of Y-doped Bi2212 [77]. The fitting parameters of the model are reported in table 7.1. Another interesting information comes from the fraction of hot phonons f: the results of the fit suggests that only a small fraction of all the phonon modes is strongly coupled with the electronic carriers. This result is in accord with the time-resolved photoemission studies and it was explained in term of the strong anisotropy of the phononic modes in HTSC [101].
The temporal profile of T_e, T_p and T_l obtained from the fit parameter is sketched in fig. 7.6.

7.5 Phenomenological differential approach

The modification of the reflectivity experimentaly observed on an ultrafast time scale is the effect of the pump-induced variation of the physical parameter that describe the equilibrium dielectric function of the system. In our case, the parameters that are perturbed by the light pulse and contribute to $\Delta R/R(\omega, t)$ in the probe pulse spectral range are (see table 5.2):

- the Drude plasma frequency ω_p
- the width Γ of the Drude peak
- the optical oscillators in the mid-infrared and the visible region

Both ω_p and Γ depends on the temperature. When the sample is heated by the pump pulse, we expect a variation of the these two term. It is indeed demonstrated that if the effective single band Hamiltonian, describing the motion of the Drude carriers, is simplified by a near-neighbour hopping approximation, ω_p is related to the kinetic energy.

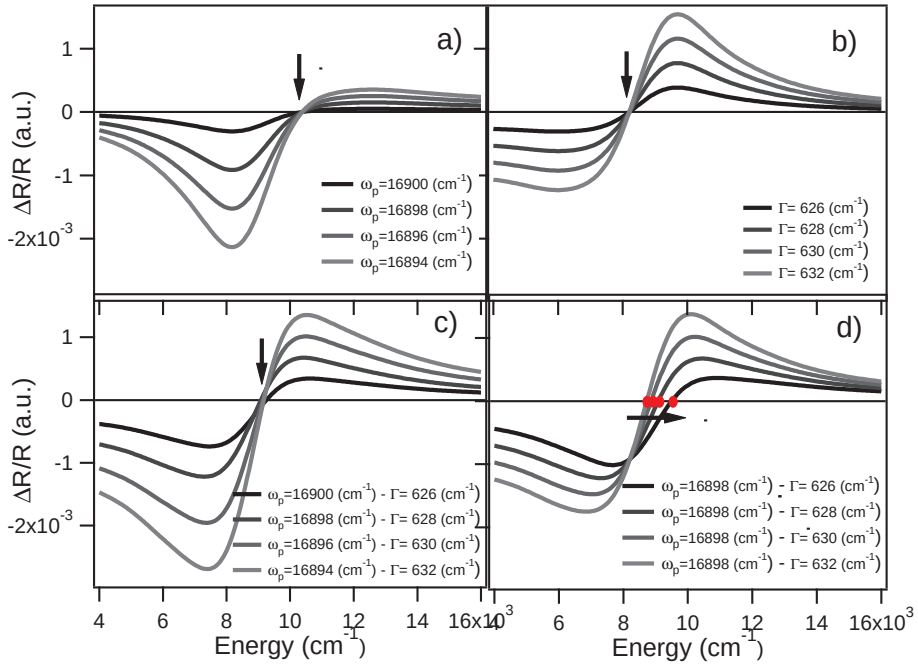

Figure 7.7: $\Delta R/R$ simulations obtained from the differential Drude model. The equilibrium dielectric function, used in the differential fit, is obtained by the interpolation of the static reflectivity with a Drude model. $\Delta R/R$ obtained by varying (a) only the plasma frequency ω_p, (b) only the width Γ, (c) linear variation of ω_p and Γ (d) variation of Γ with ω_p not in equilibirum. The last possibility is the one that simulate a shift of the crossing point (red points).

To be more precise a positive variation of the kinetic energy corresponds to an ω_p variation of the opposite sign. The T-dependence of ω_p is exploited by considering the Sommerfeld expansion of the total energy U of a non-interacting electron gas:

$$U = U_0 + \frac{\pi^2}{6}\left(k_b T^2\right) g\left(E_F\right) \tag{7.1}$$

where U_0 is the ground state energy and $g(E)$ is the density of energy levels [8].
Γ includes the impurity scattering rate Γ_{imp} and, in the case of HTSC, another term related to both T_e and T_b (see formula 3.11). The T-dependence of Γ results in a narrowing of the Drude peak with decreasing the temperature which has been observed by many experimental groups [11]. The variation of the optical oscillators is not related to a simple heating effect which affects only the thermal distribution of electrons and bosons but to a rearrangement of the electronic bands.
In this section we try to determine the physical parameters that cause the transient variation of the signal by adopting a phenomenological differential model. We fit the equilibrium reflectivity in the intraband optical region, by using a simple Drude model, with a temperature dependent width of the Drude peak. The reflectivity in the interband optical region, is reproduced by adding to the equilibrium dielectric function the oscillator reported in table 5.2. We make the assumption that the

variation of the signal in normal state can be explained in term of a thermal effect and, for the moment, we limit to vary only ω_p and Γ. In fig. 7.7 we show the result of the simulation of the simplified differential model. The variation of ω_p (fig. 7.7a) gives rise to a more prominent negative signal with a no-varying crossing point at higher frequencies. 7.7a) we simulate the reflectivity variation caused by a simple broadening of Γ: $\Delta R/R$ seems to reproduced well the shape of the signal and the crossing point frequency is near to the experimental value but it doesn't shift in time. Even if we change ω_p and Γ both linearly (left-bottom figure) we don't obtain any shift. The unique way to obtain this effect consists on changing Γ while keeping fixed ω_p (right-bottom figure). This means that the blue shifting of the crossing point, observed in our measurements, has to be ascribed to a different temporal dynamics (with different decay times) of ω_p and Γ. In the spectral region far from the crossing point the experimental $\frac{\Delta R}{R}$ is mainly affected by the thermal induced variation of Γ.
In conclusion, the tunability of the frequency of the probe pulse has allowed us to explore the temporal evolution of $\Delta R/R(t,\omega)$ over a wide energy window. A change of sign of the fractional reflectivity is found at $\hbar\omega_{probe} \sim$ 1eV both for optimally and overdoped sample. In the frequency region far from the crossing point the dynamics depends only on the broadening of the Drude peak and is characterized by two decays in agreement to what observed in metals. Since in an HTSC the conduction electrons interact with a broad spectrum of bosons, the resulting Drude peak broadness extends until the visible region and its transient variation is sensed as a reflectivity change. Near the crossing point the temporal dynamics is more complex because $\Delta R/R$ depends on the temporal modification of both ω_p and the Drude width. In the extended Drude model the last term is expressed in term of the electronic T_e and bosonic T_b temperature. Since in a time resolved experiment, the electrons population is driven in a condition out of equilibrium with respect the boson and on a subpicosecond time scale $T_e \neq T_b$, it is necessary to study the effect of the temperature disentangling on the Drude broadening. This will be done in the next section.

7.6 Differential model

7.6.1 Non-equilibrium dielectric function

We describe now in detail, the differential model developed to account the T_e and T_b decoupling and fit our measurements. As we have reported in the last section, the variation of the reflectivity, in normal state, is ascribed to ω_p and to the broadening of the Drude peak that depends both on T_e and T_b.
Since in a non-equilibrium measurement, the system is perturbed by a laser pulse, its physical properties change and depend on the delay time τ between pump and probe pulse. In particular the relative variation of the reflectivity is given by:

$$\frac{\Delta R}{R}(\omega,\tau) = \frac{R_{exc}(\omega,\tau) - R_{eq}(\omega)}{R_{eq}(\omega)} \tag{7.2}$$

where $R_{exc}(\omega,\tau)$ and $R_{eq}(\omega)$ are the out of equilibrium and equilibrium reflectivi-

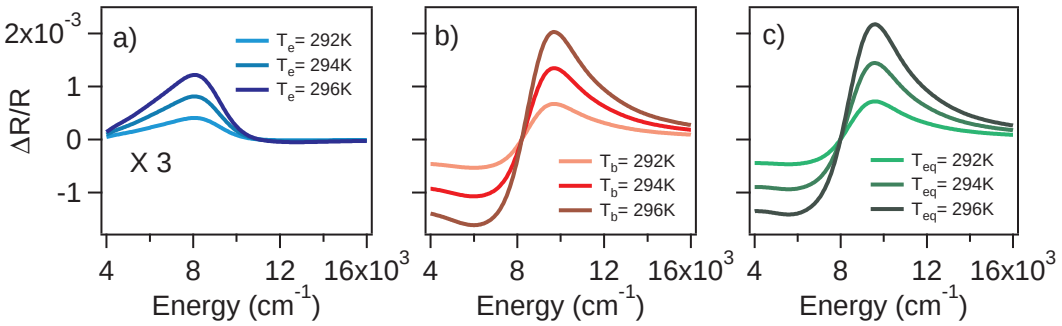

Figure 7.8: Simulated $\Delta R/R$ obtained by varying (a) only the electronic temperature,(b) only the bosonic temperature, (c) boson and electron temperature in equilibrium

ties. The reflectivity and the dielectric function are connected by this relation:

$$R(\omega) = \left| \frac{\sqrt{\epsilon(\omega)} - 1}{\sqrt{\epsilon(\omega)} + 1} \right|^2 . \tag{7.3}$$

R_{eq} is well described by the extended Drude model of the dielectric function $\epsilon(\omega)$ (3.8), described in chapter (3.2.1). The parameters used to interpolate R_{eq} are reported in table (5.2). We start to develop the differential model from the static model used to fit R_{eq} and introducing the temporal dependency of the parameters. R_{eq} contains all the physical change induced by the pump and it is written in term of the time-dependent version of dielectric function $\epsilon(\omega)$ reported here for sake of clarity:

$$\epsilon(\omega,\tau) = \epsilon_\infty - \frac{\omega_p^2}{\omega(\omega + \Sigma_{opt}(\omega,\tau))} + \text{interband oscillators} \tag{7.4}$$

$\Sigma_{opt}(\omega,\tau)$ is the time dependent optical self-energy defined as:

$$\frac{\Sigma_{opt}(\omega,\tau)}{\omega} = \left(\int \frac{f(\xi, T_e(\tau)) - f(\xi+\omega, T_e(\tau))}{\omega + \Sigma^*(\xi, T_e(\tau), T_b(\tau)) + \Sigma(\xi+\omega, T_e(\tau), T_b(\tau)) + i\Gamma_{imp}} \right)^{-1} - 1. \tag{7.5}$$

The temporal dependence of $\Sigma_{opt}(\omega,\tau)$ comes from both the electronic $T_e(\tau)$ and the bosonic temperature $T_b(\tau)$ through the kernel function $L(\omega,\Omega,T)$ (3.11) since the single particle self-energy, in the strong coupling formalism, is written as the convolution integral between the electron-boson coupling function and the kernel-function (see chapter 3.2.1). The bosonic temperature enters into the imaginary part of $L(\omega,\Omega,T)$ through $n_{BE}(\Omega,T_b)$ while the former enters both in the real part of $L(\omega,\Omega,T)$ and in the Fermi-Dirac distribution $f_{FD}(\omega,T_e)$.
Our approach is finally to fit the experimental variation of the reflectivity $\Delta R/R(\omega,\tau)$ with the function (7.2) at different delays modifying only the parameters: T_e, T_b and ω_p. We will show later on that, in the normal state, it's not necessary to change the parameters of the interband oscillators to obtain a good fit.
The use of the formalism in (7.5) also opens the possibility to disentangle the effects of $T_e(\tau)$ and $T_b(\tau)$ on the differential signal.

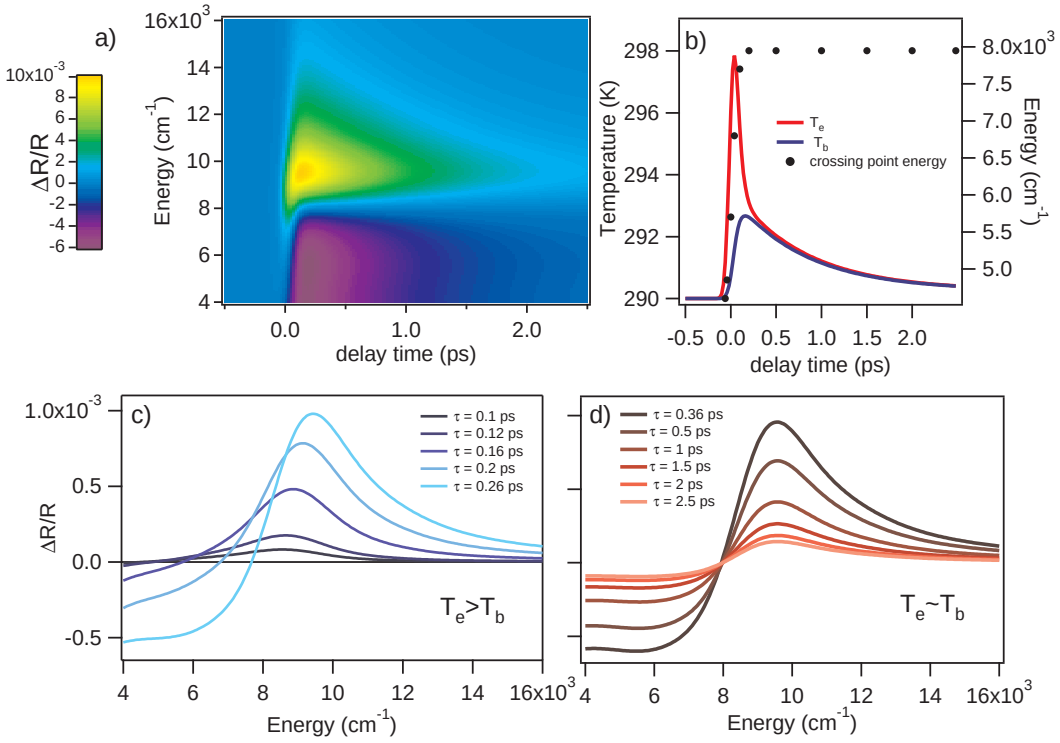

Figure 7.9: (a) Simulated temporal evolution of the differential reflectivity obtained by putting in the differential model the temporal variation of value of T_e and T_b shown in (b). In (c-d) the cut at different delay times, of the 2D simulation are reported. During the first 200 fs (c) the signal is consistent with an increase of T_e decoupled from T_b. When T_b starts to increase the crossing point shift towards higher frequencies until the equilibrium between T_e and T_b is reached (d). In (b) the shift of the crossing point (black point) is reported.

In fig.7.8a-b we report the expected $\Delta R/R(\omega)$ obtained by simulating alternatively the heating of the electrons and bosons. In the first case, the resulting signal is positive below $\sim$9000 cm^{-1} and close to zero at higher energy. On the contrary, the heating of the bosons alone induces a $\Delta R/R$ signal which is negative in the infrared region and changes sign at about 8000 cm^{-1}. The differential reflectivity caused by a quasi-thermal temperature variation (i.e. $T_e \sim T_b$), simulated in fig. 7.8c, has a similar shape of the T_b-heating induced signal, suggesting that, at equilibrium, the boson temperature overwhelms the contribution of the electronic temperature increase. This shape of the reflectivity variation is typical of a temperature-related broadening of the Drude peak (see fig. 7.7b).
Once $T_e(\tau)$ and $T_b(\tau)$ are determined by fitting the one-color pump-probe measurements with the numerical solutions of the three temperature model (fig. 7.6), we can simulate the temporal behaviour of $\Delta R/R(\omega, \tau)$ using the formula (7.2). The result of the simulation is reported in fig. 7.9a together with the cut at different delay times (fig. 7.9c-d)). We stress that, in this case, the parameters, used to calculate R_{eq} and R_{exc}, are obtained from the fit of the OP96 sample at T=290 K, and the temporal profile of T_e and T_b is calculated with a laser fluence of $10\mu J/cm^2$ and an

electron-boson coupling constant λ=0.08.
Following closely the behavior of the $\Delta R/R(\omega)$, we find that since the electron and boson populations are not yet thermalized, during the first 200 fs, the main contribution to the resulting signal comes from the out of equilibrium electronic carriers. When the bosonic temperature starts to increase, the crossing point shift towards higher energies and a negative signal develops in the infrared region. The crossing point temporal dynamics fades out after 0.3 ps when the electron-boson thermalization is reached, as shown in fig. 7.9b. At larger delays the simulated signal is in accord with a quasi-thermal decreasing of the equilibrium temperature (fig. 7.9d).
Comparing the simulations based on the three temperature model to our results, we find a discrepancy between the experimental $\Delta R/R(\omega,\tau)$ at τ=0 ps (i.e. the energy-resolved spectrum integrated over the first 100 fs) and the simulated one (see fig. 7.9c). This discrepancy is observed only on a fast time scale (<0.3 ps) and can be understood in term of the temporal behaviour of T_e and T_b. The fast and positive signal below 1.2 eV, which is totally absent in our measurements, is due to the fact that T_b has a rise time slower than T_e (fig. 7.9b) and the electrons reach the highest temperature when the bosons start to get excited. In our case the shape of the reflectivity variation at τ=0 ps can be explained in term of a sudden increase of the bosonic temperature.

7.6.2 Kramers-Kronig constraint

Before showing the results of the differential fits, it is necessary to check if the non-equilibrium model presented before satisfy the Kramers-Kronig (KK) transform. These integral relations connects the real and imaginary part of the response function of a physical system and they are the consequence of the principle of causality.
In the case of the complex optical conductivity $\sigma(\omega)$ the KK-relations assume the following form:

$$\sigma_1(\omega) = \frac{1}{\pi} P \int_{-\infty}^{+\infty} \frac{\sigma_2(\omega')}{\omega' - \omega}\, d\omega' \tag{7.6}$$

$$\sigma_2(\omega) = -\frac{1}{\pi} P \int_{-\infty}^{+\infty} \frac{\sigma_1(\omega')}{\omega' - \omega}\, d\omega' \tag{7.7}$$

where P is the principal part of the integral.
In the frame of the generalized Drude model (chapter 3.2.1), the constant damping term in $\sigma(\omega)$ is substituted by a complex and frequency dependent optical self-energy function $\Sigma_{opt}(\omega)$. Inverting the formula 3.3, we can express the real and imaginary part of $\Sigma_{opt}(\omega)$, respectively $1/\tau(\omega)$ and $\lambda(\omega)$, in term of $\sigma(\omega)$:

$$\frac{1}{\tau(\omega)} = \frac{\omega_p^2}{4\pi} Re\left(\frac{1}{\sigma(\omega)}\right) \tag{7.8}$$

$$1 + \lambda(\omega) = -\frac{\omega_p^2}{4\pi}\frac{1}{\omega} Im\left(\frac{1}{\sigma(\omega)}\right) \tag{7.9}$$

Since $\sigma(\omega)$ is causal, $\lambda(\omega)$ and $1/\tau(\omega)$ are not independent but they are related by the KK relations [3, 11].

On the contrary the validity of these relations is not discussed in the literature,

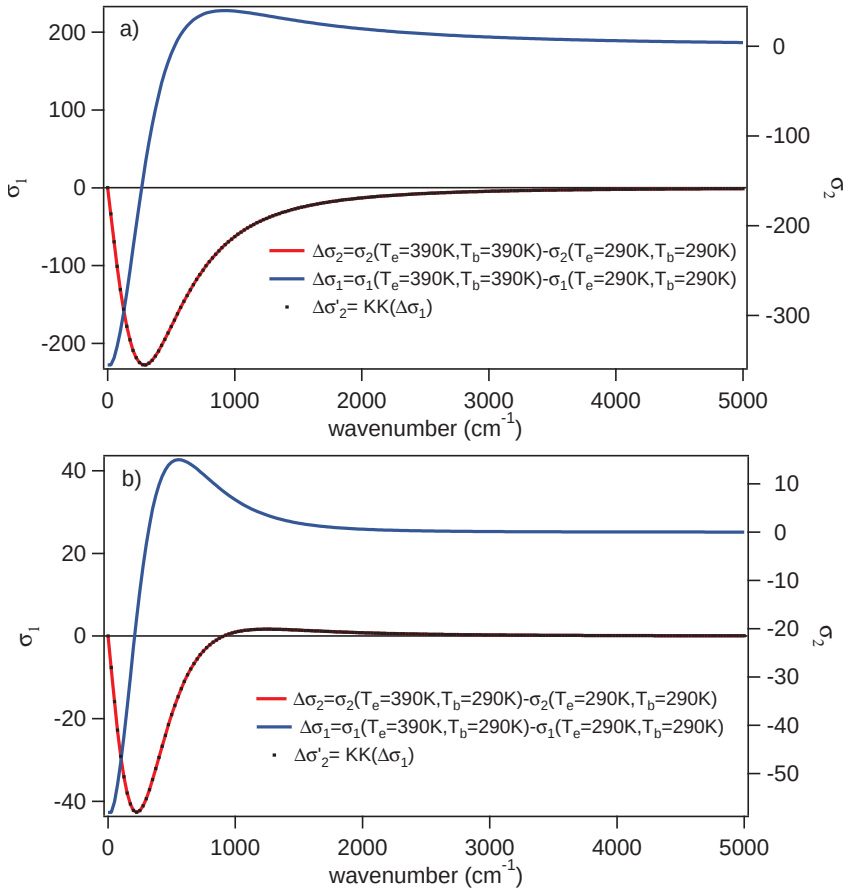

Figure 7.10: Real (blue) and imaginary (red) part of the differential optical conductivity obtained by a quasithermal increase of T_e and T_b(a) and by an independent increase of T_e (b). The KK transform of $\Delta\sigma_1$ overlaps $\Delta\sigma_2$ indicating that the differential model satisfies the KK relations in both the case.

for $\sigma(\omega)$ written in term of the electron and hole self-energies (eq 3.8) both in the equilibrium and in the non-equibrium scenario, when T_e is no longer tied to T_b.
To tackle this question, we adopt a simplified model given by a Drude oscillator strongly coupled with a bosonic spectrum $\Pi(\Omega)$. The parameters of the model are reported here in succession: ϵ_∞=1, ω_p=5000 cm^{-1}, Γ_{imp}=50 cm^{-1}. The electron-boson coupling function is a simplified version of the one reported in fig. 5.7 at T=290 K where the broad spectrum of electronic origin is removed. The real and imaginary part of the differential conductivity $\Delta\sigma(\omega)$ (respectively the red and blue curve) are calculated in two different cases: an increase of the equilibrium temperature (ΔT_e=ΔT_b), reported in fig. 7.10a, and of the electronic temperature decoupled from the bosons ($\Delta T_e > \Delta T_b$) in fig. 7.10b.
In both situations, the KK-trasform of the real part of the differential conductivity $\Delta\sigma_1(\omega)$ (black points) exactly reproduces the $\Delta\sigma_2(\omega)$ calculated from the model. The result demonstrates that the non-equilibrium model is consistent with the KK relations and confirming the reliability of our approach.

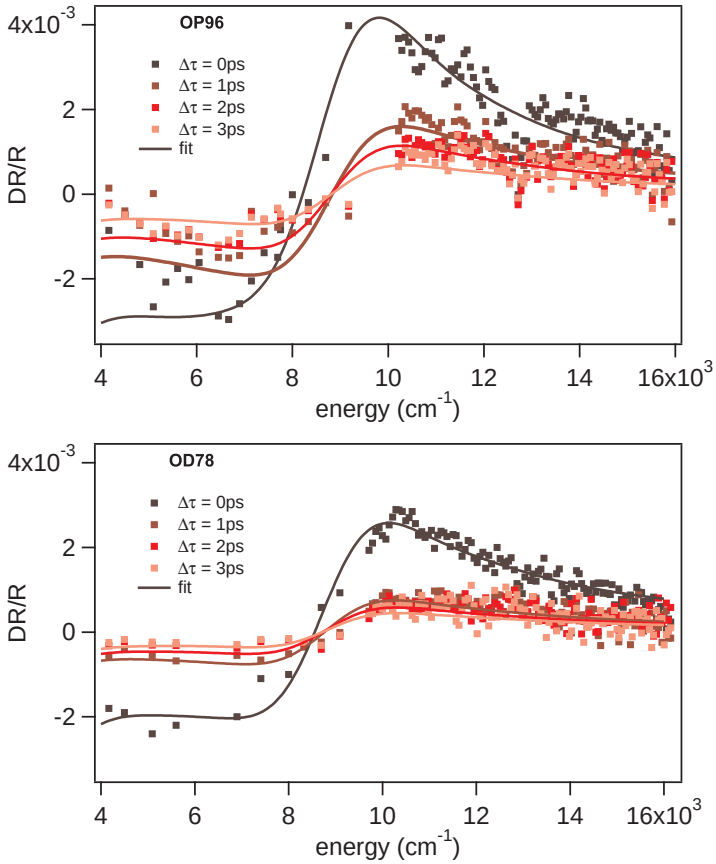

Figure 7.11: Energy resolved spectra carried on OP96 and OD86 at different delay times. The fit to the curves is given by the function 7.2 (continuous lines). The parameter of the fit are listed in table 7.1

7.6.3 Fits and discussion

In fig. 7.11 we report the energy resolved relative variation of reflectivity $\Delta R/R(\omega, \tau)$ at different delay times for OP96 and OD86 samples. The solid lines are the best differential fit of the function 7.2 to the data. The fit satisfactorily reproduces the shape of the experimental data and the table 7.2 lists the best values of the free parameters in the fitting procedure. The parameters reported in the table show that the transient variation of the signal can be explained in term of an increasing of the electronic and bosonic temperatures which thermalize on a picosecond time scale. This thermal effect is accompanied by an impulsive lowering of the Drude plasma frequency ω_p. The combination of these two temporal dynamics gives rise to the crossing point blue shift discussed in the previous section. The resulting ω_p variation confirms the temperature dependence of ω_p observed in equilibrium optical measurements [90] and corresponds to an impulsive increasing of the carriers kinetic energy.

Looking at the energy resolved spectrum measured at τ =0 ps, we note that the fitting results indicate a sudden increase of the temperature of all the bosonic modes

Table 7.2: Parameters used in the differential fit of $\frac{\Delta R}{R}(\omega,\tau)$ to fit the data reported in fig.7.11 at various delay times. The free parameters of the fit are T_e,T_b,ω_p.

sample	parameters	τ=-1ps	τ=0ps	τ=1ps	τ=2ps	τ=3ps
OP96	T_e (K)	290	295.4	292.3	292	291.6
	T_b (K)	290	291.2	290.5	290.35	290.2
	ω_p (cm^{-1})	16901.4	16900.2	16900.5	16900.7	16900.9
OD86	T_e (K)	290	296	291.6	291	290.8
	T_b (K)	290	290.5	290.16	290.1	290.1
	ω_p (cm^{-1})	17389	17387.4	17388.5	17388.5	17388.5

described by $\Pi(\Omega)$. This result calls for a discussion about the nature of the bosons which are involved in this process since, as we have pointed out in the previous chapters, the coupling mechanism between the electronic carriers and the other degree of freedom of an HTSC is a matter of debate. The possibility of a sudden increase of the phonon temperature is rather unlikely since almost the entire energy carried by the pump pulse would be absorbed directly by the lattice on a fast time scale, because of the large difference between the phonon and electron specific heat, and we would observe a quasithermal variation of the temperatures rather than an independent increse of T_e with respect to T_{ph}. Moreover, both time-resolved photoemission [101] and ultrafast electron diffraction measurements [19] results indicate a variation of the electronic temperature ΔT_e much larger than that of the phonon temperature ΔT_{ph}.
The hypothesis that bosonic modes of electronic origin, like spin fluctuations, are involved is more viable because, in this case, the boson contribution to the specific heat C_b is expected to be much smaller than the phonon contribution. The determination of C_b represents a very difficult task because of the difficulty to disentangle it from the electronic contribution C_e. A tentative estimation of the order of magnitude of C_b, was carried on in a theoretical work by Singh *et al.* [113] where the the magnetic specific heat C_m is calculated for the undoped compounds. In the specific case of La_2CuO_4, C_m is estimated to be 6.5×10^{-7} J/cm^3K^2 at T=30 K, i.e. two order of magnitude lower than that the electronic specific heat measured on OP Y-doped Bi2212 at the same temperature ($\gamma_{el}(T = 30K) = 4.2 \times 10^{-5}$ J/cm^3K^2). The specific heat of the spin fluctuations in a doped sample, where the antiferromagnetic order is broken, can only be smaller than C_m.

7.6.4 Disentangling the electronic and phononic glue

The differential fit, reported in the previous section, is obtained by assigning a single temperature to all boson glue described by $\Pi(\Omega)$. This is not completely correct,

Table 7.3: For each bosonic excitation, we report the electron-boson coupling constant λ, the characteristic boson frequency $\tilde{\omega}$ and the corresponding critical temperature T_c resulting from the strong-coupling formalism (eq. 2.6).

Excitations	λ	$\tilde{\omega}$ (cm^{-1})	T_c (K)
Electronic bosons	0.21-0.4	1615.7-1253.5	6.5-45.8
Strongly coupled phonons	0.06-0.1	631-631	$1.8{\cdot}10^{-5}$-$1.5{\cdot}10^{-2}$
Cold phonons	0.47-0.7	631-631	33.4-65.8
All bosons	0.97	940.4	147.8

because the high-energy part of the boson glue has an electronic origin and it is reasonable to suppose that immediately after the pump excitation, it reaches the same temperature of the electronic carriers because of the low specific heat, while the low-energy peak has a controversial origin and could be associated to both phonons and electronic-like bosons. We can try to address this problem assuming that a fraction of this peak is ascribed to the coupling to the electronic degrees of freedom while the remaining part describes the lattice modes. As a consequence, the electronic part of the glue $\Pi_{el}(\Omega)$, represented by the blue colored hystogram in fig. 7.12, is a sum of the broad high-energy continuum and a part of the peak. The phononic part of the peak includes two contributions: the strongly coupled phonons (i.e. in-plane breathing modes-red peak) and the cold phonons (i.e. out-of-plane buckling modes-black peak) which are characterized by two different relaxation dynamics. The first contribution has been determined by the three temperature model fit of the single color pump-probe reflectivity measurements and results to be λ=0.08±0.02.
We repeat the same differential analysis, reported in the previous section, but taking now into account the different parts of the glue function. The free parameters of the fit procedure are the electronic temperature T_e, the hot phonon temperature T_{ph}, the temperature T_{el-bos} and the fraction g of the peak related to the electronic-like bosons. Since the electron population thermalizes instantly with the excitations of $\Pi_{el}(\Omega)$, we fit the $\Delta R/R(\omega)$ with this constraint: ΔT_e=ΔT_{el-bos}. The temperature variation of the cold lattice modes is considered negligible.
The best value g obtained by the differential fit in fig. 7.12 is included between 0.05 and 0.3, meaning that a fraction included between the 5% and the 30% of the peak represents the electronic glue, while the remaining part is ascribed to the cold phonon modes.
The error bars of g are derived by propagating the errors on the temperatures determination. Employing the McMillan formula (2.6), we can evaluate the coupling strength λ and the contribution to T_c of the different excitation belonging to $\Pi(\Omega)$. The results are reported in table(7.3).
Although the contribution of the electronic bosons to T_c is lower than the phononic one, we can assert that the two components alone are not sufficient to account for the high value of the critical temperature. For that reason we can assert that both these different pairing mechanisms play a significant role in HTCS and the phonon-

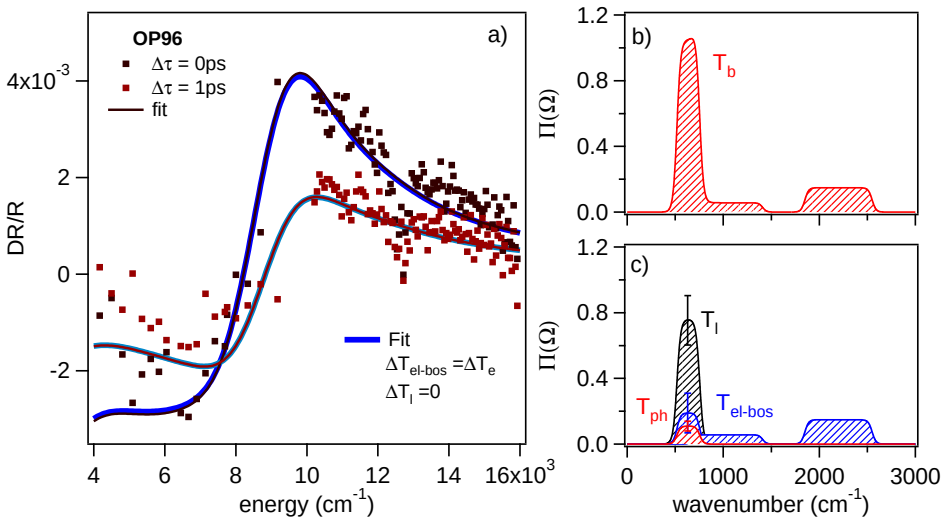

Figure 7.12: (a) Energy resolved spectra carried on OP96 at a delay time of 0 and 1 ps(squares) and the fit to the curve (brown lines) obtained with the eq. 7.2 and the parameters listed in table 7.2. The differential fit are performed by treating all the boson modes as a population out of equilibrium at a temperature different from the electronic temperature as shown in (b). The blue thick lines are the $\Delta R/R$ differential fit obtained by disentangling the electronic and phononic part of the glue spectrum. The fitting constraints are reported in the inset. The free parameters of the differential fit are T_e, T_{el-bos}, the hot phonon temperature T_p, and the fration g of the low-energy peak related to the spin fluctuation modes.(c) Different portions of the boson glue obtained as the result of the fit. The blue histrogram represents the contribution to the pairing between the electrons and the bosons of electronic origin. The low-energy excitations of electronic origin represent a fraction between the 5% and the 30% of the total peak spectral weigth. The red and black peaks are attributed respectively to hot and cold phonon modes.

mediated pairing mechanism is accompanied by a pre-existing strong electron-boson interaction as suggested by many recent works [60, 61, 88].
These results seem to suggest a physical scenario in which the temporal dynamics of the electronic carriers brought out of equilibrium by an ultrafast laser pulse, is governed, on a fast time scale, by a strong coupling to the electronic part of the spectrum $\Pi(\Omega)$. In particular an important role is played by the low-energy part of the bosonic excitations spectrum which seems to include more contributions of different nature. The thermalization between electrons and spin-fluctuations occurs in a very short delay time; after that the system starts to lose energy interacting with a subset of phonon modes (hot phonons) which, in turn, relax by inelastic scattering with the other phonon modes (cold phonons) according to the three temperature model.

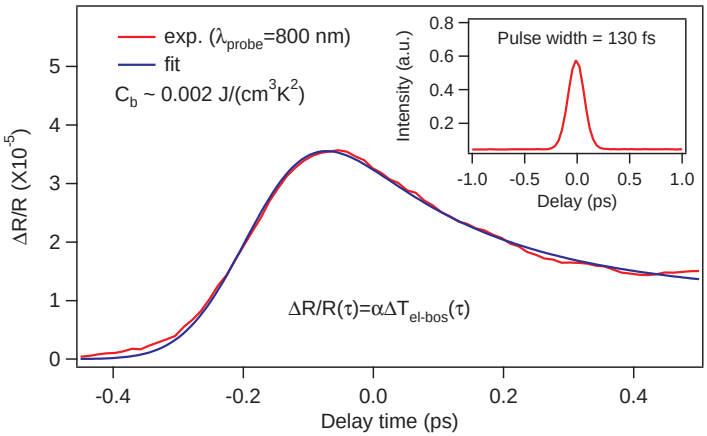

Figure 7.13: Differential reflectivity measured on OP96 sample at T=290K using a probe pulse at 800 nm (red curve). Fit of the data with the numeric solution of the equation 6.10 (blue curve). Since the bosons of electronic origin thermalize instantly with the electrons, the relative variation of the reflectivity on a fast time scale (<1 ps) depends on the transient variation of T_{el-bos}. The fit result provides a value of C_b ~0.002 J/cm^3K^2 which is ten times lower than C_e. In the inset the temporal profile of the pump pulse is shown.

7.7 Four temperature model

It is possible to extend the three temperature model to our case, including a term related to the thermalization between the electronic carriers and the electronic part of the boson glue. The formalism adopted to describe the electron-phonon relaxation can be generalized to any other boson mode [5]. The electronic energy relaxation rate can be written as:

$$\frac{dE_e}{dt} = 2\pi N_c N(\epsilon_F) \int_0^\infty d\Omega \Pi(\Omega) (\hbar\Omega)^2 (n_e - n_b) \tag{7.10}$$

where n_b is a generic boson distribution function at a temperature T_b. If we treat the electrons system as a free particles gas the heat capacity coefficient γ_{el} is:

$$\gamma_{el} = \frac{\pi^2}{6} N_c N(\epsilon_F) (k_b T_e)^2 \tag{7.11}$$

where N_c is the number of primitive cells and $N(\epsilon_F)$ is the density of states of both spins per unit cell. We can use the formula (7.11) to convert eq. (7.10) into a temperature relaxation rate, obtaining the following rate equations system:

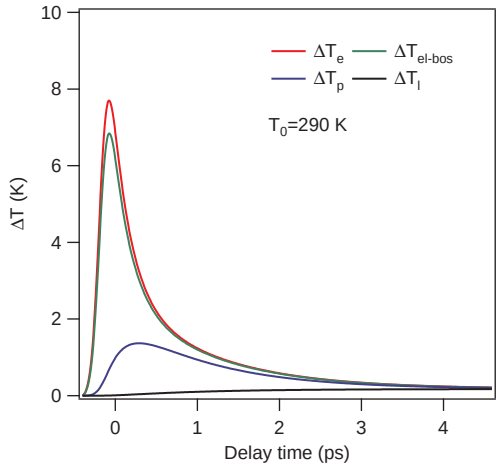

Figure 7.14: Temporal profile of the temperature (electrons, electronic bosons, hot phonons, cold phonons) obtained by the numeric integration of the rate equations 6.9-12 with the parameters obtained by the fit of the data shown in fig. 7.12. The pump fluence is 10 $\mu J/cm^2$.

$$\frac{dT_e}{dt} = -\frac{2}{k_b^2 \pi T_e} \int_0^\infty \Pi_{el}(\Omega) (\hbar\omega)^2 (n_e - n_b)\ d\Omega + \frac{P}{C_e} \tag{7.12}$$

$$\frac{dT_{el-bos}}{dt} = \frac{C_e}{C_b} \frac{2}{k_b^2 \pi T_e} \int_0^\infty \Pi_{el}(\Omega) (\hbar\omega)^2 (n_e - n_b)\ d\Omega - \frac{T_{el-bos} - T_p}{\tau_\alpha} \tag{7.13}$$

$$\frac{dT_p}{dt} = \frac{C_b}{C_p} \frac{T_b - T_p}{\tau_\alpha} - \frac{T_p - T_l}{\tau_\beta} \tag{7.14}$$

$$\frac{dT_l}{dt} = \frac{C_p}{C_l} \frac{T_p - T_l}{\tau_\beta} \tag{7.15}$$

where C_b is the bosonic specific heat. Note that it is straightforward to obtain the equation (2.17) directly from the equation (6.9) approximating the boson spectrum by an Einstein model.
The first equation of the system represents the temporal evolution of the electronic temperature: the rapid increase of T_e is due to the photon absorpition and to the strength of the electron-electron interaction and electron-boson interaction, the last given by the integral over the frequency of $\Pi_{el}(\Omega)$, obtained by the differential fit previously shown. The time dependence of the bosonic excitation is exploited in the second differential equation: the rise-time depends both on $\Pi_{el}(\Omega)$ and on the ratio between C_b and C_e. Because of the low C_b value (i.e. lower than C_e in the case of spin fluctuation), τ_r is extremely fast (i.e. of the order of fs) and it is limited by the temporal resolution of the pulse. Moreover the electrons exchange istantly their energy with the electronic bosons and a quasithermal evolution of T_e and T_{el-bos} is expected to occur even on an ultrafast time scale. The last term of the second equation describes the following cooling process due to the scattering with the strongly interacting subset of phonon modes. The last stage of energy relaxation is described by the remaining rate equations and it is related to the anharmonic decay of hot phonons.

We use now this extended version of the three temperature model to reproduced the one-color time-resolved measurements, as we did in fig.(7.5). We focus on the rise dynamics of $\Delta R/R$ and we try to give an estimation of C_b. Because of the instantaneous thermalization between electrons and bosons, it is justifiable to assume that $\Delta R/R \propto T_{el-bos}(\tau)$ and to fit the data with the temporal profile of T_{el-bos}. The result of the fit is reported in fig.(7.13) together with the relative variation of the reflectivity taken at λ_{probe}=800 nm. Since C_e is experimentally determined and $\Pi_{el}(\Omega)$ was previously obtained by the differential analysis, the parameter C_b is adjusted by the fit in order to reproduce the rise dynamics giving the result: $C_b \sim 0.002$ J/cm^3K^2, which is one order of magnitude lower then C_e (~ 0.029 J/cm^3K^2 at room temperature).

7.8 Conclusion

The time and frequency-resolved variation of reflectivity, measured in normal state, is reported in this chapter. We have studied the frequency-resolved traces at different delay times by developing a differential dielectric function to reproduce the temporal evolution of the spectral feautures. The equilibrium dielectric function and the bosonic glue have been derived previously in the frame of the Extended Drude model. The strong-coupling formalism, used here to describe the equilibrium physical properties, has allowed us to study separately the contribution to the transient signal of the electrons and bosons. The differential fit to $\Delta R/R$, integrated over the first 100 fs of delay time, strongly differs by the physical scenario depicted by the three temperature model and can be explained in term of a sudden increase of the temperature of part of the bosons. The istantaneous coupling between the electronic carriers with a part of the bosonic glue is a signature of the electronic origin of these bosonic modes. The physical scenario, we have proposed to explain the dynamics of $\Delta R/R(\omega, t)$ on a fast time scale, relies on the strong coupling between the electrons and the electronic part of the spectrum $\Pi(\Omega)$. On a slower time scale, the system starts to exchange energy with the hot phonons modes, which in turn relax in a hundreds of picoseconds by an anharmonic decay with the remaining cold lattice modes. We have given an estimation of the strength λ of the different excitations belonging to $\Pi(\Omega)$ and we have determined the corresponding contribution to the critical temperature T_c by employing the strong-coupling McMillan formalism. We have obtained a λ that ranges between 0.21 and 0.4 for the bosons of electronic origin and a T_c between 6.5 K and 45.8 K. In the phonon case (i.e. cold and hot phonon modes) λ varies from 0.053 to 0.8 with a T_c that reach the maximum value of $\sim$66 K. Considering that the total coupling, obtained by integrating $\Pi(\Omega)$, is 0.97 and T_c is $\sim$148 K, we can conclude that the high critical temperature in HTSC is determined by the electronic coupling with both bosonic and phononic modes and the two mechanism alone are not sufficient to explain the superconductivity in cuprates as suggested in many works (see [60, 61, 88] and references therein).

Chapter 8

Pseudogap phase

8.1 Introduction

In this chapter we study the optical response in both the time and frequency domains in the pseudogap phase at T=100 K. The variation of reflectivity measured below the pseudogap temperature T^* is completely different from that measured in normal state. When T^* is crossed, the transient optical response of the system changes drastically with respect the normal state response. This effect can not be explained in term of an excited state absorption or an effect due to a modification of the equilibrium dielectric function but it is a genuine response of the system in the pseudogap phase. The differential fit indicates a transient increasing of the Drude plasma frequency and a weakening of the electron-boson coupling suggesting that the pseudogap is accompanied by an opening of a gap in the density of the electronic state and is characterized by a temperature dependent modification of the bosonic glue.

8.2 Experimental data

In fig. 8.1 we report the time and frequency resolved reflectivity $\Delta R/R(\omega, t)$, between 1.25 eV and 2 eV, carried on the samples UD83, OP96 and OD86 at T=100K. In chapter 6 we have estimated, by studying the sign-flip of the transient signal $\Delta R/R(t)$, the edge of the pseudogap phase temperature T^* to be $\sim$220 K and $\sim$150 K for UD83 and OP96 respectively. In OD86 we did not observed any change of sign of the relative reflectivity. This result seems to suggest that the pseudogap phase in the overdoped sample is strongly quenched, in accord with physical scenario in which the pseudogap line merges into the superconductive dome in the overdoped region. At this temperature, the frequency resolution unveils a more structured ω-dependance of the reflectivity variation. In under and optimally-doped samples a positive variation is measured below $\sim$1.35 eV, while a negative and flat signal extends up to the UV region. In the over-doped sample, the high-energy negative response is quenched, while the positive structure at 1.3 eV persists. This feauture is absent in the normal state.

For each 2D plots we report the time traces obtained by cutting the supercontin-

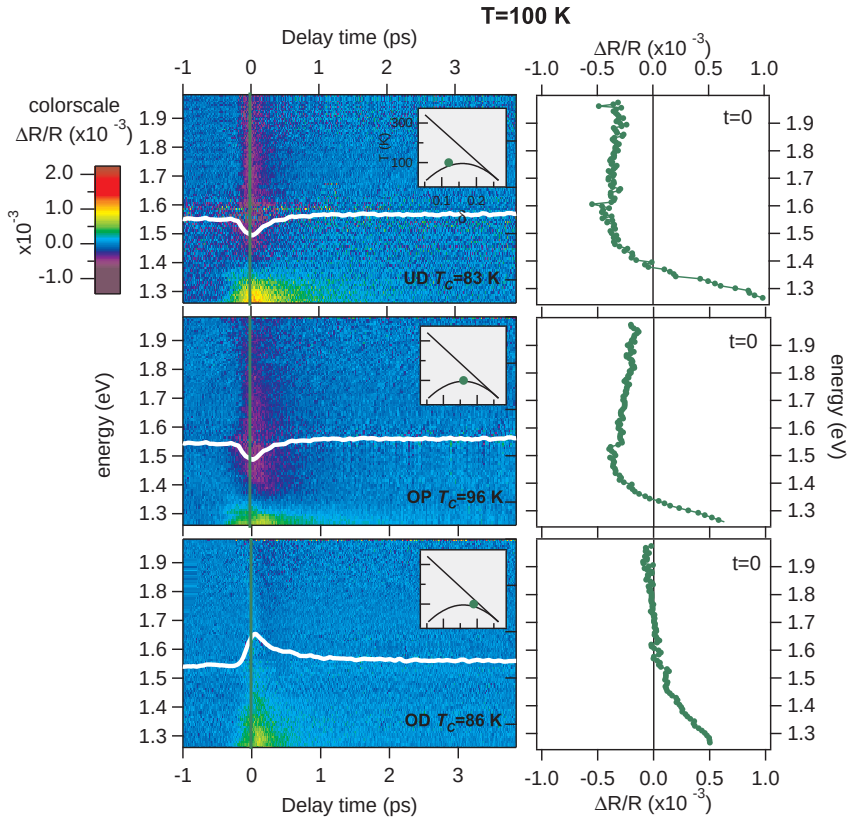

Figure 8.1: Energy and time-resolved reflectivity on $Bi_2Sr_2Ca_{0.92}Y_{0.08}Cu_2O_{8+\delta}$. The 2D scan are reported for different doping range at T=100K. The colour scale of the reflectivity variation amplitude is reported on the top left of the figure. The insets display the position of each scan in the T-δ phase diagram. The white lines are the $\frac{\Delta R}{R}(t)$ traces obtained at λ_{probe}=800nm. The green line represents the cut at the delay time τ=0 ps. The energy resolved spectra $\Delta R/R(\omega, \tau = 0)$ are reported next to the respective 2D plot.

uum measurements at λ_{probe}=800 nm, which display the same temporal behaviour of that observed in chapter 6 in one color pump-probe reflectivity. In particular a fast transient component, with a decay time of ∼400 fs, followed by a slow component is recorded. It is interesting to note that, at higher delay times (>2 ps), the signal becomes positive even for the under and the optimally doped sample.
In fig. 8.2a we report the data obtained from the supercontinuum probe technique extended in the infrared region down to 0.5 eV employing the ultrashort pulses provided by the OPA system for the OP96 sample. The total energy extension of the probe ranges from 0.5 eV to 2 eV. Shifting the probe energy towards the infrared region, the transient signal decreases and changes sign at about 0.55 eV.

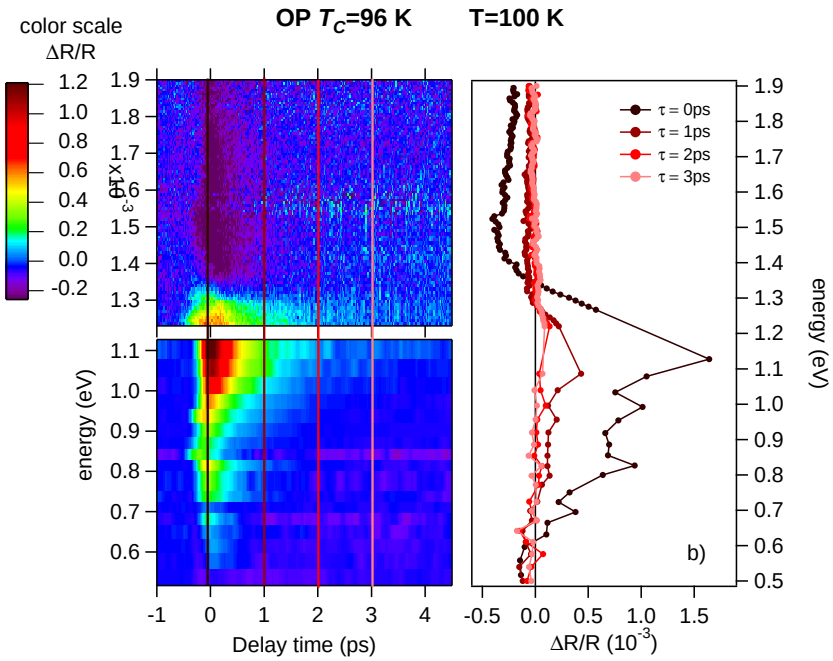

Figure 8.2: (a) Pump-supercontinuum probe reflectivity measurements (top) jointed with pump-OPA probe reflectivity measurements (bottom) carried on OP96 at T=100K. The total probe energy range is 0.5-2 eV. The pump fluence I_{fl}=10 $\mu J/cm^2$ per pulse. The straight line represents the temporal cut of the 2D spectra. (b) Energy resolved spectra at different delay times.

8.3 Fit and discussion

At this point, we want to address the question about the origin of the transient optical response observed in pseudogap phase.

8.3.1 Quasithermal modification of the reflectivity

Fig. 8.3 displays the equilibrium temperature variation of the reflectivity ΔR_{eq} on the OP96 sample, being ΔR_{eq} the difference between the reflectivity measured by optical ellipsometry at a given temperature. The positive value of ΔR_{eq} over all the probe photon frequency range shows how the structured responses measured in the pseudogap and in the superconductive state (as we will see in the following chapter) are incompatible with a quasithermal scenario where the underlying electronic structure is unchanged, while the effective temperatures are impulsively

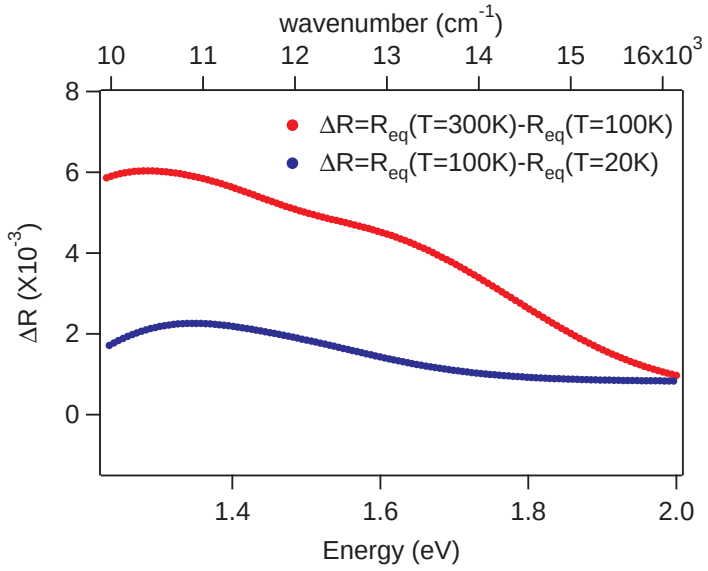

Figure 8.3: Reflectivity difference ΔR obtained by subtracting the fit of the equilibrium reflectivity of OP96 at different temperatures as shown in the inset.

increased of $\Delta T(t)$. In this case the transient reflectivity variation can be expressed as $\Delta R/R(\omega,t) = [(1/R)(\partial R/\partial T)(\omega)]\,\Delta T$ and would be expected proportional to the time-integrated measured ΔR_{eq}, reported in fig. 8.3, which does not exhibit any structure or change of sign.
The reflectivity variation in pseudogap state is not due to a simple heating effect and can not be explained as a difference between two thermal equilibrium states characterized by different temperatures T and T+ΔT being ΔT related to the increase of the internal energy provided by the pump pulse.

8.3.2 Role of the $\epsilon_{eq}(\omega)$

$\Delta R/R(\omega)$ does not depend on the starting equilibrium dielectric function by checking fig. 8.4a where we report on the same graph the calculated differential reflectivity induced by a quasithermal variation of the temperatures ($T_e(t) \sim T_b(t)$) when the sample is in normal state and in pseudogap state at T=100 K.
Although the equilibrium dielectric functions and the bosonic glue spectra $\Pi(\Omega)$, shown in the inset, at T=290 K and T=100 K are different, the shape of the reflectivity variation is qualitatively similar in both the cases.
The simulation of an increase of the electronic temperature decoupled from the temperature of the high-energy bosonic modes is shown in fig. 8.4b. Also in this case the resulting shape of $\Delta R/R(\omega)$ in pseudogap phase mimics the normal state behaviour and it is completely different from the experimental results, demonstrating that an effective temperature variation of the different parts of the glue is not suitable alone to reproduce the transient signal variation.

8.4 Differential fit

In the previous sections we have demonstrated that the transient optical response of the system in the pseudogap phase can not be explained as a thermal effect and does not depend on the equilibrium dielectric function but it is an intrinsic response of the system caused by the pump light pulse.
The differential fit function, shown in fig. 8.5, reproduces qualitatively well the experimental energy resolved traces and indicates a transient increasing of the Drude plasma frequency accompanied by a lowering of the intensity of the low-energy part of the electron-boson coupling function. We want to show how the variation of these parameters can change the $\Delta R/R(\omega)$. The impulsive increasing of the plasma frequency ω_p, simulated in fig. 8.4c, gives rise to a positive variation of the reflectivity in the infrared region below $\sim$1 eV and a lower signal in the visible (red curves).
The differential fit of the OP96 and OD86 samples, are displayed in fig. 8.4 along with the corresponding energy-resolved spectra integrated over the first 200 fs of delay time, and qualitatively capture the shape of the experimental data in both the cases.

The results of the best fits to the data suggest that, beyond the increasing of the temperature $T_e(t)$ and $T_b(t)$, the reflective variation on a fast timescale in pseudogap phase, can be attributed to an impulsive increase of ω_p accompanied by a weakening of the lowest-energy boson peak. The variation of ω_p shows an opposite trend with respect that observed in normal state where the Drude plasma frequency undergoes a transient lowering according to a corresponding increasing of the kinetic energy of the charge carriers. The observed variation of ω_p could be associated to the presence of a gap above T_c. The opening of a gap causes the piling up of the electronic density of states at the gap edge while the unoccupied states are pushed toward higher energies above the gap. This means that, when the carriers are excited above the gap, they find to have an increased kinetic energy. When the pump pulse hits the sample, it strongly perturbes the electronic distribution causing the closing of the gap. The pump-induced quenching of the gap, causes the transient decreasing of the carriers kinetic energy which corresponds to an opposite variation of ω_p.
The physical scenario we have proposed before, is true only if the pseudogap is a "'real"' gap in the electronic density of states. This point is strongly discussed and no general consensus has been reached. A large number of spectroscopic techniques, which can probe directly the pseudogap phase like ARPES and STS, are not able to distinguish if this gap is related to a suppression of the density of states at the Fermi level rather than a suppression of spectral weight in the single-particle spectral function [55]. The differential fit results seems to point to the first hypothesis.

The glue function extracted from the equilibrium optical measurements in pseudogap phase sensibly differs from the one in normal state. In particular a low-energy peak, centered on 36 meV, appears in $\Pi(\Omega)$, upon lowering the temperature and it could be involved in the transient response of the system.
The impulsive weakening of the bosonic peak, simulated in fig. 8.4d, could be related to the magnetic collective mode observed in inelastic neutron scattering measurement in many families of cuprates [73]. Its energy ranges between 52 and 56 meV in the case of $HgBa_2CuO_{4+\delta}$ and it is close to the energy of the peak (36$\pm$16 meV)

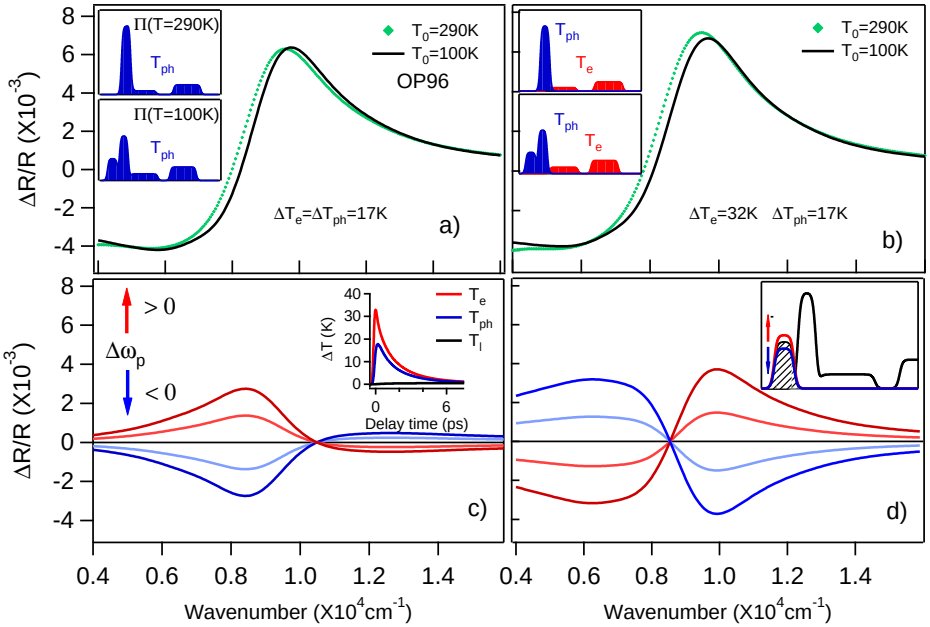

Figure 8.4: (a) Calculated differential reflectivity assuming that the electronic population is thermalized with all the spectrum of bosons (i.e. $\Delta T_e \sim \Delta T_{ph}$) and starting from the equilibrium dielectric function of the OP96 sample at T=290 K (green curve) and T=100 K (black curve). The glue functions $\Pi(\Omega)$ in normal and pseudogap phase are reported in the insets of the graph.(b) Differential reflectivity obtained by decoupling the temperature of the electronic part of $\Pi(\Omega)$ (red area) and the low-energy bosons (blue area).(c) The shape of $\Delta R/R(\omega)$ obtained by simulating the positive and negative variation of ω_p. In the inset we report the temporal profile of the temperatures variation at T=100 K, obtained by the three temperature model simulations.(d) The shape of $\Delta R/R(\omega)$ obtained by simulating the increasing and the lowering of the low-energy peak which appears in the $\Pi(\Omega)$ in pseudogap state (see the inset).

appearing in the bosonic spectrum at T=100K (see the inset of fig. 8.4a-b). The mode's intensity starts to rise at T=T* and it has been associated to an unusual long-range magnetic order in the pseudogap phase. This experimental finding constitutes an argument in favour of the hypothesis that the pseudogap phase is a new phase of the matter characterized by a given order parameter. Varma and coworkers describes this order in term of pairs of electron-current loops, flowing within the same unit cell, which give rise to pairs of oppositely directed magnetic moments [128]. The electronic nature of this peak is in accord with our differential fit because its variation occurs on an a fast time scale (<200 fs). Moreover the absence of structural changement in Bi2212 makes difficult to associate this mode to a new lattice excitation occuring in pseudogap phase.

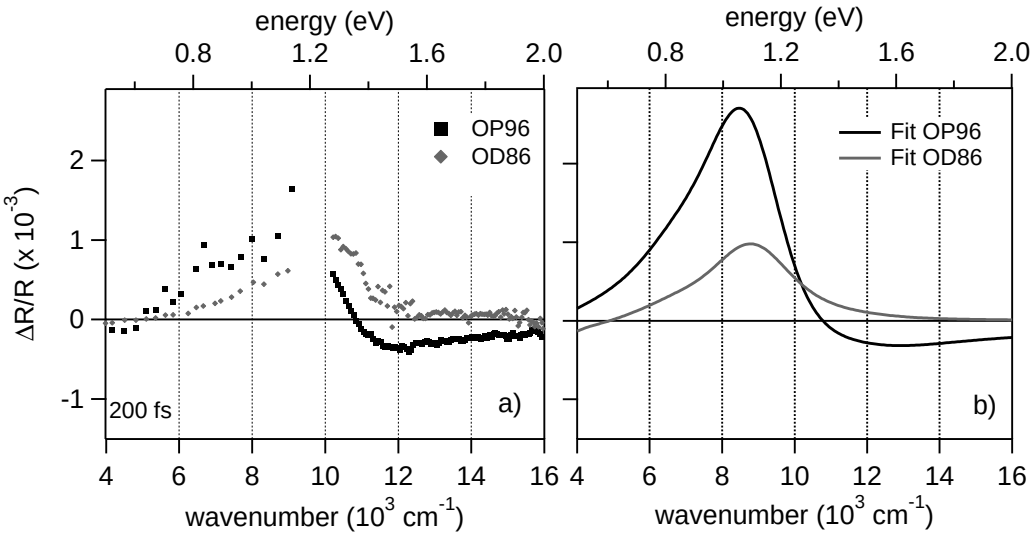

Figure 8.5: (a) Energy-resolved spectra taken at 200 fs of time delay on OP96 and OD86.(b) The best fit to the data with the differential dielectric function. The fit qualitatively reproduces the data assuming a transient increasing of ω_p and a weakening of the lowest-energy bosonic peak.

8.5 Conclusions

In conclusion the differential fit qualitatively reproduces the energy-resolved reflectivity spectra in pseudogap phase by assuming, beyond a simple variation of the electronic and bosonic temperatures, also a transient increasing of the Drude plasma frequency ω_p and a weakening of the low-energy bosonic mode. The positive variation of ω_p, opposite to the fit results obtained in normal state, could be explained in term of a pump induced closing of a gap above T_c which causes the decreasing of the carriers kinetic energy. This physical scenario seems to support the hypothesis according to which the pseudogap is a real gap in the density of states.
The electron-boson coupling function at T=100 K displays a new mode at ∼36 meV, close to the narrow peak centered at ∼70 meV, which could be related to the magnetic collective mode recently observed in inelastic neutron scattering measurements. The fit results indicates also a weakening of this bosonic mode showing that its appearance could be considered as an intrinsic feature of the pseudogap phase.

Chapter 9

Superconductive phase

9.1 Introduction

In this chapter we report time and frequency resolved reflectivity measurements on Y-doped Bi2212 in the superconductive phase at T=20 K. In this case, the system exhibits a structured response in the 1-2 eV range that can not be reproduced by modifying the extended Drude parameters as in normal and pseudogap phase but can be satisfactorily reproduced assuming a modification of the optical oscillators at 1.5 and 2 eV. The spectral weight variation related to these transitions accounts for the kinetic energy variation claimed by previous works based on equilibrium spectroscopies [15, 20, 70, 82, 90, 107, 108, 125].

9.2 Experimental data

In fig. (9.1) we report the time and frequency resolved reflectivity $\Delta R/R(\omega, t)$, between 1.25 eV and 2 eV, carried on the samples UD83, OP96 and OD86 in the superconductive state at T=20K. The energy resolved spectra at delay τ=0, reported on the right-hand side, show that $\Delta R/R$ behaviour is more structured as compared to the normal state response and strongly depends on the hole concentration. In UD83 the transient response is positive for all the energy range reaching $\sim 10^{-3}$ and drops at higher probe frequency. In OP96 a negative dip occurs in $\Delta R/R$ between 1.4 eV and 1.5 eV followed by a steep rise at lower energy. In OD86 the negative dip evolves becoming broadened and more intense. For each 2D plot, the time traces at λ_{probe}=800 nm are reported (white curves) and exactly reproduce the time-resolved reflectivities obtained in the standard single-colour configuration, i.e., with fixed probe wavelength [76]. As previously observed in one-color pump-probe reflectivity measurements, reported in chapter 6.3, the decay time of $\Delta R/R$ increases upon cooling the sample below T_c, changing from $\sim$350 fs to 3-5 ps. The sudden increase of the decay time is generally attributed to a bottleneck effect [62], the dynamics being dominated by the high-frequency bosons ($\hbar\Omega > 2\Delta$) emitted during the reformation of the Cooper pairs.
This dynamical process is phenomenologically described by the Rothwarf-Taylor model [106], as reported in detail in chapter 3.3.3.

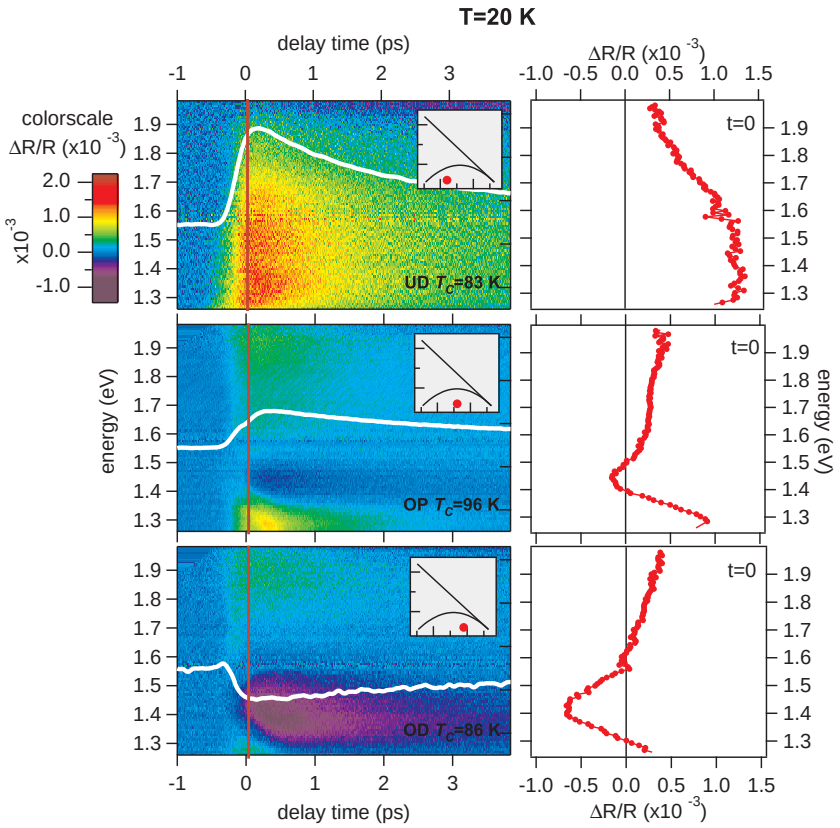

Figure 9.1: Energy and time-resolved reflectivity on $Bi_2Sr_2Ca_{0.92}Y_{0.08}Cu_2O_{8+\delta}$. The 2D scan are reported for different doping range at T=20K. The colour scale of the reflectivity variation amplitude is reported on the top left of the figure. The insets display the position of each scan in the T-δ phase diagram. The white lines are the $\Delta R/R(t)$ traces obtained at λ_{probe}=800nm. The red line represents the cut at the delay time τ=0 ps. The energy resolved spectra $\Delta R/R(\omega, \tau = 0)$ are reported next to the respective 2D plot.

Before studying the non-equilibrium dielectric function below T_c, we describe the recovery dynamics of a non-equilibrium electronic population. We can identify three different time-scales.
After being excited at 1.5 eV by the pump pulse, the electronic carriers thermalize on a fast timescale (0-50 fs) and through inelastic electron-electron scattering. The scattering rate, obtained through optical measurements, is roughly proportional to both the frequency and temperature, i.e., $\propto 1/\tau(\omega, T)$ [123]. At 1.5 eV energy, the frequency-dependent scattering rate is $\sim$4000 cm^{-1}, corresponding to a lifetime of $\sim$1 fs. In the first tens of femtoseconds, the non-equilibrium electrons lose energy through a cascade process and low-energy excitations are accumulated at the top of the gap. As the electronic excitations decrease their energy, the scattering rate proportionally decreases. The non-equilibrium population created within the pulse duration can be assumed as quasi-thermal, being described by an effective chemical potential (μ_{eff}) [99] or a temperature (T_{eff}) [100].

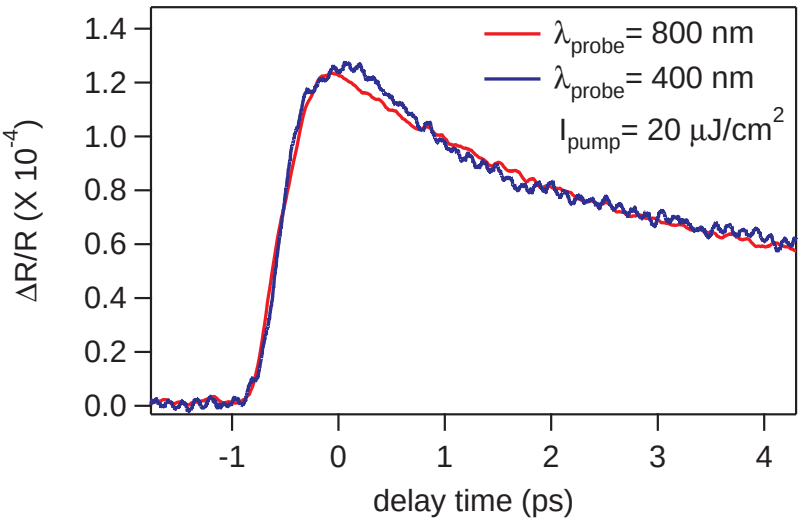

Figure 9.2: Differential reflectivity at different pump wavelength (λ_{pump}=800 nm and λ_{pump}=400 nm) at T=20 K in the low fluence regime (I_{pump}=20 $\frac{\mu J}{cm^2}$). The slowing down of the dynamics is observed at both the wavelengths and the decay time is nearly the same

In this frame, the photoinduced non-equilibrium population created during the pulse duration is independent of the particular pump photon energy. To test this prediction, we repeated the $\Delta R/R(\omega, t)$ measurements with a photon pump energy of 3.14 eV, obtaining the same results (see fig.9.2).
Moreover, from the measurements carried on in normal state, we found that the electron population, on this fast timescale, is strongly coupled with the electronic part of the boson spectrum. On a longer timescale, below 500 fs, the excited quasiparticles, exchange energy with the phonon population at the equilibrium temperature T_{eq}. The energy exchange can be related either to a direct inelastic scattering process between gap-energy excitations and phonons or to the selective emission of bosons during the recombination of the quasiparticles to reform Cooper pairs. On the sub-ps timescale the physical scenario is that of a non-equilibrium population of the quasiparticles thermalized with a subset of phononic modes at a temperature larger than T_{eq}. Above 500 fs, the subset of bosons strongly coupled to the quasiparticles, thermalizes with the phonon thermal reservoir through inelastic phonon-phonon scattering processes.
To wrap up, after approximately 500 fs, the excited electronic carriers are thermalized with both the bosons of electronic origin and the strongly coupled lattice modes. Further more, the indipendent variation of the electronic and bosonic temperatures on the 0-500 fs timescale, simulated in fig. 7.8a, significantly affects the measured time-resolved reflectivity only below 1.2 eV, i.e. the lower limit of the supercontinuum probe frequency range.
For this reason and to simplify the calculations, in the following we will fit the 1.2-2 eV time-resolved reflectivity at higher delays omitting the effects related to

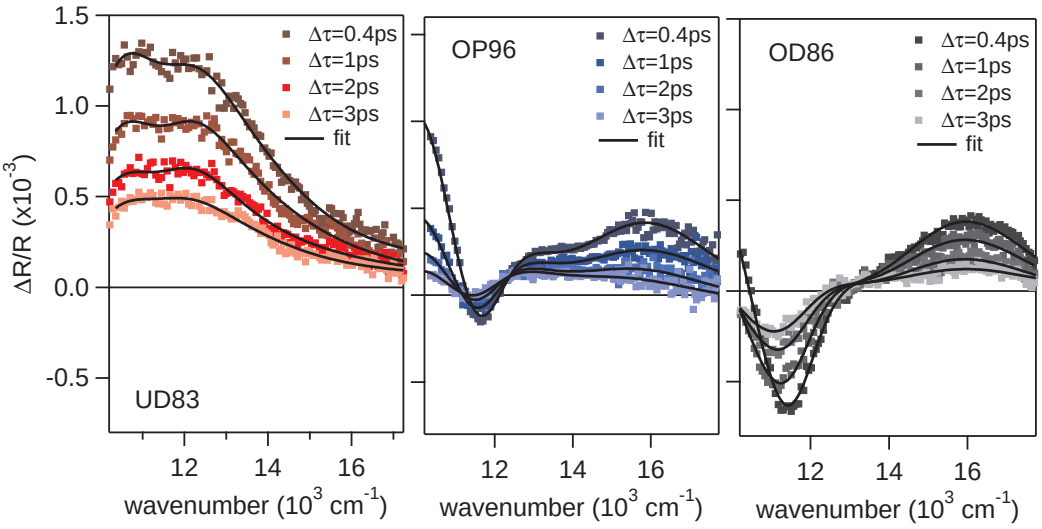

Figure 9.3: Energy-resolved spectra measured at different delay times. The black curves represent the best fit lines to the data assuming a transient modification of the 1.5 eV and 2 eV interband oscillators. The differential fit parameters related to the 0ps time-traces are reported in table 9.1.

the disentangling between T_e and T_b, and assuming a quasi-thermal variation of the temperature. As a consequence of this assumption, we use a differential model based on the so-called Allen approximation of the memory function (equation 3.5). In this case the fitting methods is faster than that used for the data in normal and pseudogap phase, because only one integration relates the boson coupling function and the memory function, and it is more effective to evidence possible modifications in the interband transitions.

9.3 Fitting results and discussion

In fig.9.3 we report the $\Delta R/R(\omega, t)$ measured in the superconducting phase in the 1.2-2.2 eV energy range at different delay times. As we can see the shape of the reflectivity variation is significantly different from the temperature-related broadening effect of the Drude peak which is characterized by a positive signal that monotonically decreases with the probe energy.
In order to reproduce the structured signal, it is necessary to change the parameters of the interband optical oscillator at 11800 cm^{-1} (1.46 eV) and 16163 cm^{-1} (2 eV) (ω_2 and ω_3 in the table 5.2). The conservation of the total spectral weight is guaranteed by the constraint that the sum of the squared plasma frequencies of the extended Drude model and of the interband oscillators is constant.
Moreover the fit to the data automatically satisfy the Kramers-Kronig (KK) relations, since they are obtained as a difference between KK-constrained Lorentz oscillators, and are used to calculate the relative variation of the optical conductivity ($\Delta\sigma_1/\sigma_1(\omega, t)$) shown in figure . The trend from positive $\Delta\sigma_1/\sigma_1(\omega, t)$ in the underdoped to a slightly negative $\Delta\sigma_1/\sigma_1(\omega, t)$ in the overdoped samples reveals that the

Table 9.1: Tables of the paramenters modified in the differential fit procedure related to the time delay traces at 0.4 ps. The impulsive variation of the fitted data are reported in fig.9.3

	parameters	UD83	OP96	OD86
Extended Drude	T (K)	38.6	38.8	41.3
Interband transition	ω_2 (cm^{-1})	11802	11799	11803
	ω_{p2}^2 (cm^{-2})	5.38e+06	5.68e+06	5.80e+06
	γ_2 (cm^{-1})	3657	3698	3689
	ω_3 (cm^{-1})	16160	16176	16177
	ω_{p3}^2 (cm^{-2})	3.93e+07	4.06e+07	4.18e+07
	γ_3 (cm^{-1})	8314	8283	8278

interband spectral weight variation ($\Delta SW_{tot} = \Delta\omega_p^2(1.5)/8 + \Delta\omega_p^2(2)/8$, $\omega_p(1.5)$ and $\omega_p(2)$ being the plasma frequencies of the 1.5 and 2 eV oscillators) strongly depends on the doping as we can clearly see in fig. 9.4.

In the simple energy-gap model for conventional superconductors, small changes of the interband transitions, over a narrow frequency range of the order of $\omega_{o,i} \pm \frac{\Delta}{\hbar}$, can arise from the opening of the superconducting gap at the Fermi level. In contrast to this model, these measurements clearly shows a photoinduced change of R(ω,t) over a spectral range ($\sim$1 eV), significantly broader than Δ $\sim$40 meV [135]. This result reveals a dramatic superconductivity-induced rearrangement of the mixed Cu-O electronic states extending from 1 eV to 2 eV binding energy.

In a time-resolved pump-probe experiment, carried on below T_c, the pump pulse effect is to break the Cooper pairs injecting a density of quasiparticle above 2Δ. Depending on the fluence of the pulse, this can result in a photoinduced phase transition to the normal state. In Y-doped Bi2212, a photo-induced phase transition was observed at $\sim 60\mu J/cm^2$ [50]. Since the working fluence of the experiment ($10\mu J/cm^2$) is well below this threshold, the effect of the pump is to impulsively increase the temperature of the system without inducing a transition to the normal state. In this way, the impulsive increase of the interband spectral weight ΔSW_{tot} observed in UD83 and OP96 corresponds to a reduction of ΔSW_{tot} upon lowering the temperature of the system. Since the spectral weight change of the charge transfer oscillators is compensated by an opposite change on the intraband spectral weight, this result suggests that the superconductivity, in this doping range, is accompanied by a reduction of the carriers kinetic energy.

As we move from the under to the overdoped side of the superconducting dome, our results point toward a scenario of a transition from a superconductivity-induced gain of kinetic energy, involving electronic states at 1.5-2 eV binding energy, to a BCS-like loss of kinetic energy, overcompensated by a gain in binding energy.

The results of the differential fitting procedure are very stable on the choice of the equilibrium dielectric function. The same results are obtained assuming a different

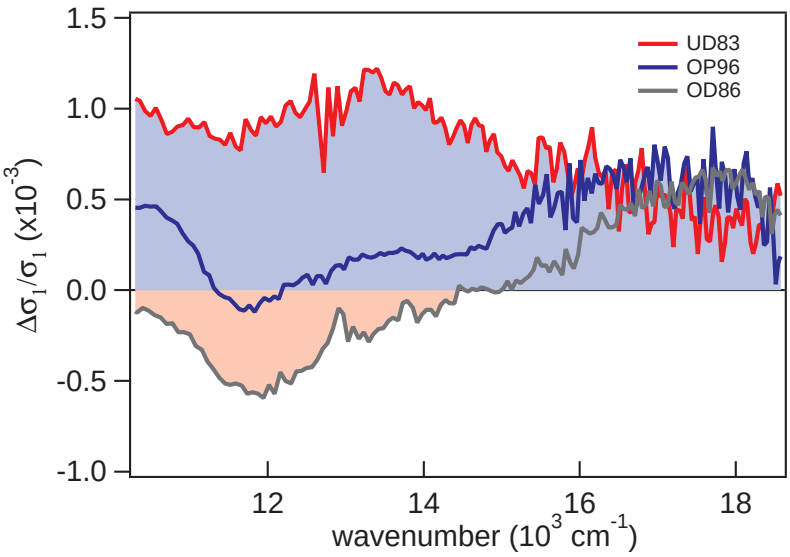

Figure 9.4: Relative variation of the optical conductivity, obtained from the Kramers-Kronig transformation of the fit at 0 ps delay time. The spectral weigth variation, obtained as the $\Delta\sigma/\sigma$ integral over the frequency range, changes from positive to negative with the increasing the doping rate.

$\epsilon_{eq}(\omega, t)$ (for example with a different number of interband oscillators). For this reason, the equilibrium dielectric function used can be considered as a "realistic" dielectric function, even if, possibly, not the best dielectric function one can get (since the procedure to obtain it is often questionable). In any case, the details of the equilibrium dielectric function do not alter the results of the differential analysis. In fig. 9.5, the error bars indicate the range of ΔSW_{tot} values that can be obtained starting form different $\epsilon_{eq}(\omega, t)$.
In table 9.1 we report the values assumed by the non-equilibrium dielectric function at a delay of 0.4 ps in order to obtain the best fit of the data. Fig. 9.6 shows the temporal dynamics of the total variation of spectral weight ΔSW_{tot} compared to the time evolution of the superconductive gap Δ. We can clearly see that the two dynamics display the same temporal dacay and the maximum value of ΔSW_{tot} corresponds to the minimum value of Δ after $\sim$400fs, i.e. when part of the boson has thermalized with the electronic carriers. This results suggests that the variation of the optical properties in the visible region is exclusively related to the impulsive suppression of Δ. At longer times (5 ps), when the complete electron-boson thermalization broadens the Drude peak, the ΔSW_{tot} variation is completely washed out.
A further confirmation of the strict relation between the partial photoinduced closing of the gap and the modification of the optical properties in the visible range comes from the temperature dependence of ΔSW_{tot} reported in fig. 9.7. In this case ΔSW_{tot} is estimated from the slow decay component of the one-color pump-probe measurements taken at the same fluence (i.e. 10 $\mu J/cm^2$) and results to vanish approaching T_c from below.

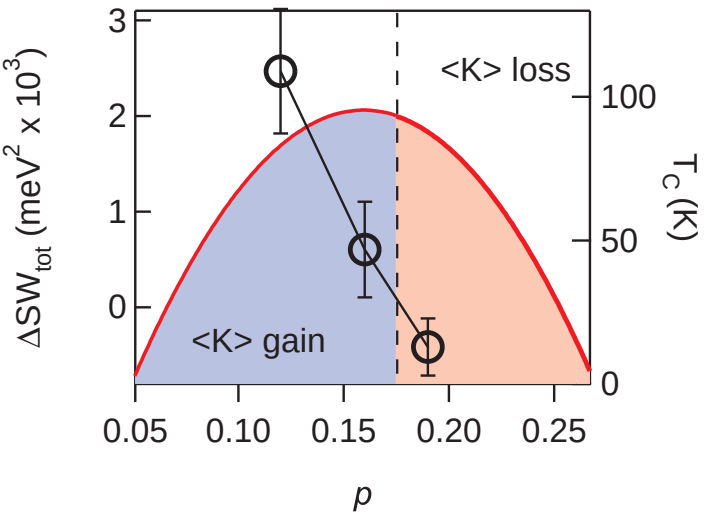

Figure 9.5: The black circles represent the maximum $\Delta SW_{tot} = \Delta\omega_p^2(1.5)/8 + \Delta\omega_p^2(2)/8$, observed at 400 fs, as a function of the doping level. The error bars take into account the stability of the differential fit on the equilibrium dielectric function.

9.3.1 Kinetic energy variation

In BCS system the superconductivity-induced appearance of the optical spectral weight at zero frequency is compensated by a decrease of the spectral weight of intraband transitions, as a consequence of the conservation of the electric charge. This physical result is expressed by the Ferrel-Glover-Tinkham sum rule. In HTSC, possible violations of this sum rules for the in-plane dielectric function have proposed and discussed [15, 53, 96, 90]. In this scenario possible spectral weight shift from/to the interband transitions has to be taken into account in a more general sum rule, reported in equation 3.14.
The total intraband spectral weight (including the zero-frequency condensate spectral weight) can be related to the kinetic energy T_δ of the charge carriers (holes) associated to hopping process in the δ direction, via the relation 3.15 that we report here [53]:

$$\frac{1}{4\pi}\int_0^\infty \omega\epsilon_D(\omega)\ d\omega = \frac{\pi^2 a_\delta^2 e^2}{2\hbar^2 V_{Cu}}\langle -T_\delta\rangle \tag{9.1}$$

where a_δ is the lattice spacing in the Cu-O plane, projected along the direction determined by the in-plane polarization δ of the incident light and V_{Cu} is the volume per Cu atom. We obtain $< K >= 2 < T_\delta >$ from the spectral weight variation of the interband oscillators, through the relation:

$$\langle K\rangle = 2\langle T_\delta\rangle = \frac{4\hbar^2 V_{Cu}}{\pi^2 a_\delta^2 e^2}\left[SW_h^N - SW_h^{SC}\right] \tag{9.2}$$

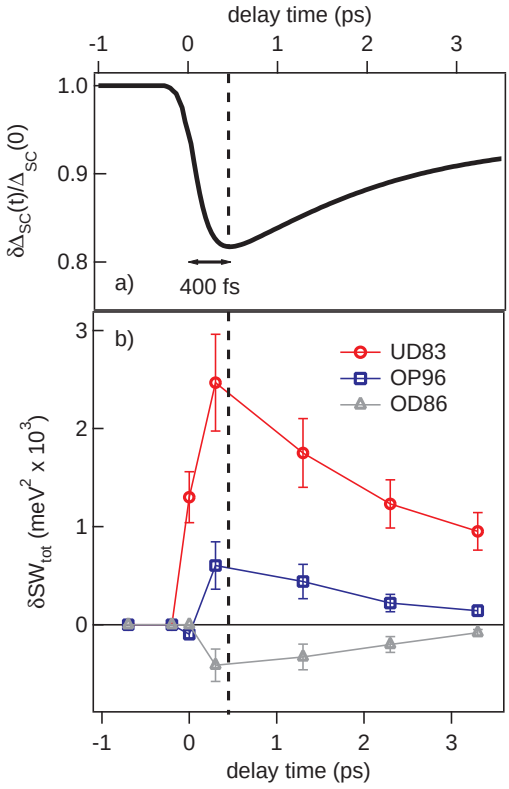

Figure 9.6: (a) The dynamics of the superconducting gap, assuming that $\Delta R/R(\omega, t)$ is proportional with the photoexcited quasiparticle density. At a pump fluence of 10 $\mu J/cm^2$, the maximum gap decrease is ∼20% at 400 fs delay time. (b) The spectral weigth variation at different delay times for the three dopings. The maximum value of ΔSW_{tot} corresponds to the minimum Δ value at ∼400 fs, i.e., after a partial electron-boson thermalization. The error bars represent the standard deviation obtained from the fit.

Considering V_{Cu}=$V_{unitcell}/8 \sim 1.1 \cdot 10^{-22} cm^3$ and a_δ=$a_{unitcell}/\sqrt{2}$ ∼3.9A, we obtain that the kinetic energy can be calculated as:

$$< K >= 8\hbar^2 \left[SW_h^N - SW_h^{SC}\right] \cdot (83 meV/eV^2), \tag{9.3}$$

where $8\hbar^2 \left[SW_h^N - SW_h^{SC}\right]$ is the interband spectral weight variation expressed in eV^2.

A finite value of $\left[SW_h^N - SW_h^{SC}\right]$ thus implies a superconductivity-induced variation of the kinetic energy.

Since the interband spectral weight variation $\Delta SW_{tot} = \Delta\omega_p^2(1.5)/8 + \Delta\omega_p^2(2)/8$ extracted from the differential fit corresponds to a given density of quasiparticles injected by the pump pulse, it is necessary to know the density of the broken Cooper pairs to give an estimation of $\left[SW_h^N - SW_h^{SC}\right]$. The density of photoinjected excitations can be roughly estimated considering the absorbed laser fluence of 10 $\mu J/cm^2$ per pulse, corresponding to an absorbed energy density of 0.6 J/cm^3, λ_d=160 nm being the penetration depth at 800 nm wavelength.

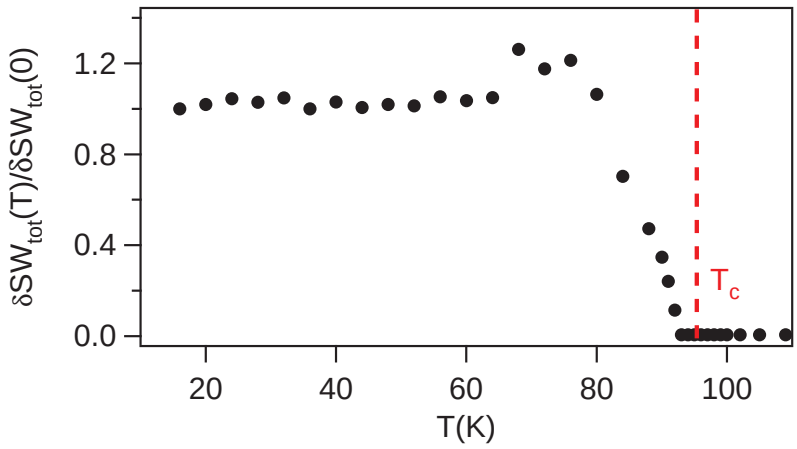

Figure 9.7: The ΔSW_{tot} value, relative to the extrapolated zero-temperature value, is estimated from single-colour measurements and reported as a function of the temperature for OP96. Similar results are obtained for UD83 and OD86.

Considering a volume per Cu atom of $1.13{\cdot}10^{-22}$ cm^3 and assuming that the number of gap-energy excitations produced by each 1.5 eV photon is approximately $\sim \frac{\hbar\omega}{2\Delta} = \frac{1.5\,eV}{0.04\,eV} \sim 40$, the density of broken Cooper pairs is $5.5{\cdot}10^{-3}$ per Cu atom. This value is about the 7% of the superfluid density in optimally-doped Bi2212 [56]. This estimation is too high because it does not take into account the d-wave character of the superconducting gap and the possibility that energy can be released to bosons before the complete electron thermalization [94].

A more precise calculation of the density of photoinjected excitations is based on a phenomenological approach. We take advantage of the upper limit in the photoexcitation density set by the photo-induced phase transition to the normal state reported at high pump fluence on HTSC [50, 69, 84]. This nonthermal phase transition has a first-order character and takes place at a finite superconducting gap value [Coslovich2010], as predicted by the μ_{eff} non-equilibrium superconductivity model [50, 94, 99]. In the Y-Bi2212 we observe a photo-induced phase transition at $\sim$60 $\mu J/cm^2$ [50, 27]. From numerical calculations, performed by Nicol*et al.* [94] within the μ_{eff} model, the instability of the superconducting state is predicted when 15-20% of Cooper pairs are broken. Extrapolating back to our working fluence (10 $\mu J/cm^2$), we can estimate the number of photo-excited Cooper pairs to be around 3%. The total kinetic energy variation $\left[SW_h^N - SW_h^{SC}\right]$ corresponding to the breaking of all the Cooper pairs, is determined from the experimental interband spectral weight variation ΔSW_{tot} and it turns to be $\sim$1-2meV/Cu for the underdoped sample.

This value is very close to the superconductivity-induced kinetic energy gain predicted by several unconventional models and estimated by standard spectroscopic techniques, integrating over all the high-energy spectral region.

9.3.2 Gap suppression

As we have anticipated in the previous section the superconductive gap is expected to exhibit strong variations in time, when the system is perturbed by an ultra-short laser pulse. Since the parameters of the RT model [106] can be affected by these varitions, we developed a time dependent model based on the RT equations [45]:

$$\begin{aligned} \dot{n} &= I_{QP}(t) + 2\gamma p - \beta n^2 \\ \dot{p} &= I_{Bos}(t) - \gamma p + \frac{\beta n^2}{2} - \gamma_{esc}(t)(p - p_T) \end{aligned} \tag{9.4}$$

In the phonon bottleneck regime ($\gamma > \gamma_{esc}$), the excitation relaxation is ultimately regulated by the escape rate of the non-equilibrium gap-energy phonons ($\gamma_{esc}(p-p_T)$) term, p_T being the thermal phonon density). The γ_{esc} value is determined both by the escape rate of the non-equilibrium phonons from the probed region and by the energy relaxation through inelastic scattering with the thermal phonons and is directly dependent on the superconducting gap value [45]. The time evolution of Δ can be obtained from the $\Delta R/R(t)$ time-traces at 800 nm probe wavelength, under the following assumptions:

- The $\Delta R/R(t)$ time-trace is assumed to be proportional to the solution n(t) of Eqs.9.4, in agreement with the literature [27, 50, 47, 48, 63, 62, 64, 69, 76].
- The time-dependent non-equilibrium superconducting gap $\Delta(n(t))$ can be expressed as a function of $n(t)$, considering the effective temperature (T_{eff}) and chemical potential (μ_{eff}) models [45, 50, 94, 99]. In both cases the normalized $\Delta(n(t))$ depends on $(1 - a \cdot n(t)^{3/2})$ (being a a conversion factor) for a d-wave gap symmetry [45, 94].
- While γ and β can be assumed as constant during the decay dynamics, $\gamma_{esc}(\Delta(n(t)))$ is the only time-dependent parameter.
- $\gamma_{esc}(t)$ quadratically depends on the instantaneous gap value, as demonstrated in Ref. [45], i.e. $\gamma_{esc}(t) = \gamma_{esc}(0) \cdot [\Delta(n(t))/\Delta(0)]^2$ being the γ_{esc} value corresponding to the unperturbed gap $\Delta(0)$.

Fitting the $\Delta R/R(t)$ time-traces, measured at 10 $\mu J/cm^2$ pump fluence, with the solution of Eqs.9.4 we are able to extract the instantaneous $\Delta(t)$ value, reported in fig. 9.6. The minimum gap value is obtained at t=400 fs delay and corresponds to ∼80% of $\Delta(0)$.

9.4 Conclusion

The differential dielectric function fitting procedure allows us to conclude that, as T_c is crossed, the $\Delta R/R(\omega, t)$ signal measured in the near IR/visible region is associated to a modification of the interband transitions, beyond a simple impulsive broadening of the Drude function. This conclusion holds for all the doping regimes investigated in the present measurements. These results finally shed light on the long-standing question [33] about the origin of the $\Delta R/R(t)$ measured in the one-colour time-resolved reflectivity experiment [63]. The measured signal is not originated by an

excited state absorption, related to the variation of the electronic distribution within the unvaried electronic bands, but to a real modification of the underlying electronic bands and, in particular, of the interband transitions at 1.5-2 eV. Nonetheless, the measured $\Delta R/R(\omega, t)$ is proportional to the density of photo-injected quasiparticles, as commonly assumed (see Ref. [69] and references therein).

Chapter 10

Conclusions

In this thesis work we study for the first time the temporal optical response of cuprates over a wide spectral region ranging from the visible to the near-infrared optical region. To achieve this result we exploit the supercontinuum coherent spectrum produced by a non-linear photonic crystal fiber and the tunable pulses provided by an optical parametric amplifier system as a probe. The time and frequency resolved reflectivity measurements we report and discuss, are carried on different $Bi_2Sr_2Ca_{0.92}Y_{0.08}Cu_2O_{8+\delta}$ crystals at three different dopings and temperatures. Due to its simultaneous high spectral and temporal resolution, this experimental technique is able to investigate the non-equilibrium dielectric function of the system.
Since the study of this physical quantity relies on the knowledge of the equilibrium dielectric function $\epsilon_{eq}(\omega)$, a great importance is given to find a model able to describes the optical properties of an HTSC.
In chapter four we report the reflectivity measurements carried on in the equilibrium condition. The extended Drude model and a sum of optical oscillator are successfully employed to reproduce $\epsilon_{eq}(\omega)$ in a broad spectral region. Moreover the electron-boson coupling function $\Pi(\Omega)$ is directly extracted from the data, following the same procedures described in [127]. The extracted glue function is characterized by a low-energy narrow peak, centered at $\sim$70 meV, whose origin is strongly debated and a broad continuum extending up to 300 meV which accounts for the strength of the coupling between the carriers and the other bosons of electronic origin.
The core of the thesis is given by the last three chapter where we study the recovery dynamics of the excited dielectric function respectively in normal, pseudogap and superconductive phases.

- In order to make a quantitatively study of the pump induced variation of the signal over the frequency window of interest at different delay times, we developed a differential model, which is described in detailed in chapter 7. Exploiting the possibility of this non-equilibrium approach to spectrally resolve and to disentangle the contribution of electronic and bosonic temperature, we obtain interesting results about the pairing mechanism in cuprates. In particular, focusing on the dynamics of $\Delta R/R(\omega)$ on an a fast time scale ($<$200 fs), we find that the carriers, after being excited by the laser pulse, thermalize istantly with the electronic part of $\Pi(\Omega)$. The differential fit results indicates

that, not only the high-energy part of $\Pi(\Omega)$, but also a fraction of the narrow peak have to be ascribed to the coupling with electronic bosons. The complete physical scenario, resulting by extending the probe photon spectral window, involves a sudden thermalization between electrons and bosonic modes which is followed, on a slower time scale, by the relaxation with the phonon modes (hot and cold phonons) according to the three temperature model [101]. In addition, using the strong-coupling formalism, we have determined the contribution to the critical temperature of the different part of $\Pi(\Omega)$. Our conclusion is that T_c is determined by the electronic coupling with both bosonic and phononic modes and the two mechanism alone are not sufficient to explain the superconductivity in cuprates.

- In the pseudogap state (chapter 8), the variation of reflectivity is totally different from the normal state behaviour. This drastic change can not be explained in term of an excited state absorption or an effect due to the different pump-induced heating, but it is an intrinsic response of the system. The differential analysis of the optical response seems to evidence a transient and positive variation of the Drude plasma frequency according to a possible gap closing effect. This result is in accord with the theory that the pseudogap consists in an effective spectral weight suppression of the density of states near the Fermi level E_F and it is consistent with a temperature dependent glue funtion [73].

- The superconductivity induced variation of reflectivity, reported in chapter 9, cannot be reproduced by simply modifying the extended Drude model parameters, as in normal and pseudogap phase. The structured signal measured below T_c can be fully accounted by assuming a modification of the optical oscillators at 1.5 and 2 eV, confirming that, in cuprates, the electronic structure close to E_F is strictly connected to that on a higher-energy scale and the opening of the superconductive gap is accompanied by a modification of the optical properties in the visible region.
  A reflectivity change in this spectral region was already observed in equilibrium optical measurements in term of a spectral weight transfer from the intraband to the interband optical region [90]. However the difficulty to resolve small signal variations and to set with precision the finite cutoff frequency necessary to evaluate the optical integral and the temperature-dependent narrowing of the Drude-like peak, prevented these techniques from addressing the major question whether the measured spectral weight variation is equally spread over all the interband transitions or related to particular electronic states participating in the condensate formation [96].
  These results are in accord with the theory of hole superconductivity proposed by Hirsch and Marsiglio [52]. According to that, in cuprates the carriers lower their kinetic energy upon pairing, contrary to the case of BCS superconductors where a lowering of the potential energy stabilizes the superconductive ground state. Moreover the superconductivity-induced decrease of the kinetic energy, estimated from our fit result, is $\sim$1-2 meV/Cu atom, in accord to that obtained by standard spectroscopic techniques integrating over all the high-energy spectral region.

In conclusion, we have applied a time and frequency resolved technique to investigate the excited state of a cuprate. This experimental technique has the advantage to combine both the temporal and spectral resolution with the sensitivity to the different phase of the system. For this reason, it constitutes a very powerful and promising tool to study the non-equilibrium physics of the strongly correlated systems. A further step to improve this technique consists in extending the probe spectral window. This could allow to study the optical response of such systems in the far infrared and terahertz region i.e. very close to the relevant energy scale in HTSC like the d-wave superconducting gap and pseudogap.

Bibliography

[1] A. Abanov, A. V. Chubukov, and J. Schmalian. Fingerprints of spin mediated pairing in cuprates. *J. Electron Spectrosc. Relat. Phenom.*, 117:129, 2001.

[2] R. R. Alfano and S. L. Shapiro. Emission in the Region 4000 to 7000 Via Four-Photon Coupling in Glass. *Phys. Rev. Lett.*, 24:584, 1970.

[3] J. W. Allen and J. C. Mikkelsen. Optical properties of CrSb, MnSb, NiSb, NiAs. *Phys. Rev. B*, 15:2952, 1977.

[4] P. B. Allen. Electron-phonon effects in the infrared properties of metals. *Phys. Rev. B*, 3:305, 1971.

[5] P. B. Allen. Theory of thermal relaxation of electrons in metals. *Phys. Rev. Lett.*, 59:1460, 1987.

[6] P. W. Anderson. The Resonating Valence Bond State in La_2CuO_4 and Superconductivity. *Science*, 235:1196, 1987.

[7] P. W. Anderson. Is There Glue in Cuprate Superconductors? *Science*, 316:1705, 2007.

[8] N. W. Ashcroft and N. D. Mermin. *Solid state physics.* Harcourt College Publishers, Orlando FL, 1976.

[9] J. Bardeen, L. N. Cooper, and J. R. Schrieffer. Microscopic Theory of Superconductivity. *Phys. Rev.*, 106:162, 1957.

[10] J. Bardeen, L. N. Cooper, and J. R. Schrieffer. Theory of Superconductivity. *Phys. Rev.*, 108:1175, 2008.

[11] D. N. Basov and T. Timusk. Electrodynamics of high-T_c superconductors. *Rev. Mod. Phys.*, 77:721, 2005.

[12] M. Bassi, P. Camagni, R. Rolli, G. Samoggia, F. Parmigiani, G. Dhalenne, and A. Revcolevschi. Optical absorption of $CuGeO_3$. *Phys. Rev. B*, 54, 1996.

[13] B. Batlogg, H. Y. Hwang, H. Takagi, R. J. Cava, H. L. Kao, and J. Kwo. Normal state phase diagram of $(La,Sr)_2CuO_4$ from charge and spin dynamics. *Physica C*, 130:235, 1994.

[14] J. G. Bednorz and K. A. Müller. Possible high T_c superconductivity in the Ba-La-Cu-O system. *Z. Phys. B: Condens. Matter*, 64:189, 1986.

[15] A. V. Boris, N. N. Kovaleva, O. V. Dolgov, T. Holden, C. T. Lin, B. Keimer, and C. Bernhard. In-plane spectral weight shift of charge carriers in $yba_2cu_3o_{6.9}$. *Science*, 304:708, 2004.

[16] N. B. Brookes, G. Ghiringhelli, O. Tjernberg, L. H. Tjeng, T. Mizokawa, T. W. Li, and A. A. Menovsky. Detection of Zhang-Rice Singlets Using Spin-Polarized Photoemission. *Phys. Rev. Lett.*, 87:237003, 2001.

[17] S. D. Brorson, A. Kazeroonian, D. W. Face, T. K. Cheng, G. L. Doll, M. S. Dresselhaus, G. Dresselhaus, E. P. Ippen, T. Venkatesan, X. D. Wu, and A. Inam. Femtosecond thermomodulation study of high-t_c superconductors. *Solid State Commun.*, 74:1305, 1990.

[18] S. D. Brorson, A. Kazeroonian, J. S. Moodera, D. W. Face, T. K. Cheng, E. P. Ippen, M. S. Dresselhaus, and G. Dresselhaus. Femtosecond room-temperature measurement of the electron-phonon coupling constant γ in metallic superconductors. *Phys. Rev. Lett.*, 64:2172, 1990.

[19] F. Carbone, D.-S. Yang andE. Giannini, and A. H. Zewail. Direct role of structural dynamics in electron-lattice coupling of superconducting cuprates. *Proc. Natl. Acad. Sci.*, 105:20161, 2008.

[20] F. Carbone, A. B. Kuzmenko, H. J. A. Molegraaf, E. van Heumen, V. Lukovac, F. Marsiglio, and D. van der Marel. Doping dependence of the redistribution of optical spectral weight in $Bi_2Sr_2CaCu_2O_{8+\delta}$. *Phys. Rev. B*, 74:064510, 2006.

[21] C. Castellani, C. Di Castro, and M. Grilli. *Z. Phys*, 130:137, 1997.

[22] R. J. Cava. Oxide superconductors. *J. Am. Ceram. Soc.*, 83:5, 2000.

[23] S. Chakravarty, R. B. Laughlin, D. K. Morr, and C. Nayak. Hidden order in the cuprates. *Phys. Rev. B*, 63:094503, 2001.

[24] A. V. Chubukov and J Schmalian. Superconductivity due to massless boson exchange in the strong-coupling limit. *Phys. Rev. B*, 72:174520, 2005.

[25] F. Cilento, C. Giannetti, G. Ferrini, S. Dal Conte, T. Sala, G. Coslovich, M. Rini, A. Cavalleri, and F. Parmigiani. Ultrafast insulator-to-metal phase transition as a switch to measure the spectrogram of a supercontinuum light pulse. *Appl. Phys. Lett.*, 96:021102, 2010.

[26] L. N. Cooper. Bound Electron Pairs in a Degenerate Fermi Gas. *Phys. Rev.*, 104:1411, 1956.

[27] G. Coslovich, C. Giannetti, F. Cilento, G. Ferrini, and F.Parmigiani. Quasiparticles dynamics in underdoped Bi2212 under strong optical perturbation. *AIP proceedings*, 1162:177, 2009.

[28] T. Cuk, F. Baumberger, D. H. Lu, N. Ingle, X. J. Zhou, H. Eisaki, N. Kaneko, Z. Hussain, T. P. Devereaux, N. Nagaosa, and Z.-X. Shen. Coupling of the B_{1g} Phonon to the Antinodal Electronic States of $Bi_2Sr_2Ca_{0.92}Y_{0.08}Cu_2O_{8+\delta}$. *Phys. Rev. Lett.*, 93:117003, 2004.

[29] T. Cuk, D. H. Lu, X. J. Zhou, Z.-X. Shen, T. P. Devereaux, and N. Nagaosa. A review of electronphonon coupling seen in the high-T_c superconductors by angle-resolved photoemission studies (ARPES). *phys. stat. sol. (b)*, 242:11, 2005.

[30] E. Dagotto. Correlated electrons in high-temperature superconductors. *Rev. Mod. Phys.*, 66:763, 1994.

[31] A. Damascelli, Z. Hussain, and Z.-X. Shen. Angle-resolved photoemission studies of the cuprate superconductors. *Rev. Mod. Phys.*, 75:473, 2003.

[32] L. de Medici, X. Wang, M. Capone, and A. J. Millis. Correlation strength, gaps, and particle-hole asymmetry in high-T_c cuprates: A dynamical mean field study of the three-band copper-oxide model. *Phys. Rev. B*, 77:014518, 2009.

[33] J. Demsar, R. A. Averitt, V. V. Kabanov, and D. Mihailovic. Comment on Photoinduced Changes of Reflectivity in Single Crystals of $YBa_2Cu_3O_{6.5}$ (Ortho II). *Phys. Rev. Lett.*, 91:169701, 2003.

[34] J. Demsar, B. Podobnik, V. V. Kabanov, T. Wolf, and D. Mihailovic. Superconducting Gap Δ_c, the Pseudogap Δ_p, and Pair Fluctuations above T_c in Overdoped $Y_{1-x}Ca_xBa_2Cu_3O_{7-\delta}$ from Femtosecond Time-Domain Spectroscopy. *Phys. Rev. Lett.*, 82:4918, 1999.

[35] J. Demsar, J. L. Sarrao, and A. J. Taylor. Dynamics of photoexcited quasiparticles in heavy electron compounds. *J. Phys.:Condens. Matter*, 18, 2006.

[36] T. P. Devereaux, T. Cuk, Z.-X. Shen, and N. Nagaosa. Anisotropic Electron-Phonon Interaction in the Cuprates. *Phys. Rev. Lett.*, 93:117003, 2004.

[37] M. Dressel and G. Grunner. *Electrodynamics of solids: optical properties of electrons in matter*. Cambridge University Press, Cambridge, 2002.

[38] J. M. Dudley, G. Genty, and S. Coen. Supercontinuum generation in photonic crystal fiber. *Rev. Mod. Phys.*, 78:1135, 2006.

[39] H. Eisaki, N. Kaneko, D. L. Feng, A. Damascelli, P. K. Mang, K. M. Shen, Z.-X. Shen, and M. Greven. Effect of chemical inhomogeneity in bismuth-based copper oxide superconductors. *Phys. Rev. B*, 69:064512, 2004.

[40] G. M. Eliashberg. *Sov. Phys. JEPT*, 11:696, 1960.

[41] V. J. Emery. Theory of high-Tc superconductivity in oxides. *Phys. Rev. Lett.*, 58:2794, 1987.

[42] V. J. Emery and S. A. Kivelson. Importance of phase fluctuation in superconductors with small superfluid density. *Nature*, 374:4347, 1995.

[43] V. J. Emery, S. A. Kivelson, and O. Zachar. Spin-gap proximity effect mechanism of high-temperature superconductivity. *Phys. Rev. B*, 56:6120, 1997.

[44] M. Eschrig and M. R. Norman. Neutron Resonance: Modeling Photoemission and Tunneling Data in the Superconducting State of $Bi_2Sr_2CaCu_2O_{8+\delta}$. *Phys. Rev. Lett.*, 85:3261, 2000.

[45] G. Coslovich et al. *to be published on ArXiv.*

[46] D. Fournier, G. Levy, Y. Pennec, J.L. McChesney, A. Bostwick, E. Rotenberg, R. Liang, W.N. Hardy, D.A. Bonn, I.S. Elfimov, and A. Damascelli. Loss of nodal quasiparticle integrity in underdoped $YBa_2Cu_3O_{6+x}$. *ArXive*, 10074027.

[47] N. Gedik, P. Blake, R. C. Spitzer, J. Orenstein, R. Liang, D. A. Bonn, and W. N. Hardy. Single-quasiparticle stability and quasiparticle-pair decay in $YBa_2Cu_3O_{6.5}$. *Phys. Rev. B*, 70:014504, 2004.

[48] N. Gedik, M. Langner, J. Orenstein, S. Ono, Y. Abe, and Y. Ando. Abrupt Transition in Quasiparticle Dynamics at Optimal Doping in a Cuprate Superconductor System. *Phys. Rev. Lett.*, 95:117005, 2005.

[49] N. Gedik, J. Orenstein, R. Liang, D. A. Bonn, and W. N. Hardy. Gedik *et al.* Reply:. *Phys. Rev. Lett.*, 91:169702, 2003.

[50] C. Giannetti, G. Coslovich, F. Cilento, G. Ferrini, H. Eisaki, N. Kaneko, M. Greven, and F. Parmigiani. Discontinuity of the ultrafast electronic response of underdoped superconducting $Bi_2Sr_2CaCu_2O_{8+\delta}$ strongly excited by ultrashort light pulses. *Phys. Rev. B*, 79:224502, 2009.

[51] J. E. Hirsch. The True Colors of Cuprates. *Science*, 295.

[52] J. E. Hirsch and F. Marsiglio. Superconducting state in an oxygen hole metal. *Phys. Rev. B*, 39:11515, 1989.

[53] J. E. Hirsch and F. Marsiglio. Optical sum rule violation, superfluid weight, and condensation energy in the cuprates. *Phys. Rev. B*, 62:15131, 2000.

[54] J. Hohlfeld, S.-S. Wellershoff, J. Güdde, U. Conrad, V. Jähnke, and E. Matthias. Electron and lattice dynamics following optical excitation of metals. *Chem. Phys.*, 251:237, 2000.

[55] S. Hüfner, M. A. Hossain, A. Damascelli, and G. A. Sawatzky. Two gaps make a high-temperature superconductor? *Rep. Prog. Phys*, 71:062501, 2008.

[56] J. Hwang, T. Timusk, and G. D. Gu. Doping dependent optical properties of $Bi_2Sr_2CaCu_2O_{8+\delta}$. *J. Phys.:Condens. Matter*, 19:125208, 2007.

[57] J. Hwang, T. Timusk, and G. D. Gu. High-transition-temperature superconductivity in the absence of the magnetic-resonance mode. *Nature*, 427:714, 2007.

[58] J. Hwang, T. Timusk, E. Schachinger, and J. P. Carbotte. Evolution of the bosonic spectral density of the high-temperature superconductor $bi_2sr_2cacu_2o_{8+\delta}$. *Phys. Rev. B*, 75:144508, 2007.

[59] M. Imada, A. Fujimori, and Y. Tokura. Metal-insulator transition. *Rev. Mod. Phys.*, 70:1039, 1998.

[60] S. Ishihara and N. Nagaosa. Interplay of electron-phonon interaction and electron correlation in high-temperature superconductivity. *Phys. Rev. B*, 69:144520, 2004.

[61] S. Ishihara and N. Nagaosa. Electronphonon interaction in correlated cuprate superconductors. *J. Phys. Chem. Sol.*, 67:154, 2006.

[62] V. V. Kabanov, J. Demsar, and D. Mihailovic. Kinetics of a Superconductor Excited with a Femtosecond Optical Pulse. *Phys. Rev. Lett.*, 95:147002, 2005.

[63] V. V. Kabanov, J. Demsar, B. Podobnik, and D. Mihailovic. Quasiparticle relaxation dynamics in superconductors with different gap structures: Theory and experiments on $YBa_2Cu_3O_{7-\delta}$. *Phys. Rev. B*, 59:1497, 1999.

[64] R. A. Kaindl, M. A. Carnahan, D. S. Chemla, S. Oh, and J. N. Eckstein. Dynamics of Cooper pair formation in $Bi_2Sr_2CaCu_2O_{8+\delta}$. *Phys. Rev. B.*

[65] A. Kaminski, H. M. Fretwell, M. R. Norman, M. Randeria, S. Rosenkranz, U. Chatterjee, J. C. Campuzano, J. Mesot, T. Sato, T. Takahashi, T. Terashima, M. Takano, K. Kadowaki, Z. Z. Li, and H. Raffy. Momentum anisotropy of the scattering rate in cuprate superconductors. *Chem. Phys.*, 71:014517, 2005.

[66] A. E. Karakozov, E. G. Maksimov, and O. V. Dolgov. *Solid State Commun.*, 124:119, 2002.

[67] H. J. Kaufmann, E. G. Maksimov, and E. K. H. Salje. Electron-Phonon Interaction and Optical Spectra of Metals. *J. Supercond*, 22:755, 1998.

[68] M. L. Kulic and O. V. Dolgov. Forward scattering peak in the electronphonon interaction and impurity scattering of cuprate superconductors. *phys. stat. sol. (b)*, 242:151, 2005.

[69] P. Kusar, V.V. Kabanov, J. Demsar, T. Mertelj, S. Sugai, and D. Mihailovic. Controlled Vaporization of the Superconducting Condensate in Cuprate Superconductors by Femtosecond Photoexcitation. *Phys. Rev. Lett.*, 101:227001, 2008.

[70] A. B. Kuzmenko, H. J. A. Molegraaf, F. Carbone, and D. van der Marel. Temperature-modulation analysis of superconductivity-induced transfer of in-plane spectral weight in $bi_2sr_2cacu_2o_8$. *Phys. Rev. B*, 72:144503, 2005.

[71] A. Lanzara, P. V. Bogdanov, X. J. Zhou, S. A. Kellar, D. L. Feng, E. D. Lu, T. Yoshida, H. Eisaki, A. Fujimori, K. Kishio, J.-I. Shimoyama, T. Nodak, S. Uchidak, Z. Hussain, and Z.-X. Shen. Evidence for ubiquitous strong electron-phonon coupling in high-temperature superconductors. *Nature*, 412:510, 2001.

[72] P. A. Lee, N. Nagaosa, and X. G. Wen. Doping a Mott insulator: Physics of high-temperature superconductivity. *Rev. Mod. Phys.*, 78:17, 2006.

[73] Yuan Li, V. Balédent, G. Yu, N. Barišic, K. Hradil, R. A. Mole, Y. Sidis, P. Steffens, X. Zhao, P. Bourges, and M. Greven. Hidden magnetic excitation in the pseudogap phase of a high-T_c superconductor. *Nature*, 468:283, 2010.

[74] N. Lin, E. Gull, and A. J. Millis. Optical conductivity from cluster dynamical mean-field theory: Formalism and application to high-temperature superconductors. *Phys. Rev. B*, 80:161105.

[75] W.A. Little, M.J. Holcomb, G. Ghiringhelli, L. Braicovich, C. Dallera, A. Piazzalunga, A. Tagliaferri, and N.B. Brookes. A determination of the pairing interaction in the high-T_c cuprate superconductor $Tl_2Ba_2CaCu_2O_8$ (Tl2212). *Physica C*, 460:40, 2007.

[76] Y. H. Liu, Y. Toda, K. Shimatake, N. Momono, and M. Odaand M. Ido. Direct Observation of the Coexistence of the Pseudogap and Superconducting Quasiparticles in $Bi_2Sr_2CaCu_2O_{8+y}$ by Time-Resolved Optical Spectroscopy. *Phys. Rev. Lett.*, 101:137003, 2008.

[77] J. W. Loram, J. L. Luo, J. R. Cooper, W. Y. Liang, and J. L. Tallon. The Condensation Energy and Pseudogap Energy Scale of Bi2212 from the Electronic Specific Heat. *Physica C*, 341.

[78] J. W. Loram, K. A. Mirza, J. R. Cooper, and J. L. Tallon. Specific heat evidence on the normal state pseudogap. *J. Phys. Chem. Sol.*, 59:2091, 1998.

[79] H. Maeda, Y. Tanaka, M. Fukutumi, and T. Asano. A New High-T_c Oxide Superconductor without a Rare Earth Element. *Jpn. J. Appl. Phys., Part 2*, 27:209, 1988.

[80] E. G. Maksimov. High-temperature superconductivity: the current state. *Physics Uspekhi*, 43:965, 2000.

[81] F. Marsiglio. Inversion of Optical Conductivity Data in Metals. *J. Supercond*, 12:163, 1999.

[82] F. Marsiglio, F. Carbone, A. B. Kuzmenko, and D. van der Marel. Intraband optical spectral weight in the presence of a van hove singularity: Application to $bi_2sr_2cacu_2o_8$. *Phys. Rev. Lett.*, 74:174516, 2006.

[83] F. Marsiglio and J. E. Hirsch. Hole superconductivity and the high-T_c oxides. *Phys. Rev. B*, 41:6435, 1990.

[84] T. Mertelj, V. V. Kabanov, C. Gadermaier, N. D. Zhigadlo, S. Katrych, J. Karpinski, and D. Mihailovic. Distinct Pseudogap and Quasiparticle Relaxation Dynamics in the Superconducting State of Nearly Optimally Doped $SmFeAs_{0.08}F_{0.2}$ Single Crystals. *Phys. Rev. Lett.*, 102:117002, 2009.

[85] A. Migdal. *Sov. Phys. JEPT*, 7:996, 1957.

[86] W. L. Mc Millan and J. M. Rowell. Lead Phonon Spectrum Calculated from Superconducting Density of States. *Phys. Rev. Lett.*, 14:108, 1965.

[87] A. J. Millis, H. Monien, and D. Pines. Phenomenological model of nuclear relaxation in the normal state of $YBa_2Cu_3O_7$. *Phys. Rev. B*, 42:167, 1990.

[88] A. S. Mishchenko. Manifestation of the Electron-Phonon Coupling in the Spectroscopy of High-Temperature Superconductors. *J. Phys. Chem. Sol.*

[89] N. Miyakawa, P. Guptasarma, J. F. Zasadzinski, D. G. Hinksand, and K. E. Gray. Strong dependence of the superconducting gap on oxygen doping from tunneling measurements on $Bi_2Sr_2CaCu_2O_{8+\delta}$. *Phys. Rev. Lett.*, 80:157, 1998.

[90] H. J. A. Molegraaf, C. Presura, D. van der Marel, P. H. Kes, and M. Li. Superconductivity-Induced Transfer of In-Plane Spectral Weight in $Bi_2Sr_2CaCu_2O_{8+\delta}$. *Science*, 295:2239, 2002.

[91] H. Monien, P. Monthoux, and D. Pines. Phenomenological model of nuclear relaxation in the normal state of $YBa_2Cu_3O_7$. *Phys. Rev. B*, 43:275, 1991.

[92] N. Nagaosa and P. A. Lee. Ginzburg-Landau theory of the spin-charge-separated system. *Phys. Rev. B*, 45:966, 1992.

[93] Y. Nambu. Quasi-Particles and Gauge Invariance in the Theory of Superconductivity. *Phys. Rev.*, 117:648, 1960.

[94] E. J. Nicol and J. P. Carbotte. Comparison of s- and d-wave gap symmetry in nonequilibrium superconductivity. *Phys. Rev. B*, 67:214506, 2003.

[95] M. R. Norman, , D. Pines, and C. Kallin. The pseudogap: friend or foe of high T_c? *Adv. Phys*, 54:715, 2005.

[96] M. R. Norman, A. V. Chubukov, E. van Heumen, A. B. Kuzmenko, and D. van der Marel. Optical integral in the cuprates and the question of sum-rule violation. *Phys. Rev. B*, 76:220509.

[97] M. R. Norman and H. Ding. Collective modes and the superconducting-state spectral function of $Bi_2Sr_2CaCu_2O_8$. *Phys. Rev. B*, 57, 1998.

[98] M. R. Norman and C. Pepin. The Electronic Nature of High Temperature Cuprate Superconductors. *Rep. Prog. Phys*, 66:1547, 2003.

[99] C. S. Owen and D. J. Scalapino. Quantum critical behaviour in a high-T_c superconductor. *Phys. Rev. Lett.*, 28:1559, 1972.

[100] W. H. Parker. Modified heating theory of nonequilibrium superconductors. *Phys. Rev. B*, 12:3667, 1975.

[101] L. Perfetti, P. A. Loukakos, M. Lisowski, U. Bovensiepen, H. Eisaki, and M. Wolf. Ultrafast Electron Relaxation in Superconducting $Bi_2Sr_2CaCu_2O_{8+\delta}$ by Time-Resolved Photoelectron Spectroscopy. *Phys. Rev. Lett.*, 99:197001, 2007.

[102] P. Phillips. Identifying the propagating charge modes in doped Mott insulators. *Rev. Mod. Phys.*, 82:1719, 2010.

[103] W. E. Pickett. Electronic structure of the high-temperature oxide superconductors. *Rev. Mod. Phys.*, 61:433, 1989.

[104] M. Presland, J. Tallon, R. Buckley, R. Liu, and N. Flower. General trends in oxygen stoichiometry effects on T_c in Bi and Tl superconductors. *Physica C*, 176:95, 1991.

[105] A. V. Puchkov, P. Fournier, D. N. Basov, T. Timusk, A. Kapitulnik, and N. N. Kolesnikov. Evolution of the pseudogap state of high-t_c superconductors with doping. *Phys. Rev. Lett.*, 77:3212, 1996.

[106] A. Rothwarf and B. N. Taylor. Measurements of recombination lifetimes in superconductors. *Phys. Rev. Lett.*, 19:27, 1967.

[107] A. F. Santander-Syro, R. P. S. Lobo, N. Bontemps, Z. Konstatinovic, Z. Z. Li, and H. Raffy. Pairing in cuprates from high-energy electronic states. *Europhys. Lett.*, 62:568, 2003.

[108] A. F. Santander-Syro, R. P. S. M. Lobo, N. Bontemps, W. Lopera, D. Giratá, Z. Konstantinovic, Z. Z. Li, and H. Raffy. In-plane electrodynamics of the superconductivity in $Bi_2Sr_2CaCu_2O_8$: Energy scales and spectral weight distribution. *Phys. Rev. B*, 70:134504, 2004.

[109] D. J. Scalapino, E. Loh, and J. E. Hirsch. d-wave pairing near a spin-density-wave instability. *Phys. Rev. B*, 34:8190, 1986.

[110] G. P. Segre, N. Gedik, J. Orenstein, D. A. Bonn, R. Liang, and W. N. Hardy. Photoinduced Changes of Reflectivity in Single Crystals of $YBa_2Cu_3O_{6.5}$ (Ortho II). *Phys. Rev. Lett.*, 82:3054, 2002.

[111] Z.-X. Shen, D. S. Dessau, B. O. Wells, D. M. King, W. E. Spicer, A. J. Arko, D. Marshall, L. W. Lombardo, A. Kapitulnik, P. Dickinson, S. Doniach, J. DiCarlo, T. Loeser, and C. H. Park. Anomalously large gap anisotropy in the a-b plane of $bi_2sr_2cacu_2o_{8+\delta}$. *Phys. Rev. Lett.*, 5:1553, 1993.

[112] S.V. Shulga, O. V. Dolgov, and E. G. Maksimov. Electronic states and optical spectra of HTSC with electron-phonon coupling. *Physica C*, 178:266, 1991.

[113] M. R. Singh and S. B. Barrie. Magnon Specific Heat in Quasi-Two-Dimensional Antiferromagnetic Materials: Application to $YBa_2Cu_3O_6$ and La_2CuO_4 Oxide Superconductors. *phys. stat. sol. (b)*, 205:611, 1998.

[114] S. Tajima, T. Ido, S. Ishibashi, T. Itoh, H. Eisaki, Y. Mizuo, T. Arima, H. Takagi, and S. Uchida. Optical-phonon study of single crystals of various layered cuprates and related materials: Evidence of unique electron-phonon coupling in the CuO_2 plane. *Phys. Rev. B*, 43:10496, 1991.

[115] K. Tanaka, W. S. Lee, D. H. Lu, A. Fujimori, T. Fujii, Risdiana I. Terasaki, D. J. Scalapino, T. P. Devereaux, Z. Hussain, and Z.-X. Shen. Distinct Fermi-Momentum-Dependent Energy Gaps in Deeply Underdoped Bi2212. *Science*, 314:1910, 2006.

[116] H. J. Tao, F. Lu, and E. J. Wolf. Observation of pseudogap in $Bi_2Sr_2CaCu_2O_{8+\delta}$ single crystals with electron tunneling spectroscopy. *Physica C*, 282:1507, 1997.

[117] T. Timusk and B. Statt. The pseudogap in high-temperature superconductors: an experimental survey. *Rep. Prog. Phys*, 62:61, 1999.

[118] M. Tinkham. *Introduction to superconductivity.* McGraw-Hill, New York, 1975.

[119] Y. Tokura and T. Arima. New Classification Method for Layered Copper-Oxide Compounds and its Application to Design of New High-T_c Superconductors. *Jpn. J. Appl. Phys., Part 1*, 29:2488, 1990.

[120] A. Toschi and M. Capone. Optical sum rule anomalies in the cuprates: Interplay between strong correlation and electronic band structure. *Phys. Rev. B*, 77:014518, 2008.

[121] C. C. Tsuei and J. R. Kirtley. Pairing symmetry in cuprate superconductors. *Rev. Mod. Phys.*, 72:969, 2000.

[122] T. Valla, A. V. Fedorov, J. Lee, J. C. Davis, and G. D. Gu. The ground state of the pseudogap in cuprate superconductors. *Science*, 314:1914, 2006.

[123] D. van der Marel, H. J. A. Molegraaf, J. Zaanen, Z. Nussinov, F. Carbone, A. Damascelli, H. Eisaki, M. Greven, P. H. Kes, and M. Li. Quantum critical behaviour in a high-T_c superconductor. *Nature*, 425:271, 2003.

[124] E. van Heumen, A. B. Kuzmenko, and D. van der Marel. Optics clues to pairing glues in high-T_c cuprates. *J.Phys.:Conf.Ser*, 150:052278, 2009.

[125] E. van Heumen, R. Lortz, A. B. Kuzmenko, F. Carbone, D. van der Marel, X. Zhao, G. Yu, Y. Cho, N. Barisic, M. Greven, C.C. Homes, and S. V. Dordevic. Optical and thermodynamic properties of the high-temperature superconductor $HgBa_2CuO_{4+\delta}$. *Phys. Rev. B*, 75:054522, 2007.

[126] E. van Heumen, W. Meevasana, A. B. Kuzmenko, H. Eisaki, and D. van der Marel. Doping-dependent optical properties of Bi2201. *New J. Phys.*, 11:055067, 2009.

[127] E. van Heumen, E. Muhlethaler, A. B. Kuzmenko, H. Eisaki, W. Meevasana, M. Greven, and D. van der Marel. Optical determination of the relation between the electron-boson coupling function and the critical temperature in high-T_c cuprates. *Phys. Rev. B*, 79:184512, 2009.

[128] C. Varma. High-temperature superconductivity: Mind the pseudogap. *Nature*, 468:184, 2010.

[129] C. M. Varma. Pseudogap Phase and the Quantum-Critical Point in Copper-Oxide Metals. *Phys. Rev. Lett.*, 83:3538, 1999.

[130] C. M. Varma, P. B. Littlewood, S. Schmitt-Rink, E. Abrahams, and A. E. Ruckenstein. Phenomenology of the normal state of Cu-O high-temperature superconductors. *Phys. Rev. Lett.*, 63:1996, 2006.

[131] C. M. Varma, S. Schmitt-Rink, and E. Abrahams. Charge transfer excitations and superconductivity in ionic metals. *Solid State Commun.*, 62:681, 1987.

[132] B. Vignolle, S. M. Hayden, D. F. McMorrow, H. M. Ronnow, B. Lake, C. D. Frost, and T. G. Perring. Two energy scales in the spin excitations of the high-temperature superconductor $La_{2-x}Sr_xCuO_4$. *Nature Physics*, 3:163, 2007.

[133] F. Wooten. *Optical properties of solids.* Academic Press, New-York, 1972.

[134] K. M. Wu, J. R. Ashburn, and C. J. Torng. Superconductivity at 93 K in a new mixed-phase Y-Ba-Cu-O compound system at ambient pressure. *Phys. Rev. Lett.*, 58:908, 1987.

[135] G. Yu, E. M. Motoyama, and M. Greven. A universal relationship between magnetic resonance and superconducting gap in unconventional superconductors. *Nature Physics*, 5:873, 2009.

[136] J. Zaanen, G. Sawatzky, and J. Allen. Band gaps and electronic structure of transition-metal compounds. *Phys. Rev. Lett.*, 55:418, 1998.

[137] F.C. Zhang and T. Rice. Effective Hamiltonian for the superconducting Cu oxides. *Phys. Rev. B*, 37:3759, 1988.

[138] X. J. Zhou, T. Cuk, T. Devereaux, N. Nagaosa, and Z.-X. Shen. *Angle-resolved photoemission spectroscopy on electronic structure and electronphonon coupling in cuprate superconductors. Handbook of High-Temperature Superconductivity: Theory and Experiment.* Springer, Berlin, 2007.

List of publications

Surface and Bulk Contribution to Cu(111) Quantum Efficiency
E. Pedersoli, C. M. R. Greaves, W. Wan, C. Coleman-Smith, H. A. Padmore, S. Pagliara, A. Cartella, F. Lamarca, G. Ferrini, G. Galimberti, M. Montagnese, S. Dal Conte, and F. Parmigiani, *Appl. Phys. Lett.* 93, 183505 (2008).

Ultrafast insulator-to-metal phase transition as a switch to measure the spectrogram of a supercontinuum light pulse
F. Cilento, C. Giannetti, G. Ferrini, S. Dal Conte, T. Sala, G. Coslovich, M. Rini, A. Cavalleri and F. Parmigiani, *Appl. Phys. Lett.* 96, 021102 (2010).

How superconductivity modifies the high-energy scale optical properties in $Bi_2Sr_2Ca_{0.92}Y_{0.08}Cu_2O_8$
C. Giannetti, F. Cilento, S. Dal Conte, G. Coslovich, G. Ferrini, H. Molegraaf, M. Raichle, R. Liang, H. Eisaki, M. Greven, A. Damascelli, D. van der Marel and F. Parmigiani, *submitted to Nature Communications.*

Inducing a superconducting-to-normal-state first-order phase transition in overdoped $Bi_2Sr_2Ca_{0.92}Y_{0.08}Cu_2O_8$ by ultrashort laser pulses
G. Coslovich, C. Giannetti, F. Cilento, S. Dal Conte, G. Ferrini, P. Galinetto, M. Greven, H. Eisaki, M. Raichle, R. Liang, A. Damascelli and F. Parmigiani, *submitted to Phys. Rev. B.*

Disentangling the electronic and phononic glue in high-T_c superconductors
S. Dal Conte, C. Giannetti, F. Cilento, G. Coslovich, G. Ferrini, M. Raichle, R. Liang, A. Damascelli and F. Parmigiani, *in preparation.*

Intertube charge transfer induced by free-electron carriers in unaligned bundled SWNT
G. Galimberti, S. Pagliara, S. Ponzoni, S. Dal Conte, G. Ferrini, S. Hofmann and C. Cepek, *in preparation.*

Acknowledgments

I would like to conclude this work by saying thank to many persons which helped me and gave me support and encouragement. Without them all this work wouldn't have been possible.
First of all I would like to thank my advisor Prof. Fulvio Parmigiani for having given me the possibility to work with smart and challenging people and for his support in these Ph.D. years. I am also grateful to Pietro Galinetto because he made possible the collaboration with the ultrafast optics groups in Brescia and Trieste.
A very special thanks goes to my other advisor, Claudio Giannetti. Especially I am grateful for your great enthusiasm for the physics and the overall support and encouragement you gave me during these years. E' stato un piacere lavorare con te e ti devo molto. Grazie mille per il tempo che mi hai dedicato, per la smisurata pazienza nei miei confronti e per le tante cose che mi hai insegnato in questi anni.
A huge thanks goes to Prof. Andrea Damascelli, who accepted to be the referee of my thesis, for the detailed suggestions and the helpful comments to my work.
I am also indebted to Prof. Andrea Damascelli and his group in the University of British Columbia for the growth and characterization of the samples of Y-doped Bi2212. I want to acknowledge Prof. Dirk van der Marel and his group in the University of Genève for having provided to us the equilibrium optical measurements reported in chapter 5.
I am also grateful to Federico Cilento and Giacomo Coslovich of the ultrafast optics group of the university of Trieste, for the non-equilibrium optical measurements in the infrared region carried on with the OPA system. A special thanks goes to my friend and colleague Federico Cilento with whom I spent the last two years of Ph.D.. Your precious help, your expertise in electronics as well as in physics, have made all the work in the lab easier.
During the first year of Ph.D. I had the pleasure to work with Stefania Pagliara and Gianluca Galimberti. E' stato bello lavorare assieme e vi ringrazio molto per tutto quello che avete fatto per me.
Finally I want to acknowledge all the people which I have known during this fantastic period (in alphabetical order): Francesco Banfi, Alessandro Bisio, Patrizia Borghetti, Davide Bossini, Emanuele Cavaliere, Mirko Chiodi, Giovanni Drera, Stefano Facchini, Prof. Gabriele Ferrini, Giovanna Malegori, Matteo Montagnese, Lorenzo Morini and Damiano Nardi.
Tutta la mia riconoscenza va alla mia famiglia perchè mi è sempre stata vicina e non mi ha mai fatto mancare niente. Infine, un grazie sincero a Martina perchè quando sono con te ogni affanno e preoccupazione spariscono e lasciano posto al tuo sorriso ed alla tua dolcezza.